



universität
wien

DIPLOMARBEIT

Single Qubit Control and Observation of Berry's Phase in a Superconducting Quantum Circuit

angestrebter akademischen Grad
Magister der Naturwissenschaften (Mag. rer. nat.)

Verfasser: Johannes M. Fink
Matrikel-Nummer: 0205521
Studienrichtung: A 411 Physik
Betreuer: Univ.-Prof. Dr. Andreas Wallraff,
Laboratorium für Festkörperphysik, ETH Zürich

Wien, am 29. Mai 2007

Preface

It is not quite five years ago that I went to the University of Vienna with some technical background and a strong interest in the fundamental questions that puzzle natural sciences today. Pretty soon after having started my physics studies I noticed the quickly emerging field of experimental quantum information science. It was fascinating for me not only that there exist experiments in this field which partly answer questions philosophers are still arguing about. Furthermore, one can anticipate that if at some point it becomes possible to manipulate and control sufficiently complex quantum systems on their most elementary level, it will revolutionize information sciences and in particular boost the available computational power; computational power that handles the most valuable good of today's societies – information.

There is a large number of different approaches to the realization of a future quantum information processor. Many scientists would agree however, that an implementation that becomes useful at some point will probably be a solid state system. Preferably one that is harnessing conventional integrated electronic circuit techniques in contrast to 'bottom up' nano-fabrication approaches. When I got the chance to work with a young team at ETH Zürich on the experimentally probably most advanced solid state qubits, I knew there would be unforeseen challenges. Setting up a rather sophisticated experiment basically from scratch in the framework of a diploma thesis held some risks and definitively would require some extra time. Now I can say however that it was a good decision - setting up a new lab and working on this thesis satisfied my interest in both technological challenges and the puzzling features of quantum information science.

Abstract

The *circuit quantum electrodynamics* experiment set up during this diploma thesis represents a solid state version of optical cavity quantum electrodynamics [1] in which a superconducting qubit is coupled to a high finesse cavity. It was proposed in [2] and realized for the first time in [3], where the coherent interaction of a single microwave photon with a quantum mechanical solid state circuit was demonstrated. This setup not only offers the possibility to carry out quantum optics experiments in a solid state system [4, 5], it moreover is a promising candidate for the realization of a quantum information processor [6].

This thesis summarizes and discusses technical achievements and first experimental results obtained during one year of setting up a new laboratory at ETH Zürich. The experiments required the installation of a new dilution refrigerator as well as low noise measurement and control circuitry at microwave frequencies. Results of spectroscopic and time-resolved measurements on a fully electrically controllable superconducting charge qubit, the Cooper pair box, embedded in a coplanar waveguide microwave resonator are presented.

First results of this work concern the spectroscopic characterization of the cavity plus qubit system. Using the AC Stark effect we were able to calibrate and control the average number of photons in the resonator. Furthermore spectroscopically measured two photon sideband transitions are investigated. These show in principle the potential of driving time-resolved sideband transitions which could be used to entangle qubit states and photon number states [7] – an important technique to couple more than one qubit, create Bell states and to establish an interface between flying and stationary qubits.

The main focus of the presented work was the development of coherent qubit state control and measurement in the time domain. We demonstrate short single qubit gate operation times in Rabi oscillation measurements performed with a high fidelity quantum non demolition readout. Measurements of the dephasing time using Ramsey and spin echo techniques show coherence times that are among the longest ever observed in solid state qubits. Finally the implemented quantum state tomography enables us to fully determine the qubit state vector.

The methods described above are the prerequisites for the first observation of Berry's phase in a solid state qubit. The Berry phase is a time independent phase that arises from geometric properties of the underlying parameter space only. It is of fundamental interest to observe a geometrically acquired phase in a macroscopic pseudo spin- $\frac{1}{2}$ system. Moreover geometric phases constitute a promising candidate for the realization of robust qubit phase gates for quantum information processing [8, 9].

Contents

Preface	iii
Abstract	v
1 Introduction	1
2 Review and Theory	5
2.1 Quantum Information Basics	5
2.1.1 Qubits	5
2.1.2 Entanglement	8
2.1.3 Quantum Computation	11
2.2 Superconducting Charge Qubit	16
2.2.1 Josephson Tunnel-Junction	17
2.2.2 Cooper Pair Box (CPB)	20
2.3 On-Chip Microwave Cavity	25
2.3.1 Mapping of Transmission Line Resonance to LC Resonance	25
2.3.2 Coplanar Waveguide Resonator	28
2.3.3 Quantization of the LC Oscillator	29
2.4 Circuit Quantum Electrodynamics	30
2.4.1 Coupling of CPB to Cavity	32
2.4.2 Readout Scheme	34
3 Measurement Setup	37
3.1 The Sample	37
3.1.1 Microwave Resonator	38
3.1.2 Cooper Pair Box	38
3.1.3 Sample Mount	39
3.2 Measurement, Control and Data Acquisition	40
3.2.1 Microwave Circuit	41
3.2.2 DC Bias Circuits	50
4 Circuit QED Experiments	53
4.1 Characterization of the System	54
4.1.1 Cavity Resonance Frequency and Quality Factor	54
4.1.2 Energy Level Diagramm of the CPB	55
4.1.3 Response to Bias	56

Contents

4.1.4	Spectroscopic Characterization	59
4.2	Spectroscopic Measurements	61
4.2.1	AC Stark Effect	61
4.2.2	Two-Tone Sideband Spectroscopy	62
4.3	Time Domain Measurements	64
4.3.1	Rabi Oscillations	65
4.3.2	Ramsey Fringes	68
4.3.3	Spin Echo Technique	70
4.3.4	Tomography of Quantum States	73
4.4	Berry Phase Experiment	76
4.4.1	The Geometric Phase	76
4.4.2	Pseudo Spin-1/2 under RF-Irradiation	78
4.4.3	Measurement & Results	80
5	Conclusion and Prospects	91
	Bibliography	VIII
	Acknowledgements	IX
	Curriculum Vitae	XI

1 Introduction

It was about a hundred years ago that Max Planck came up with an approach based on using quantized (discrete) frequencies to explain the spectrum of black body radiation and hence gave rise to a new theory called quantum mechanics. It became the most successful physical theory so far – no relevant experiment is in contradiction with its predictions. Quantum theory is also possibly the most general physical theory: it explains the behavior of our microscopic world including, for instance, almost all of chemistry, but is also believed to apply at all scales, i.e. to the properties of the universe as a whole, see e.g. [10]! Its interpretation is as controversial now as it was in former times when Einstein and Bohr heatedly discussed these issues. In the past decade however both, theoretical and experimental advances, have made it possible to ask what were formerly philosophical questions about the conceptual difficulties of quantum theory, and to test these issues in the laboratory.

Quantum Information

Closely related to these new investigations the concept of quantum information arose [11, 12, 13]. This sort of information is physical information that is held in the *state* of a quantum system. The familiar classical way in which information is recorded, for instance as in today's computers, is in terms of *bits*, each bit being either a zero or a one, corresponding to a switch being off or on, for instance. Thus, there are two mutually exclusive alternatives. The unit of quantum information is the qubit, which can also take the values 0 and 1, but the either-or situation of classical information now becomes much richer: in a sense, a qubit can have both values simultaneously!

Quantum information is carried by a two-state quantum system, that is a physical system which would typically be observed to be in one or the other of two distinct possible states. For instance, it could be an electron that is spinning either clockwise or anticlockwise¹, or an electron that is either in one or the other of two electronic states that have different energies. But in a way that is peculiar to quantum mechanics, such systems can also be in these two quite distinct states at the same time in the form of a so-called *superposition of states*. The notion of a superposition of states has no classical analogue and is a situation that is difficult to conceive of from our perspective of how the world works – an object is either one thing or the other, never both at the same time. It is this possibility to store two different bits of information simultaneously that gives quantum information the potential to be so powerful in information processing, such as in a quantum computer.

¹Spin in quantum mechanics has some subtle properties that make this picture a little simplistic.

Motivation

The ability to manipulate quantum information enables us to perform tasks that would be unachievable in a classical context. One example is the unconditionally secure transmission of information which is enabled by implementing *quantum cryptography*. The other is *quantum information processing* which contains certain algorithms and tasks classical computers cannot perform efficiently. It means that the computing time grows exponentially with the size of the problem for a classical computer, but much less slowly, in polynomial time, for a quantum computer. In fact slowly enough such that totally intractable problems on a classical computer can be solved on a quantum computer. Two examples of these include Shor's factoring algorithm [14] – which can be used to find the prime factors of very large numbers, a crucial task in the cracking of codes – and Grover's search algorithm [15] used to search large databases more efficiently.

Other possible applications include the simulation of complex quantum systems like large molecules and their interactions, which is extremely inefficient on classical computers. As an example consider a quantum system that can be modeled with 50 quantum bits. Only to store the statevector of this system requires already 2^{50} classical bits, i.e. ~ 140 terabyte of memory. Material research, biology and nano technology, all will benefit, and at some point require a better simulator for engineering new quantum products. Finally, a quantum computer is claimed to be able to provide approximate solutions to some large 'NP-complete' problems² much faster compared to so far known classical algorithms [16]. Problems like *the traveling sales man* can be mapped to a variety of optimization problems where limited resources are being allocated to maximize or minimize a relevant quantity, arising numerously in logistics, engineering and finance.

Open Quantum Systems

All physical systems interact with their surrounding environment to one degree or another – to put it with John Donne: 'no man is an island' – and such systems are said to be open systems. This openness results in *decoherence*, the technical term for the 'washing out' of quantum superposition, so that a qubit is no longer simultaneously a one *and* a zero, but it definitely becomes either a one *or* a zero. Decoherence occurs whenever a system interacts with its environment in a thermodynamically irreversible way. Since interference phenomena are crucial features of quantum mechanics and spontaneous, or artificially generated interactions between a quantum system and its environment lead to a suppression of interference, decoherence can often be seen as the *absence of interference*. Decoherence plays a central role in how the observed classical world emerges from its intrinsically quantum nature [17], but more practically, it is one of the limiting factors in the functioning of a quantum computer. The better it is understood, and controlled, the better the chance of building a quantum computer.

²if so, any NP problem as NP complete are the toughest problems in NP. NP is a complexity class in theoretical computer science and terms the set of 'non-deterministic, polynomial time' – problems.

Cavity Quantum Electrodynamics (CQED)

CQED is an active research area in physics which involves the study of open quantum systems. The interaction of matter (atoms) with light (electromagnetic fields) 'trapped' inside a cavity is investigated. Such an experimentally contrived situation offers the opportunity to study the interaction of individual atoms (or *qubits*) with individual *photons* – the quantum particles which constitute the electromagnetic field – in a highly controlled fashion, and draws its importance from the fact that it becomes possible to study this interaction under circumstances in which its purely quantum nature is preserved on long time scales, rather than being 'washed out' by the influence of environmental noise ever present in the macroscopic world. An actual experiment can still be limited by noise that is technical in nature, in the ideal case however one can reach the fundamental limit where spontaneous interactions unveil. The latter was the case in [3] where the vacuum field inside the resonator was sufficient to generate observable vacuum rabi mode splitting spectra in a quite similar setup to the one presented in the following chapters.

In this thesis the interaction of one 'artificial atom' with individual photons at microwave frequencies is studied. This is done in an architecture that was named *circuit QED* [3]. It constitutes an important step towards coupling more than one qubit coherently by means of the radiation field [18, 19, 20]. Furthermore with similar circuit QED techniques, it should become possible to create hybrid interfaces between flying qubits (photons), stationary solid state qubits used to perform fast calculations and e.g. atoms serving as memory for quantum communication in the future [21, 22, 23].

Superconducting Circuits

In order to realize a qubit, an approach using superconducting electronic circuits was chosen. These circuits are macroscopic structures on a chip – consisting of inductors, capacitors, resistors and Josephson junctions – and behave quantum mechanically under appropriate conditions, where their properties can be designed and controlled at will. It is therefore possible to build a superconducting two-level system, playing the role of an artificial atom (the qubit), out of macroscopic solid state electrical circuits [24], fabricated using techniques borrowed from conventional integrated circuits fabrication. It's realization is based on the Josephson tunnel junction, a non-dissipative, strongly non-linear circuit element available at ultra low temperatures. In contrast to microscopic entities such as spins or atoms, these circuits tend to be well coupled to other circuits, which makes them appealing from the point of view of readout and logical gate implementation.

Context

The *circuit QED* setup which was implemented during this diploma thesis offers the potential to study a variety of quantum effects involving qubit - photon interactions. The implementation consists of a fully electrically controllable superconducting qubit (the *Cooper pair box*),

1 Introduction

which is coherently coupled to a quantized radiation field (some microwave photons) in an on-chip cavity formed by a superconducting transmission line resonator. This scheme was first proposed in [2] and first realized by Wallraff et.al. [3]. Using this experimental setup, various spectroscopic and time-resolved cavity QED experiments have been performed. The developed methods were then employed to allow the first observation of Berry's phase – a quantum geometric phase – in an electronic circuit. Apart from being fundamentally interesting to observe a geometrically acquired phase in an artificially generated quantum bit, which demonstrates the high control and coherence of the macroscopic superconducting solid state circuits in use, the geometric phases constitute a promising candidate for the realization of qubit phase gates that are more robust to noise compared to gates relying on the dynamical phase [8, 9].

2 Review and Theory

In the beginning of this chapter some selected basics of quantum information are presented. In section 2 and 3 an introduction to the theoretical background of superconducting charge qubits and the microwave resonator serving as a cavity is given. Building up on that, and using the Jaynes-Cummings model of CQED, the theoretical framework for experiments in the dispersive regime is developed. The dispersive regime is entered when the 'artificial atom' is detuned from the resonator with a detuning taken to be much larger than the coupling between them, which means that there are no actual photons being absorbed while their interaction is still observable.

2.1 Quantum Information Basics

This section elaborates on basic aspects of quantum information science. After starting out with the concept of the qubit there is a more extensive discussion on the probably most interesting feature of quantum systems which is entanglement. Finally, it is discussed how these concepts could be harnessed in a useful way in order to do computations more efficiently.

2.1.1 Qubits

In analogy to the elementary unit of information in classical information theory, the bit, one can define a quantum bit or qubit, the unit of quantum information. A qubit is a quantum mechanically behaving two-level system, however the definition of its information content is independent of its physical realization and can be used synonymously, like in classical information theory: *A qubit is a state within a two-dimensional Hilbert space¹. The computational basis of this Hilbert space is $\{|0\rangle, |1\rangle\}$.*

All quantum systems which can be described by a two dimensional Hilbert space therefore serve as implementations of qubits. In this category there are e.g. the polarization state of photons, the spin subspace of spin- $\frac{1}{2}$ particles, or even two spatial modes or paths can be associated to the two basis states of a qubit. Experiments described in this thesis use the Cooper pair box, a superconducting solid state circuit, as implementation of a qubit.

In contrast to the classical bit, the qubit can not only be in one of the computational basis states $|0\rangle, |1\rangle$, but also in arbitrary linear superpositions $|\psi\rangle = \alpha|0\rangle + \beta|1\rangle$, with the normalization $|\alpha|^2 + |\beta|^2 = 1$. Those states may be represented as vectors in the two-dimensional

¹A complex vector space with an inner product.

Hilbert space:

$$|0\rangle = \begin{pmatrix} 1 \\ 0 \end{pmatrix}, \quad |1\rangle = \begin{pmatrix} 0 \\ 1 \end{pmatrix}, \quad |\psi\rangle = \begin{pmatrix} \alpha \\ \beta \end{pmatrix} \quad \text{and} \quad \rho = |\psi\rangle\langle\psi| = \begin{pmatrix} \alpha^*\alpha & \beta^*\alpha \\ \alpha^*\beta & \beta^*\beta \end{pmatrix}, \quad (2.1)$$

with ρ the density matrix. There is an infinite number of qubit states a single qubit can represent. However, this information content is somewhat hidden as the single measurement reveals only 0 or 1 with probabilities $|\alpha|^2$ or $|\beta|^2$. Since formulations of quantum mechanics in terms of pure states are adequate for isolated systems only, in general a quantum mechanical system needs to be described in terms of a density matrix ρ , which is a statistical operator (one usually thinks of ensembles). ρ contains the maximum information that can be obtained about a compound system in a so-called mixed state.

Blochsphere Representation

Instead of writing down the qubit-state as a superposition of the two basis state vectors one can similarly illustrate the state on the Bloch sphere, see Fig. 2.1, which is a unit sphere - a graphical representation of a two dimensional Hilbert space, the pure state space of a two-level quantum mechanical system.

Since global phase factors do not affect physical state we can take the coefficient of $|0\rangle$ to be real and non-negative. Thus $|\psi\rangle$ can be represented as

$$|\psi\rangle = \cos\left(\frac{\theta}{2}\right)|0\rangle + e^{i\varphi}\sin\left(\frac{\theta}{2}\right)|1\rangle \quad \text{with} \quad 0 \leq \theta < \pi \quad \text{and} \quad 0 \leq \varphi < 2\pi, \quad (2.2)$$

which maps $|0\rangle$ to $(0,0,1)$ and $|1\rangle$ to $(0,0,-1)$ in cartesian coordinates. At the equator on the other hand, we have the equal superposition of the two states: $\frac{1}{\sqrt{2}}(|0\rangle + e^{i\varphi}|1\rangle)$. Using the definition above, the Bloch vector is given by $(\cos\phi\sin\Theta, \sin\phi\sin\Theta, \cos\Theta)$.

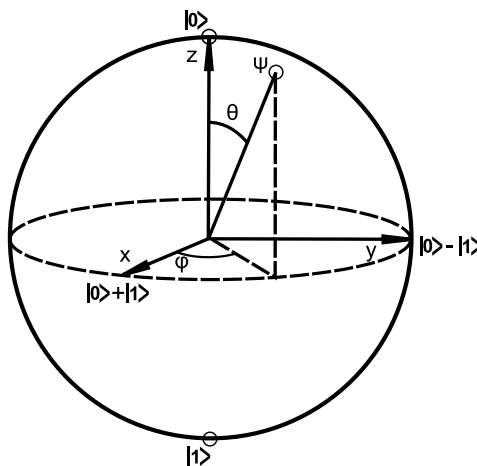


Fig. 2.1: Blochsphere representation of a qubit's state space.

Mixed states of a single qubit can also be represented in the Bloch sphere picture very conveniently. Mixed state vectors have an absolute value of ≤ 1 . The state space (Bloch sphere) of a qubit under the influence of energy dissipation shrinks towards the north pole of the Bloch sphere – the ground state. The effect of dephasing, i.e. the loss of phase information, can be illustrated with a deformed sphere aligned along the z axis [13].

Single Qubit Measurement

When a single qubit is prepared in an arbitrary superposition $|\psi\rangle = \alpha|0\rangle + \beta|1\rangle$, it is impossible to determine the coefficients α and β with certainty by any way in a single measurement. Considering a measurement in the computational basis of the qubit there are two possible measurement outcomes, $|0\rangle$ and $|1\rangle$, where the corresponding probabilities of these two outcomes are:

$$P(0) = |\alpha|^2 \quad \text{and} \quad P(1) = |\beta|^2. \quad (2.3)$$

The outcomes of a single measurement on an given qubit state of unknown preparation is thus totally random. However, for every possible qubit state, there exists a basis in the qubit Hilbert space which allows to obtain measurement results with a probability of unity: *Given an orthonormal basis $\mathcal{B} = \{|b_1\rangle, |b_2\rangle\}$, a qubit is said to be prepared in the basis \mathcal{B} if it can be written as either $|b_1\rangle$ or $|b_2\rangle$.*

It can be seen easily that the task of determining the basis of preparation of a single qubit is equivalent to the task of finding the coefficients α and β , which is not possible either. The measurement has to be repeated many times in order to achieve this task but this is not possible since the measurement process projects the state on an eigenstate of the measurement operator. This fact, together with the *no cloning theorem*, which was pointed out by Wootters and Zurek [25] and shows the impossibility of creating a perfect copy of a qubit, is the basis for quantum cryptographic methods for communication systems partly in use already today [26, 27]. The proof of the no cloning theorem is pretty much straightforward. Note however that it has been shown that at least approximate copies are possible to produce [28]. It turns out that there exists an upper bound of the fidelity of such a process, which decreases with increasing the number of copies.

If on the other hand, the basis the qubit state has been prepared in is known, one can determine with certainty in which state the qubit was prior to the measurement. If, in addition, there is more than one equally prepared quantum state available, a repeated measurement can be done in order to estimate the full information about the state vector. *Quantum state tomography* enables the phase sensitive readout of a qubit's state and requires ideally only three different measurements, each carried out repeatedly. Its implementation was part of this thesis and is presented in section 4.3.4.

2.1.2 Entanglement

When a system contains more than one qubit, the Hilbert space of the compound system is a tensor product of the individual qubit spaces². In the case of two qubits, $n = 2$ we therefore have a four dimensional Hilbert space, 2^n , for the description of the whole system. Within this state space there exist state vectors which describe the compound system but can not be factorized into product states of the individual qubits. Such non-separable states are called entangled states.

In the presented work there was only one qubit involved and the entanglement of qubitstates with photon-numberstates was only observed indirectly e.g. in section 4.2.2. Nevertheless, I want to go a little more into detail here as entanglement is not only the characteristic property that makes a quantum information processor potentially more powerful and quantum cryptography more efficient, after all it is the feature that makes quantum information science conceptually interesting! Remember, qubits can be implemented with individual particles, which can be spatially separated. However, entanglement means that a measurement on one of the two qubits can not be seen independent from the measurement of its partner, effectively creating correlations between measurement outcomes. This is a remarkable feature with no classical analog.

EPR-Paradox

In order to illustrate the counterintuitive properties of entanglement more clearly, it is useful to briefly discuss the EPR-paradox formulated by Albert Einstein, Boris Podolsky and Nathan Rosen in 1935 [29]. They stated three general and reasonable assumptions and showed that quantum mechanics is not compatible with all of them, concluding that quantum theory is incomplete. The thought experiment they proposed had a great impact in the understanding of the foundations of quantum physics. Nowadays however, it constitutes simply the best way to proof two-qubit entanglement in the laboratory.

The assumption of *completeness* means that 'every element of the physical reality must have a counterpart in the physical theory'. The concept of *reality* is briefly said referring to the fact that quantities in the theory are physically real, independent of their being measured or not, or as EPR puts it: 'If, without in any way disturbing a system, we can predict with certainty the value of a physical quantity, then there exists an element of physical reality corresponding to this physical quantity.' Finally they called for *locality* which does not allow instantaneous long-range effects.

Building up on those assumptions the authors discussed, in accordance with quantum mechanics, a problem with entangled particles. Such particles can be arbitrarily separated after their interaction, while they are still characterized by a joint (entangled) state. After measurement of only one particle, the eigenstates of both particles are determined. Therefore

²Unfortunately there is no generalization of the Bloch sphere picture to a many qubit system. It also would not be practicable as the state space of an n -qubit system scales with 2^n . The same difficulties arise when qudits like the qutrit (3-level system) are involved.

it is possible to predict (with certainty) the measurement outcome for the second particle without ever interacting with it. EPR do not accept that reality of physical quantities of one particle depend on the character of measurement which is done on the other. They conclude that quantum theory is not complete. For a complete description of reality they propose to incorporate so-called hidden variables characterizing the states of the particles. Independent of those assumptions and conclusions being correct, it is interesting to investigate the possibility of completing quantum theory with hidden variables. In such a theory there are no objective coincidences. The value of an observable for a single system is defined at all times, possibly this value is not known but gets eventually 'discovered' when an actual measurement is carried out.

Bell's Theorem

J. S. Bell started out with a very general definition of hidden variables: The hidden variables λ should act spatially limited (local) and deterministic in time. With this assumption he managed to find a purely algebraic, and experimentally verifiable, condition for a local hidden variable model [30]. Bell considers the following situation which was advocated by Bohm and Aharnov [31]: A source emits pairs of entangled spin- $\frac{1}{2}$ particles which are analyzed with two Stern-Gerlach setups at two different points in space, see Fig. 2.2. The directions of the apparatus field gradients are indicated as a and b , where the possible measurement outcomes are +1 and -1 depending on the angle of deflection. The four Bell states

$$|\Phi^+\rangle = \frac{1}{\sqrt{2}}(|0\rangle_A \otimes |0\rangle_B + |1\rangle_A \otimes |1\rangle_B) \quad (2.4)$$

$$|\Phi^-\rangle = \frac{1}{\sqrt{2}}(|0\rangle_A \otimes |0\rangle_B - |1\rangle_A \otimes |1\rangle_B) \quad (2.5)$$

$$|\Psi^+\rangle = \frac{1}{\sqrt{2}}(|0\rangle_A \otimes |1\rangle_B + |1\rangle_A \otimes |0\rangle_B) \quad (2.6)$$

$$|\Psi^-\rangle = \frac{1}{\sqrt{2}}(|0\rangle_A \otimes |1\rangle_B - |1\rangle_A \otimes |0\rangle_B) \quad (2.7)$$

which are generated in this experiment are the most prominent examples of entangled states. They are defined as maximally entangled quantum states of two qubits (A and B) which are usually thought to be spatially separated, nevertheless exhibiting perfect correlations or anti-correlations respectively.

A *correlation* $E(a, b)$ is the averaged product of both measurement outcomes. If we take locality into account the outcome of a measurement of an observable of particle A is only dependent on the direction of the field gradient a and possibly on a hidden variable λ . $\rho(\lambda)$ is the probability distribution with the condition $\int \rho(\lambda)d\lambda = 1$. The expectation value of a mea-

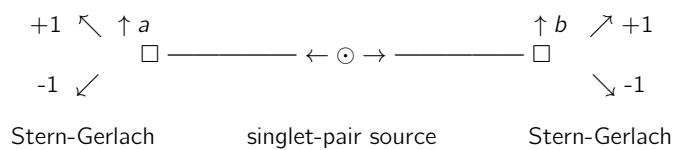


Fig. 2.2: Bell's gedankenexperiment with entangled spin- $\frac{1}{2}$ particles in a singlet state.

surement of particle A with analyzer orientation a is $A(a, \lambda)$, the expectation value of particle B with orientation b is $B(b, \lambda)$ and the expectation value of the compound measurement is then just

$$E(a, b) = \int A(a, \lambda)B(b, \lambda)\rho(\lambda)d\lambda. \quad (2.8)$$

Using these definitions and two alternative orientations of the analyzers a' and b' the so-called CHSH inequality derived in [32] can be written as

$$-2 \leq E(a, b) - E(a, b') + E(a', b) + E(a', b') \leq 2. \quad (2.9)$$

It is a generalization of the original Bell-inequality, as it holds also for possibly occurring 'zero-measurements' e.g. due to detector inefficiencies, where A and B can be seen as averaged measurement outcomes ($|A|, |B| \leq 1$). If we take the orientations of the Stern-Gerlach analyzers to be in a single spatial plane they can be substituted by angles $\alpha, \beta, \gamma, \delta$. The quantum mechanical expectation value for the correlations occurring is $E_{QT}(a, b) = -\cos(\beta - \alpha)$. This so defined quantum theoretical value violates Bell's inequality; in particular for $\alpha = 0^\circ, \beta = 45^\circ, \gamma = 90^\circ, \delta = 135^\circ$ we get the largest discrepancy which is

$$|-\cos(45^\circ) + \cos(135^\circ) - \cos(45^\circ) - \cos(-45^\circ)| = 2\sqrt{2} > 2.$$

Experiments confirmed quantum theory and ruled out the possibility of local hidden variables [33]. The major loophole of a required space-like separation of the particles [34] as well as the detection efficiency loophole [35] could be closed each, although not together in one experiment. Note, for more than two entangled qubits, there are non-probabilistic tests available. The GHZ-experiment constitutes a test of local reality that was developed by Green, Horne and Zeilinger who proposed the entangling of three particles (GHZ-state) with the advantage of getting a test result without analyzing large sets of data statistically. In principle just 4 single measurements are sufficient to show the contradiction of quantum mechanics and local realistic theories; the experiment was done in 1990 [36].

If one accepts the experimental results one has to decide which of EPR's assumptions are invalid. Most physicists would give up *locality*, as one obviously has to accept that the two separated but entangled particles have to be described as one single system independent of their separation.³ Some believe it (also) is the *reality assumption*, losing a 'real' world independent of the presence of an observer; [37] supports this position with some experimental evidence. Others claim the invalidity of another implicit assumption in deriving the Bell inequality called *Counterfactual Definiteness* (CFD)⁴ leading to the *many world interpretation* of quantum mechanics which was developed by Everett [38] and got popularized by DeWitt [39] and Deutsch [40]. Last but not least there is also the possibility of a entirely determined world, where most physicists would probably not agree on. It will be interesting if further experiments

³For example Bohm's quantum theory works out using non-local hidden variables. Most find it not elegant however, as it is still unclear how it can be compatible to quantum field theory which is essentially local.

⁴Bell's Theorem implicitly assumed that every possible measurement - even if not performed - would have yielded a single definite result.

can contribute to these questions and rule some of the above stated possibilities out.

Decoherence vs. Entanglement

It is important to clarify at this point that entanglement is not something artificially generated in the laboratories. Actually everything that interacts in any way gets entangled to some degree - it is the theory of *decoherence* that predicts that the entanglement between the system and its environment leads to a loss of information about the system's state.⁵ This is what makes it an irreversible process and ensures that different elements in the quantum superposition of the system-plus-environment's wave function can no longer interfere with each other. The interaction leads to additive probabilistically behavior (towards classical behavior), hence suppressing coherence between system's states.

Avoiding entanglement with the environment is a major task in engineering a quantum information processor. On the other hand, entanglement is increasingly believed to be a main resource for quantum communication and quantum information processing [41]. Quantum teleportation, error correction, computation and communication, all benefit from – or require – entanglement.

2.1.3 Quantum Computation

Most approaches to *Quantum Information Processing* (QIP) try to implement coherent control of individual qubits with gates building circuits somewhat similar to existing classical computers. It remains an open question if this is the approach that will prevail in the end, however pursuing this route enables us to learn about and test the properties of quantum systems in an intuitive fashion. The probably most advanced implementation in this spirit is still NMR based quantum computation. In [42] the authors use seven spin-1/2 nuclei in a molecule as quantum bits, which can be manipulated with room temperature liquid state nuclear magnetic resonance techniques and show the prime factorization of $N = 15$. However, the scalability of these systems is unclear and other systems such as ion trap setups [43, 44] or superconducting circuit implementations [45, 46, 19] are actively investigated presently, showing considerable progress in the realization of quantum information processing with gates.

Note, there are other, yet more exotic approaches, such as the *one way quantum computer* which starts out with a cluster state of as many entangled photons as possible and computes by doing measurements on this photons with purely linear components [41], and the *adiabatic quantum computation* where the initial Hamiltonian corresponding to the ground state of the system is applied to the system and in the following changed adiabatically until a final Hamiltonian is reached. This can be useful as the ground state of the final Hamiltonian can be taken to be the solution to a given problem [47].

⁵One had to know the exact state of the environment in order to describe the entangled state after interaction correctly. This is not possible for complex environments and leads to an effective loss of information about the system's state.

Quantum Gates

Any single qubit operation can be represented as a rotation on the Bloch sphere, see Fig. 2.1. Like in classical information processing one can introduce gates and combine several gates to create a quantum circuit in order to perform arbitrary operations on single qubits, see Fig. 2.3, and to perform conditional operations between qubits, see Fig. 2.4.

Some nontrivial operations on single qubits may be represented by means of the Pauli matrices acting on the computational basis states. Bit flip σ_x , bit flip with additional phase σ_y and phase flip σ_z are given by

$$\sigma_x|0\rangle = |1\rangle; \quad \sigma_x|1\rangle = |0\rangle \quad (2.10)$$

$$\sigma_y|0\rangle = i|1\rangle; \quad \sigma_y|1\rangle = -i|0\rangle \quad (2.11)$$

$$\sigma_z|0\rangle = |0\rangle; \quad \sigma_z|1\rangle = -|1\rangle \quad (2.12)$$

with

$$\sigma_x = \begin{pmatrix} 0 & 1 \\ 1 & 0 \end{pmatrix}, \quad \sigma_y = \begin{pmatrix} 0 & -i \\ i & 0 \end{pmatrix}, \quad \sigma_z = \begin{pmatrix} 1 & 0 \\ 0 & -1 \end{pmatrix}. \quad (2.13)$$

Note that the only nontrivial single bit operation in classical computations is the NOT operation. In quantum computation on the other hand, all unitary matrixes U with $U^\dagger U = I$ (because of the normalization condition of a quantum state) specify valid quantum gates. It furthermore turns out that there exists *no universal NOT* in quantum computation as the application of any unitary operator on its eigenstate (corresponding to the eigenvalue = 1) does yield the eigenstate again. One example is the σ_x bit flip operator $\sigma_x|\psi_e\rangle = |\psi_e\rangle$ with the eigenstate $|\psi_e\rangle = \frac{1}{\sqrt{2}}(1, 1)$.

Another useful operation is realized by applying the phase gate U_ϕ on a quantum mechanical state:

$$U_\phi|0\rangle = e^{i\phi}|0\rangle \quad \text{and} \quad U_\phi|1\rangle = |1\rangle \quad \text{with} \quad U_\phi = \begin{pmatrix} e^{i\phi} & 0 \\ 0 & 1 \end{pmatrix}, \quad (2.14)$$

providing a relative phase shift. The Hadamard gate H provides an operation that is also used in many quantum algorithms. It maps n qubits initialized with $|0\rangle$ to a superposition of all 2^n orthogonal states in the basis $|0\rangle, |1\rangle$ with equal weight. For one qubit:

$$H|0\rangle = \frac{1}{\sqrt{2}}(|0\rangle + |1\rangle); \quad H|1\rangle = \frac{1}{\sqrt{2}}(|0\rangle - |1\rangle) \quad (2.15)$$

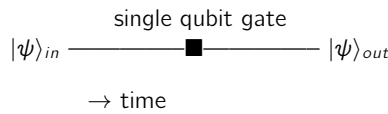


Fig. 2.3: Quantum circuit for a single qubit gate operation.

with

$$H = \frac{1}{\sqrt{2}} \begin{pmatrix} 1 & 1 \\ 1 & -1 \end{pmatrix} \quad (2.16)$$

It flips the qubit sort of halfway (to the equatorial plane of the Bloch sphere) when applied to one of the computational basis states $|0\rangle$ or $|1\rangle$, which means that a measurement on the produced superposition state will totally random yield one of the basis states. However, if it is applied subsequently again, all randomness vanishes and we obtain the original state again, since $HH = I$. Such a gate has no classical analog.

In order to implement useful algorithms two-qubit gates are necessary. The most discussed one is the controlled NOT gate ${}_cN$ (CNOT):

$${}_cN|00\rangle = |00\rangle; \quad {}_cN|01\rangle = |01\rangle; \quad {}_cN|10\rangle = |11\rangle; \quad {}_cN|11\rangle = |10\rangle \quad (2.17)$$

with

$${}_cN = \begin{pmatrix} 1 & 0 & 0 & 0 \\ 0 & 1 & 0 & 0 \\ 0 & 0 & 0 & 1 \\ 0 & 0 & 1 & 0 \end{pmatrix} \quad (2.18)$$

and the first bit being the control bit and the second bit being the target bit. The CNOT gate flips the second qubit (target) if and only if the first qubit (control) is 1. While a superposition state at the target qubit is trivial, a superposition at the control is not. Figure 2.4 shows how one can create the Bell states by feeding a superposition state into the control input of a CNOT gate.

The ${}_cN$ together with the single qubit phase gate U_ϕ (providing arbitrary 1 qubit rotations) constitutes a set of gates which is said to be *universal* for quantum computation. Such a universal set of gates can approximate any unitary transformation U , that is all other possible gates, with arbitrary accuracy, where in fact quantum circuits subsume classical circuits, see [48] or chapter 4.5 in [13]. Note however, that a lot of these unitary transformations can only be implemented very inefficiently.

Another striking fact is reversibility. All quantum gates are reversible since quantum mechanics

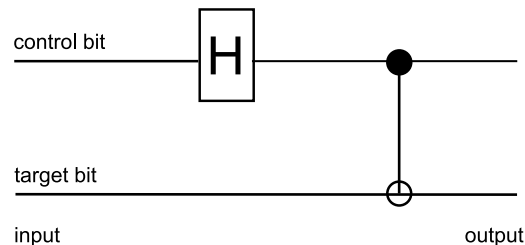


Fig. 2.4: Circuit diagram illustrating Bell-state creation. Before applying a CNOT gate the control-bit was prepared in a superposition state using a Hadamard transform. At the output we obtain one of the four Bell-states, Eq. (2.4) – Eq. (2.7), depending on the chosen input bits.

is reversible. CNOT is an analog to the classical XOR gate but unitary. In the classical case in every two bit gate like the XOR one bit of information is lost, which increases the entropy of the system hence leading to a higher temperature. In order to erase one bit of information one has to afford at least an energy of $k_b T \ln(2)$. This limitation of classical computation is called the Neumann-Landauer limit and can be bypassed by quantum computation. In today's computers the energy dissipation is about $500 k_b T \ln(2)$ per elementary operation.

Deutsch Algorithm – an Example of a Quantum Algorithm

The crucial task to solve a problem more efficiently than a classical computer is to harness the various quantum gates in an intelligent way that allows quantum physics to exhibit its power. The 'milk-cows' of the whole field are Shor's factoring algorithm, which allows an exponentially faster decomposition of large numbers to their prime factors [14] – a crucial task in the cracking of codes – and Grover's search algorithm, which makes it quadratically more efficient to find an entry in a large unstructured database [15]. Here however, the conceptually easier to understand but still powerful Deutsch algorithm shall be discussed. It was the first one proposed (1992) [49] and it shows how the concept of *quantum information* enriches information theory. After all, a nice demonstration of the Deutsch algorithm has been achieved in an ion-trap setup [44] which was qualitatively equivalent to the experimental setup presented in this thesis. While in the ion trap setup the electronic and motional states of a single calcium ion serve as qubits, in the circuit QED setup which was set up during this thesis, that could be realized with the charge state of the Cooper pair box and the photon number-state of the microwave resonator.

Before describing what the algorithm does mathematically, an example of a given problem might be useful: Think of coins which have either heads and tails (authentic) or heads on both sides (fake). In order to decide if a given coin is either fake or authentic one has to have a look on both sides of that coin. However, it turns out that harnessing the superposition principle of QM one look is enough! We are given a black box (can be shown to be realized for qubits) which takes one bit x and outputs the value $f(x)$, where $f(x)$ is defined as a boolean (0-1 valued) function that is either balanced or constant.

$$f : \{0, 1\} \rightarrow \{0, 1\} \tag{2.19}$$

with

$$f(0) = f(1) \rightarrow \text{constant, or } f(0) \neq f(1) \rightarrow \text{balanced.} \tag{2.20}$$

One can easily see that there are two queries required in order to determine if $f(x)$ is constant or balanced. The function has to be evaluated for $x = 0$ and $x = 1$.

The quantum algorithm on the other hand works as follows (see also Fig. 2.5). First, a Hadamard gate is applied to a qubit in the state $|0\rangle$ at the input, forming a superposition of the two possible input values x (query qubit). Another Hadamard is applied to an additional

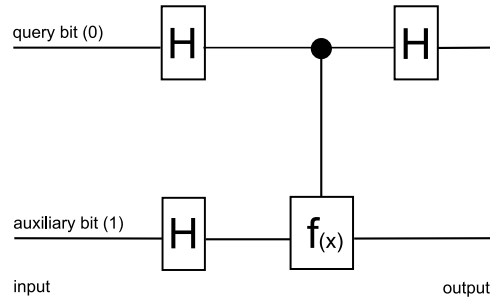


Fig. 2.5: Circuit diagram illustrating the Deutsch algorithm. Hadamard gates are used to create superposition states of query and auxiliary bits respectively. After the function is applied to the two inputs just once, the query qubit can be read out in order to determine the global balanced-or-constant property of the function $f(x)$.

qubit in the state $|1\rangle$ which serves as an auxiliary answer qubit y .

$$|0\rangle|1\rangle \rightarrow H|0\rangle H|1\rangle = \frac{1}{2}(|0\rangle + |1\rangle)(|0\rangle - |1\rangle)$$

Next, the black box function in the form of a unitary transform $U_f : |x, y\rangle \rightarrow |x, y \oplus f(x)\rangle$ is applied (\oplus ... addition modulo 2); this XORs the result with the auxiliary qubit.

$$\begin{aligned} \rightarrow U_f\left[\frac{1}{2}(|0\rangle + |1\rangle)(|0\rangle - |1\rangle)\right] &= \begin{cases} \pm\frac{1}{2}(|0\rangle + |1\rangle)(|0\rangle - |1\rangle), & f(0) = f(1) \\ \pm\frac{1}{2}(|0\rangle - |1\rangle)(|0\rangle - |1\rangle), & f(0) \neq f(1) \end{cases} \\ &= \frac{1}{2}[(-1)^{f(0)}|0\rangle + (-1)^{f(1)}|1\rangle](|0\rangle - |1\rangle) \end{aligned}$$

Finally, another Hadamard is applied on the query qubit before getting measured. If the result is 0, the function is constant, otherwise the function is balanced.

$$\begin{aligned} \rightarrow H\frac{1}{2}[(-1)^{f(0)}|0\rangle + (-1)^{f(1)}|1\rangle](|0\rangle - |1\rangle) &= \begin{cases} \pm\frac{1}{\sqrt{2}}|0\rangle(|0\rangle - |1\rangle), & f(0) = f(1) \\ \pm\frac{1}{\sqrt{2}}|1\rangle(|0\rangle - |1\rangle), & f(0) \neq f(1) \end{cases} \\ &= \frac{1}{\sqrt{2}}|f(0) \oplus f(1)\rangle(|0\rangle - |1\rangle). \end{aligned}$$

So by measuring the first qubit we determine $f(0) \oplus f(1) = 0$ (constant), or $f(0) \oplus f(1) = 1$ (balanced), which is a global property of $f(x)$ and is obtained with only *one* evaluation of that function! The difference to a classical computation is that there is a superposition state at the input of the black box and two mutually exclusive alternatives can interfere with each other during the computation. By using the Hadamard gate the different alternative outcomes are then recombined again. This represents the underlying idea of quantum algorithms in general.

If extended to n input qubits the algorithm is usually called Deutsch – Jozsa algorithm [49]. Still it is capable to tell the answer with only once evaluating $f(x_1, \dots, x_n)$! That compares to $2^n/2 + 1$ queries a classical computer would need [13]. Although there is no known application for this algorithm and a probabilistic calculation would be much faster than the deterministic upper limit for the classical computation given above, it is an important example and represented the outset of more use- and powerful quantum algorithms.

2.2 Superconducting Charge Qubit

Two main roads of experimental implementations for qubits have been followed. First, microscopic quantum systems like atoms and ions have been considered. Presently the most advanced qubit implementation is based on ions in linear traps, coupled to their longitudinal motion and addressed optically, see [43, 50]. Their main advantage is long coherence times but their scalability is somewhat questionable, see [51] for a recent miniaturization approach. The second main road investigated are micro-fabricated electronic circuits. They bring a lot of flexibility in terms of their fabrication but coherence is limited to some degree as their complexity always involve a macroscopic number of atoms and electrons.

Again, also in this direction, there are two main approaches based on quantum states of either single particles (single electron spin states, single electron orbital states) or macroscopic quantum states of the whole circuit. Microscopic states have shown long coherence times at low temperatures, however operations on single particles are difficult to perform. The second approach are superconducting circuits based on Josephson junctions, which form an artificial atom the Hamiltonian of which can be tailored almost at will and a direct electrical readout can be incorporated in the circuit. Although coherence times do not yet compare to that of natural atoms or of spins, the NEC group achieved to successfully perform a 2-bit logical operation using solid-state qubits in 2003 [52]. In the recent years considerable progress has been made with relevant coherence times of the quantum states now extending to the microseconds range [45, 46, 53, 18, 19].

Criteria for 'good Qubits'

Not all two level systems are suitable for implementing qubits. A series of criteria, summarized by Di Vincenzo, need to be addressed (see e.g. chapter 7 in [13]):

1. The level spectrum should be sufficiently anharmonic to provide a good two level system.
2. An operation corresponding to a 'reset' is needed.
3. The quantum coherence time must be sufficient for the implementation of quantum error correction codes.
4. The qubit must be of a scalable design with a universal set of gates.

5. A high fidelity readout method is needed.

Sometimes there are two additional criteria added, namely:

6. The ability to convert stationary and flying qubits.
7. The ability to faithfully transmit flying qubits between specified locations.

The requirement on the coherence is measured by the number of gate operations that can be performed with an error small enough so that error correcting codes can be used. This requirement is extremely demanding as less than one error in $\sim 10^5$ gate operations is required [13].

It is the superconducting charge qubit approach that is discussed in this thesis which has the potential to fulfill all required criteria. As we will see, the setup copes with criteria 1, 2 and 4 very well, while point 3 and partly 5 still have to be improved. Also the two additional criteria 6, see [3, 54, 55], and 7, see [18, 19] as well as experiments of the groups at Yale and NIST (unpublished), have been solved in the presented system which should enable the implementation of very interesting hybrid systems in the future.

2.2.1 Josephson Tunnel-Junction

Purely linear components are not sufficient for quantum signal processing as one needs an anharmonic level spectrum. Anharmonicity is crucial in order to be able to address two specific states unambiguously, representing the desired two-level system. In addition, the non-linear elements needed must be non-dissipative in order to ensure long coherence times. Elements like diodes or CMOS transistors are thus unsuitable even if they could be operated at ultra-low temperatures.

Ultra-low temperatures are needed for two reasons. Electronic signals have to be carried from one part of a chip to another without energy loss. Furthermore, energy has to be contained in the qubit itself without transferring it anywhere. These are necessary preconditions for conservation of quantum coherence. Superconductors provide us with the necessary properties of ultra low dissipation. Low temperature superconductors like aluminum or niobium are ideal for this task. The second reason for ultra low temperatures concerns thermal fluctuations. The energy quantum associated with the transition between the states $|0\rangle$ and $|1\rangle$ that is $\hbar\omega_{01} \equiv \hbar\omega_a$, has to be much greater than the thermal fluctuations in the quantum integrated circuit with the typical energy $k_b T$. We will see that the transition frequency for superconducting qubits is in the range of 5-20 GHz which means that T is required to be less than 20 mK in order to be sure that no higher energy states are occupied. While the chip can be cooled to such a temperature with a dilution refrigerator, it is important not to forget that the effective temperature of the electromagnetic fields connected to the chip must also be cooled to these low temperatures by means of careful electromagnetic filtering.

There is just one element that obeys both requirements, anharmonic spectrum and non-dissipative operation, and can be operated at arbitrarily low temperatures. A *Josephson junction*

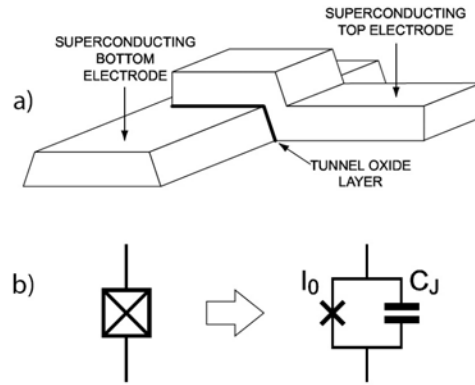


Fig. 2.6: a) Josephson tunnel junction made with two superconducting thin films. b) Schematic representation of a Josephson tunnel junction. The irreducible Josephson element is represented by a cross. Figure taken from [56].

is obtained connecting two superconducting electrodes through a thin isolating layer acting as a tunnel barrier, see Fig. 2.6. On such systems one observes the so-called Josephson effect predicted by B. Josephson in 1962.⁶

Josephson Effect

The effect is an example for a coherent quantum effect in a macroscopic structure. The ensemble of all superconducting electrons (Cooper pairs) in one electrode has to be described by a macroscopic wave-function. If the isolating layer is sufficiently thin, usually on the order of 1-2 nm, the two wave-functions describing the collective electron state in the two electrodes are overlapping in the area of the barrier, thus coupling weakly and leading to the Josephson-behavior described below [57, 58].

The DC Josephson effect describes the fact that, even without external electromagnetic fields applied, there can be a super-current across the junction. The super-current density in the contact is given by

$$J_s = J_c \sin \varphi, \quad (2.21)$$

where J_c denotes the critical current-density of the junction and φ the gauge invariant phase difference of the two macroscopic wavefunctions describing the Cooper pairs in the two superconducting electrodes. It is to note that the critical current density scales exponentially with the barrier thickness, which makes it probably the most important fabrication parameter. If J_s gets integrated over the area of the junction we obtain the weak-link current-phase relation

$$I_s = I_c \sin \varphi, \quad (2.22)$$

where I_s denotes the super-current across the contact and I_c the maximal current that can be carried as a super-current.

⁶Together with R. Doll and M. Nubauer he received the Nobel-prize in 1972 for his discovery.

The AC Josephson effect states that the phase difference φ will change in time with an externally applied voltage V

$$\frac{\partial\varphi}{\partial t} = \frac{2\pi}{\Phi_0} V, \quad (2.23)$$

with Φ_0 being the flux quantum $\Phi_0 = h/(2e) \approx 2.07 \cdot 10^{-15} \text{ Tm}^2$. After integration one obtains the voltage-phase relation

$$\varphi(t) = \varphi_0 + \frac{2\pi}{\Phi_0} V t \quad (2.24)$$

where φ_0 is an integration constant. Substituting Eq. (2.24) into Eq. (2.22) one observes that the Josephson-current is oscillating sinusoidal with the Josephson-frequency

$$\nu_J = \frac{V}{\Phi_0}, \quad (2.25)$$

where $1 \mu\text{V}$ is corresponding to about 500 MHz.

Characteristic Energies

Is the externally applied current lower than the critical current I_C there is no voltage drop across the junction, which means that there is in principle no energy dissipated in the contact. Nevertheless, there is energy stored in the Josephson-junction. In order to apply a current I_s that current has to be ramped up starting from $I_s = 0$. During this time the phase φ changes according to Eq. (2.22) hence giving rise to a voltage across the contact, Eq. (2.24). When integrating the product $I_s(t)V(t)$ over that time one obtains the Josephson coupling energy

$$E_j(\varphi) = E_{j_0}(1 - \cos \varphi), \quad (2.26)$$

which denotes the energy due to the overlap of the two wavefunctions in the electrodes. In Eq. (2.26) E_{j_0} is given by

$$E_{j_0} = \frac{\Phi_0 I_C}{2\pi}, \quad (2.27)$$

and called the Josephson-energy. The fact that it is possible to store energy in such a tunnel junction gives rise to it being considered as a nonlinear device. Taking the derivative of the current-phase relation Eq. (2.22) with respect to time we find that it behaves like a nonlinear inductance. With the common relations of induced flux being proportional to current $\phi = L_s I_s$ and the voltage being equal to the changes of the flux $V = d\phi/dt \rightarrow L_s = V/(dI_s/dt)$ we obtain

$$\frac{dI_s}{dt} = I_C \cos \varphi \frac{d\varphi}{dt} = I_C \cos \varphi \frac{2\pi}{\Phi_0} V \rightarrow L_s = \frac{\Phi_0}{2\pi I_C \cos \varphi} = L_C \frac{1}{\cos \varphi}. \quad (2.28)$$

There is another energy that characterizes a Josephson-junction which is its charging energy E_{C_0} . If there is a voltage applied across the contact the energy of the electric field E_{eI} between

the two electrodes forming a capacitor is given by

$$E_{el} = \frac{1}{2}C_{\Sigma}V^2 = \frac{Q^2}{2C_{\Sigma}} = \frac{(2eN)^2}{2C_{\Sigma}} = 4E_{c_0}N^2, \quad (2.29)$$

where

$$E_{c_0} = \frac{e^2}{2C_{\Sigma}} \quad (2.30)$$

denotes the charging energy. $C_{\Sigma} = Q/V$ is the total capacitance of the junction, Q the excess charge and N the number of excess Cooper pairs ($Q = N \cdot 2e$). Josephson and charging energy are the two characteristic energies of a Josephson junction. Their values and in particular their ratio have to be chosen carefully in order to be able to observe coherent quantum phenomena.

The Josephson junction has been described classically up to this point. However, charge and phase are two conjugate variables in the framework of quantum mechanics. The commutator relation for N and φ is given by $[\varphi, N] = i$, or for charge and flux it is $[\phi, Q] = i\hbar$. This is what enables us to engineer quantum bits out of superconducting electronic circuits.

2.2.2 Cooper Pair Box (CPB)

The Cooper pair box design is the prototype of a charge qubit. It was first proposed by Büttiker [59] and realized by the Saclay group in 1997 [60]. Coherent quantum dynamics was first observed in the NEC group [61]. It represents one possible strategy to keep charge fluctuations small while retaining the nonlinearity of the circuit. This is achieved by operating the CPB at the charge degeneracy point – the *sweet spot* [62] – where the transition energy is to first order insensitive to charge noise. Other actively investigated superconducting qubit types include the RF-SQUID (prototype of a flux qubit) and the current-biased junction (prototypical phase qubit).

The Cooper pair box consists of a Josephson junction with critical current I_c and a gate capacitance C_g , where C and R_n model the intrinsic capacity and resistance of the contact, see Fig. 2.7. The part between the gate capacitor and the isolating layer of the junction is referred to as the island of the box, whereas the rest of the electrode represents the reservoir. Cooper pairs may tunnel from the reservoir to the island and back, where $n = N/2$ is the number of excess charges on the island. V_g is an external voltage which serves as a bias parameter. It is applied to the gate capacitor C_g and controls the number of excess charges $n_g = N_g/2$ on the gate capacitor which in turn varies N . In that way it becomes possible to compensate an in practice always present residual offset charge Q_r . Such a Q_r originates e.g. from an excess of charged impurities in the vicinity of one of the capacitor plates relative to the other.

The Hamiltonian of the system can be shown to be [59, 60, 63]

$$H = E_{c_0}(N - N_g)^2 - E_{j_0} \cos \varphi \quad (2.31)$$

where $E_{c_0} = (2e)^2/(2(C + C_g))$ represents the charging energy of the island and $N_g =$

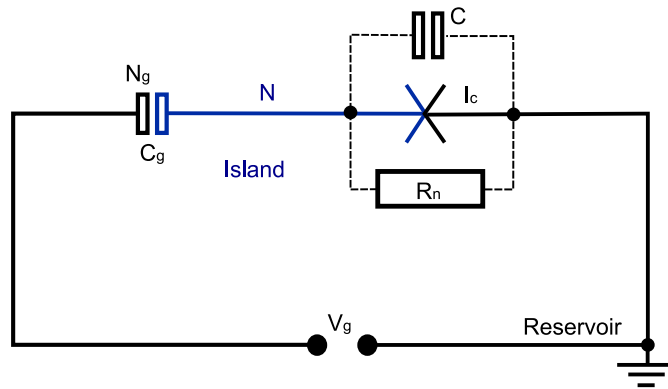


Fig. 2.7: This figure shows the Cooper pair box circuit. The island is printed in blue and the Josephson tunnel junction is modeled with a resistor, a capacitor and the Josephson element itself.

$Q_r + C_g V_g / 2e$ describes the effect of the gate voltage. From this point on Q_r is not considered anymore as its value is dependent on the sample, wiring and temperature (stray electromagnetic fields) and has to be determined experimentally for a given situation anyway. However, noise on this variable is the most important decoherence mechanism which turns out to be the limiting factor of most experiments presented later on.

For $E_{j0} \rightarrow 0$ in Eq. (2.31) one can see that the shape of the dependence of the eigenenergy E of the system vs. gate charge N_g of the system approximates a parabola. Considering the whole Hamiltonian one obtains an energy level diagram shown in Fig. 2.8. The dashed and dotted lines on the right correspond to states where there is exactly one or two excess Cooper pairs on the island respectively. At the crossing of the two parabola the two charge states are energetically degenerate (charge degeneracy point). In the presence of coherent Josephson tunneling through the barrier, those two states ($N = |1\rangle$ and $N = |2\rangle$) couple. This generates a symmetric and an antisymmetric superposition and leads to an avoided crossing at this point, where the minimal distance of the two energy levels is given by the Josephson energy E_{j0} . In this way one obtains a periodic band structure as shown in Fig. 2.8 which approximates a very good two-level system in the vicinity of the charge degeneracy point. The shape of these energy bands is characterized in terms of the ratio E_{j0}/E_{c0} which influences the anharmonicity of the energy ladder but also the sensitivity to charge fluctuations. *Charge qubit* refers to the character of the controlled variable, i.e. the qubit variable that couples to the control line one uses to manipulate the quantum information stored in the qubit.

The two considered excitations are protected from the lossy continuum of normal electron states by twice the gap energy of the used superconductor 2Δ . The charging energy must be taken to be smaller than this superconducting gap in order to avoid unwanted quasi-particles. Finally, of course both, E_{j0} and E_{c0} , have to be larger than $k_B T$ to minimize the impact of thermal fluctuations. The remaining decoherence mechanism in such a charge qubit is given by charge noise and impurities in the box itself, resulting in noise in n_g . At charge degeneracy however the transition energy is insensitive to first order to small fluctuations of n_g , see Fig. 2.8. Operating at this point, sometimes referred to as the 'sweet spot' [62],

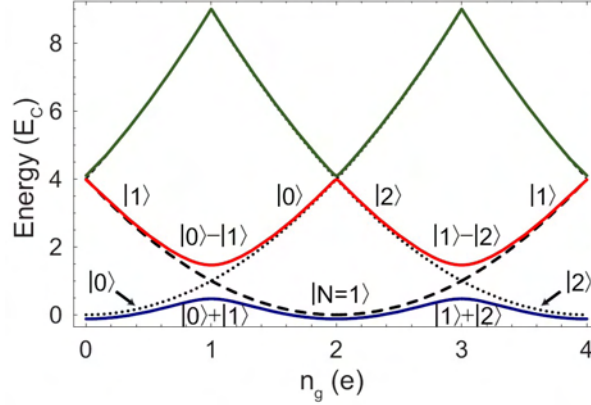


Fig. 2.8: Energy level diagram of the CPB in units of E_{c0} . The blue, red and green solid bands show the ground, and first two excited state energy levels with $E_{j0} = E_{c0}$. Dotted and dashed black lines show the electrostatic energy of the island for 0 and 1 excess Cooper pairs. At $n_g = 1$ (charge degeneracy point) an avoided crossing due to coherent Josephson tunneling occurs. The eigenstates are superpositions of N and $N + 1$ Cooper pairs. Figure taken from [64].

therefore allows for longer coherence times to be observed.

Split CPB

In order to be able to fully control the spectrum of the CPB externally a split CPB was used for the experiments presented. The main difference from the previously discussed circuit is that the tunnel junction between the island and the reservoir is split into two junctions as shown in Fig. 2.9. Using such a setup we can modify the spectrum with the action of two externally controllable parameters: N_g , which is directly proportional to V_g , and E_j , which can be varied by applying a magnetic flux Φ through the loop obtained by the splitting of the junction. E_j is then given by [58]

$$E_j = E_{j0_\Sigma} \cos\left(\pi \frac{\Phi}{\Phi_0}\right), \quad (2.32)$$

where E_{j0_Σ} is the sum of the two individual Josephson energies with their own corresponding phase differences. This model is valid if both Josephson junctions have the same Josephson energies.

CPB in the Charge Basis

We have not yet been considering the fact that the amount of excess charges on the island is actually quantized in units of $2e$, i.e. an integer number N of excess Cooper pairs. The set of states $|N\rangle$ constitutes a basis of the Hilbert space of the box with $\hat{N}|N\rangle = N|N\rangle$. Using this basis we can first write down the electrostatic component (no tunneling) of the CPB

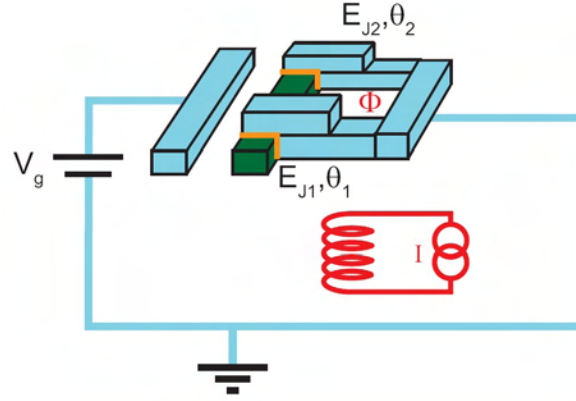


Fig. 2.9: *The Split CPB. The island is connected to the reservoir by two junctions, each with its own Josephson energy and phase difference. The shown setup gives the ability to tune the effective E_{j0} by applying a magnetic flux Φ hence inducing a Zeeman shift. Figure taken from [64].*

Hamiltonian using Eq. (2.29)

$$H_{el} = 4E_{c0} \sum_N (N - n_g/2)^2 |N\rangle\langle N|. \quad (2.33)$$

E_{c0} is given in Eq. (2.30) where C_Σ denotes now the sum of all capacitances of the superconducting island, see Fig. 2.7. Its main components are the capacitance between the electrodes C , the gate capacitance C_g and the capacitance to ground. The term describing coherent tunneling across the Josephson junction in the charge basis can be expressed as [60]

$$H_j = -\frac{E_{j0}}{2} \sum_N (|N\rangle\langle N+1| + |N+1\rangle\langle N|) \quad (2.34)$$

with the Josephson energy from Eq. (2.27). The number operator as written down in this equation allows Cooper pairs to hop on and off the island. Combining Eq. (2.33) and Eq. (2.34) yields

$$H_{CPB} = H_{el} + H_j = \sum_N \left[4E_{c0} (N - n_g/2)^2 |N\rangle\langle N| - \frac{E_{j0}}{2} (|N\rangle\langle N+1| + |N+1\rangle\langle N|) \right]. \quad (2.35)$$

We will focus only on the two lowest energy levels corresponding to the states $|0\rangle$ and $|1\rangle$ and the charge interval $0 < n_g < 2$. For this case it is convenient to choose the reference level for the charge energies to be $E_0 = 4E_{c0}(1 - n_g)^2$ which associates the energies $\pm E'_{el}/2$, with $E'_{el} = 4E_{c0}(1 - n_g)$ to the two states. Note, the two energies $\pm E'_{el}/2$ show a linear dependence upon the gate voltage in the two state approximation considered. In the spin notation this yields

$$H_{CPB} = -\frac{1}{2}(E'_{el}\sigma_z + E_{j0}\sigma_x), \quad (2.36)$$

where σ_x and σ_z are the Pauli matrices. The symmetric and antisymmetric eigenstates of this Hamiltonian may be expressed as [65]

$$|\psi_{s/a}\rangle = \cos\left(\frac{\Theta_m}{2}\right)|0\rangle \pm \sin\left(\frac{\Theta_m}{2}\right)|1\rangle, \quad (2.37)$$

with a mixing angle $\Theta_m = \arctan(E_{j0}/E'_{el})$ between an effective spin- $\frac{1}{2}$ which is σ_z and an effective magnetic field whose components are given by the box parameters E_{j0} and E'_{el} . We see that the ground state (symmetric), as well as the excited state (antisymmetric) of the box, is defined as a superposition state of $|0\rangle$ and $|1\rangle$ with a well defined number of Cooper pairs on the island. In the rotated coordinate system the Hamiltonian of the Cooper pair box becomes simply

$$H_{CPB} = \hbar\omega_a\sigma_z \quad (2.38)$$

with the energy splitting between the symmetric and the antisymmetric eigenstates given by

$$\hbar\omega_a = \sqrt{E'_{el}{}^2 + E_{j0}^2} = \sqrt{(4E_{c0}(1 - n_g))^2 + E_{j0}^2}, \quad (2.39)$$

which shows a hyperbolic gate voltage dependence, asymptotes $4E_{c0}(1 \pm n_g)$ and becomes E_{j0} for $n_g = 1$, see Fig. 2.8. The charge transition matrix element can now be expressed as [64]

$$|\langle g|\hat{N}|e\rangle|^2 \approx \sin^2(\Theta_m) = \frac{E_{j0}^2}{16E_{c0}^2(1 - n_g + E_{j0}^2)}. \quad (2.40)$$

CPB in the Phase Basis

While the charge basis is very well suited to illustrate the states of the CPB, it is not possible to solve the full Hamiltonian Eq. (2.35) analytically. This is because the charge basis is unbounded and discrete. The superconducting phase difference φ in contrast, is continuous and periodic and constitutes the canonical conjugate to charge

$$[\varphi, N] = i. \quad (2.41)$$

We therefore can choose a basis in phase and rewrite the Hamiltonian Eq. (2.35) with the relations $N = i\partial/\partial\varphi$ and $N \exp(i\varphi) = \exp(i\varphi(N + 1))$ with the eigenstates $|\varphi\rangle = \sum_{N=-\infty}^{\infty} \exp(i\varphi N)|N\rangle$ and $|N\rangle = \int_0^{2\pi} d\varphi \exp(-i\varphi N)|\varphi\rangle$ as follows [66]

$$H_{CPB} = 4E_{c0} \left(i \frac{\partial}{\partial\varphi} - \frac{n_g}{2} \right)^2 |\varphi\rangle\langle\varphi| - \frac{E_{j0}}{2} (e^{i\varphi} + e^{-i\varphi}) |\varphi\rangle\langle\varphi|. \quad (2.42)$$

The wave function in phase $\psi_m(\varphi) \equiv \langle\varphi|m\rangle$ is a solution of the time independent Schrödinger equation $H_{CPB}|m\rangle = E_m|m\rangle$, a differential equation which lies in the class of the *Mathieu equations*. They are analytically solvable and their solutions are prepackaged in *Mathematica*, see appendix D in [64] for the specific implementation used.

2.3 On-Chip Microwave Cavity

In order to be able to enter the cavity-QED regime one needs a cavity containing one single harmonic mode which couples to the qubit. Of course there will always be higher order modes, however those can be chosen not to be in the vicinity of the qubit's transition frequency. As it is difficult to realize a true lumped element circuit at microwave frequencies needed for the Cooper pair box qubit – to be considered a *lumped element*, no feature of its structure should exceed $1/10$ of a wavelength at the maximum frequency of its usage – a 1D transmission line oscillator is being used. Such a transmission line can be modeled as a series of LC circuits, realized with a coplanar waveguide and matched to the input and output coaxial transmission lines.

2.3.1 Mapping of Transmission Line Resonance to LC Resonance

Parallel LC Resonator

The equation of motion for the amount of charge on the capacitor in a parallel LCR oscillator as shown in Fig. 2.10a is given by

$$\ddot{q} - \frac{1}{RC}\dot{q} + \frac{1}{LC}q = 0 \quad (2.43)$$

with the solution

$$q(t) = q_0 e^{[i\omega_0 t - \frac{1}{2}\kappa t + \phi]} \quad (2.44)$$

which describes a charge oscillation with frequency $\omega_0 = 1/\sqrt{LC}$ and decay rate $\kappa = 2/RC$. In the frequency domain the circuit may be described by its impedance $Z(\omega)$ which can be written

$$Z_{LRC}(\omega) = \left[\frac{1}{R} + \frac{1}{i\omega L} + i\omega C \right]^{-1}. \quad (2.45)$$

Near resonance this expression may be approximated as, see e.g. [67]

$$Z_{LRC}(\omega) = \frac{R}{1 + 2iQ \frac{\omega - \omega_0}{\omega_0}} \quad (2.46)$$

where $Q = \omega_0 RC = \omega_0 / (2\pi\kappa)$ is the quality factor of the resonator. The quality factor can be thought of as the number of oscillations in a cavity decay time $T_\kappa = 1/\kappa = 2\pi \cdot RC$ before the system comes to equilibrium.

Transmission Line Resonator

A transmission line is often schematically represented as a two-wire line, since transmission lines for TEM wave propagation always have at least two conductors. In the following it is discussed how to use a piece of microwave transmission line as an effective LC resonator.



Fig. 2.10: a) Parallel LCR resonator. b) Transmission line model. Figure taken from [68].

Chapters 2 and 3 of Pozar [67] are a good reference for this section. The properties of a transmission line are characterized by

- its series resistance per unit length R^* in Ω/m due to finite conductance of the two conductors,
- its series inductance per unit length L^* in H/m due to the total self inductance of the two conductors,
- its shunt capacitance per unit length C^* in F/m due to the close proximity of the two conductors
- and its shunt conductance per unit length G^* in S/m due to dielectric losses in the material between the conductors.

Using these characteristic values an equivalent circuit of a transmission line can be developed, see Fig. 2.10b. The impedance of an infinitely long lossy transmission line (LTL) can be written as

$$Z_0 = \sqrt{\frac{R^* + i\omega L^*}{G^* + i\omega C^*}}, \quad (2.47)$$

which for very small losses reduces to $Z_{0, \text{lossless}} = \sqrt{L^*/C^*}$. The complex propagation constant is given by $\gamma = \alpha + i\beta = \sqrt{(R^* + i\omega L^*)(G^* + i\omega C^*)}$, where β , the imaginary part of γ , describes the phase of the wave and the attenuation α is described by the real part of γ . For an open (high) load impedance at the transmission line (TL) in the lossless case one obtains

$$Z_0^{\text{open}} = \frac{1}{\sqrt{L^* C^*}} \frac{n\pi}{l}, \quad (2.48)$$

with l being the length of the TL and n an integer number describing the n -th mode. The input impedance of an open LTL with the boundary condition $l = n\lambda/2$ and λ being the wavelength of the propagating wave is given by

$$Z_{in}^{\text{open}} = Z_0 \coth(\alpha l + i\omega l). \quad (2.49)$$

Around the resonance frequency ω_0 and for small losses α this expression can be approximated as

$$Z_{in}^{\text{LTL, open}} = \frac{Z_0}{\alpha l + i\pi \frac{\omega - \omega_0}{\omega_0}}. \quad (2.50)$$

Mapping Resonances

Comparing Eq. (2.46) and Eq. (2.50) one can see that it is possible to map one model to the other at the fundamental resonance ω_0 with the following substitutions

$$R = \frac{Z_0}{\alpha l} \quad (2.51)$$

$$C = \frac{\pi}{2\omega_0 Z_0} \quad (2.52)$$

$$L = \frac{2Z_0}{\pi\omega_0} \quad (2.53)$$

and the quality factor Q can therefore be written as

$$Q = \omega_0 RC = \frac{\pi}{2\alpha l} = \frac{\beta}{2\alpha}. \quad (2.54)$$

The agreement of these two models is very good and gets better for higher Q , see [68]. Note that the DC-behavior however is not equivalent.

Capacitive Coupling

In order to interconnect the above described circuit with the input and output lines a capacitive coupling has been chosen which allows to keep a relatively high Q . Coupling both, the input and the output of the TL capacitively allows for a transmission measurement. Connecting the LC resonator with a small capacitance causes a large impedance mismatch which is somewhat analogous to a partially silvered mirror reflecting most incident radiation and transmitting a small amount. The modeling of this situation can be done as shown in Fig. 2.11a with G_{ex} being the real part of the inverse of the impedance presented to the resonator at the coupling port (C_κ and R_L in series).

$$G_{ex} = \frac{R_L C_\kappa^2 \omega_n^2}{1 + R_L^2 C_\kappa^2 \omega_n^2} \quad (2.55)$$

with n representing the n -th harmonic of the resonator. An external quality factor can be defined as

$$Q_{ex} = \frac{\omega_n C_n}{G_{ex}}. \quad (2.56)$$

where C_n is defined in Eq. (2.52). For the resonator being symmetrically coupled at the input and output this expression becomes $Q_{ex} = \omega_n C_n / 2G_{ex}$ leading to

$$Q_{ex} = \frac{n\pi}{4Z_0} \left(\frac{1}{C_\kappa^2 R_L \omega_n^2} + R_L \right). \quad (2.57)$$

The loaded quality factor of the resonator Q_L can be found considering G_{int} and the external shunt conductances G_{ex} being in parallel

$$\frac{1}{Q_L} = \frac{1}{Q_{int}} + \frac{1}{Q_{ex}}, \quad (2.58)$$

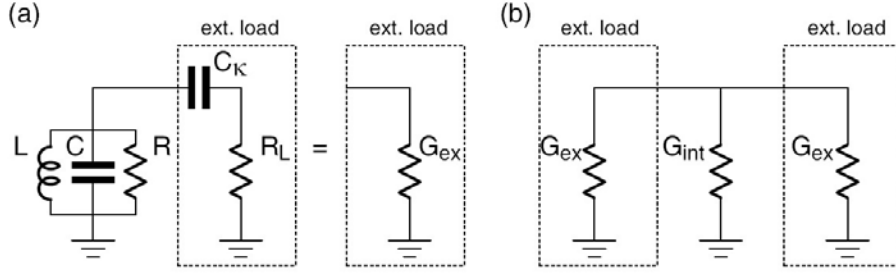


Fig. 2.11: a) LCR resonator coupled by capacitor C_k to load a R_L . b) A resonator that is coupled to both, input and output lines. Figure taken from [68].

with $Q_{int} = \omega_n C_n / G_{int}$ and the coupling coefficient defined as $g = Q_{int} / Q_{ex}$. An appropriate C_k can now be chosen in order to obtain the desired Q_{ex} . For the resonator that was used in the experiments presented, the internal Q was much bigger than the external Q i.e. the actually measured quality factor Q_L was essentially Q_{ex} (overcoupled resonator). Note that the internal Q of a given overcoupled resonator could still be determined via the insertion loss L_0 , i.e. the peak transmission, which is given by $L_0 = g / (g + 1)$.

For similar conclusions on capacitive coupling of a transmission line see reference [68].

2.3.2 Coplanar Waveguide Resonator

At some point one has to decide for a specific geometry of the transmission line. One of the possibilities is a coplanar waveguide (CPW) which is the 2-D version of a coaxial line having the ground in the same plane as the center pin. The gap between them can be chosen in a large range still showing the same impedance – it is the ratio of the center pin width to the gap width that needs to be fixed to keep the impedance fixed. This allows for creation of well localized fields in one region of the chip, e.g. where the qubit is positioned, and less intense fields in another region, e.g. where the dimensions should match with the printed circuit board (PCB). A sketch of a conductor backed coplanar waveguide with its characteristic parameters is shown in Fig. 2.12.

The impedance for such a CPW is given by [69]

$$Z_0^{CPW} = \frac{60\pi}{\sqrt{\epsilon_{eff}}} \left(\frac{K(k)}{K(k')} + \frac{K(k_3)}{K(k'_3)} \right)^{-1} \quad (2.59)$$

with the effective dielectric constant

$$\epsilon_{eff} = \frac{1 + \epsilon_r \tilde{K}}{1 + \tilde{K}} \quad (2.60)$$

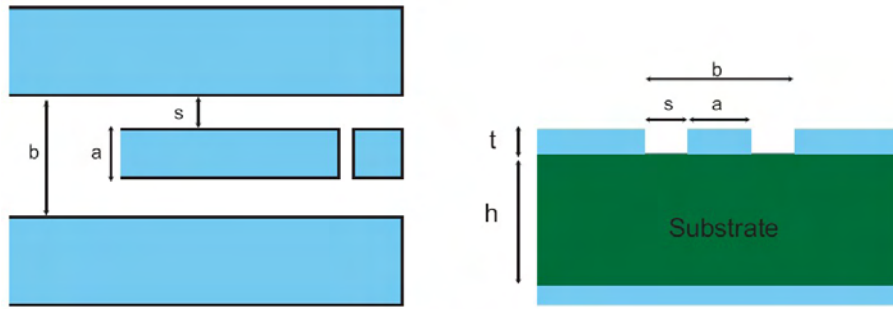


Fig. 2.12: A conductor backed coplanar waveguide. The ratio s/a determines the impedance Z_0 . The length is defined by the position of the gap capacitors. Figure taken from [64].

where K is the complete elliptic integral of the first kind and

$$\tilde{K} = \frac{K(k')K(k_3)}{K(k)K(k'_3)} \quad (2.61)$$

$$k = \frac{a}{b} \quad (2.62)$$

$$k_3 = \frac{\tanh\left(\frac{\pi a}{4h}\right)}{\tanh\left(\frac{\pi b}{4h}\right)} \quad (2.63)$$

$$k' = \sqrt{1 - k^2} \quad (2.64)$$

$$k'_3 = \sqrt{1 - k_3^2}. \quad (2.65)$$

ϵ_r is the dielectric constant of the substrate with height h . For the other dimensions used see Fig. 2.12. Note that the extent of the ground planes should be much larger than s , as they are approximated as infinite.

The speed of propagation through the CPW is $\nu_{eff} = c/\sqrt{\mu_{eff}\epsilon_{eff}}$, where for non-magnetic substrates $\mu_{eff} = 1$. For a finite length l a resonator with resonance frequencies

$$\omega_0^{CPW} = \frac{\pi m}{l} \frac{c}{\sqrt{\epsilon_{eff}}} \quad (2.66)$$

of m -th mode is formed.

2.3.3 Quantization of the LC Oscillator

We have seen that the coplanar waveguide resonator which was used in the experiments can be modeled by an LC resonator. In this subsection such an LC resonator is described in terms of a quantum mechanic oscillator in order to be able to write down the full Hamiltonian of the CQED system in the next section.

The voltage across the oscillator (L and also C) is given by

$$V = Q/C = -L \frac{\partial I}{\partial t} \quad (2.67)$$

and the total energy

$$H = \frac{1}{2}LI^2 + \frac{1}{2}CV^2 = \frac{Q^2}{2C} + \frac{\Phi^2}{2L}. \quad (2.68)$$

where $Q = VC$ is the charge stored in the capacitor and $\Phi = LI$ the flux stored in the inductor. Considering the second formulation of H we see that

$$\frac{\partial H}{\partial Q} = \frac{Q}{C} = -L \frac{\partial I}{\partial t} = -\dot{\Phi} \quad (2.69)$$

$$\frac{\partial H}{\partial \Phi} = \frac{\Phi}{L} = I = \dot{Q} \quad (2.70)$$

which means that Φ and Q are the generalized canonical position and momentum variables of the system with the commutator relation $[\Phi, Q] = i\hbar$. In analogy to the Hamiltonian for a particle moving in a harmonic potential, which is $p^2/2m + \frac{1}{2}m\omega^2x^2$ and the direct mapping $p \rightarrow Q$, $x \rightarrow \Phi$ and $\omega^2 \rightarrow 1/LC$ one can express the Hamiltonian of the system in terms of dimensionless operators similar to the classical case

$$H = \hbar\omega(a^\dagger a + 1/2). \quad (2.71)$$

Here the photon annihilation operator is given by

$$a = \frac{1}{\sqrt{2\hbar Z_c}}(Z_c Q + i\Phi) \quad (2.72)$$

with Z_c being the characteristic impedance of the oscillator $Z_c = \sqrt{L/C}$. In this notation charge and flux are given as follows

$$Q = \sqrt{\frac{\hbar}{2Z_c}}(a + a^\dagger) \quad (2.73)$$

$$\Phi = \sqrt{\frac{2Z_c}{\hbar}}(a - a^\dagger). \quad (2.74)$$

2.4 Circuit Quantum Electrodynamics

Cavity QED is well modeled by the Jaynes-Cummings Hamiltonian. It describes a near-resonant interaction between a two-level atom with a quantized single-mode radiation field, see Fig. 2.13. The Hamiltonian is given by [70]

$$\hat{H}_{JC} = \hbar\omega_r(\hat{a}^\dagger \hat{a} + \frac{1}{2}) + \frac{1}{2}\hbar\omega_a \hat{\sigma}_z + g\hbar(\hat{a}^\dagger \hat{\sigma}_- + \hat{a} \hat{\sigma}_+) + \hat{H}_\kappa + \hat{H}_\gamma, \quad (2.75)$$

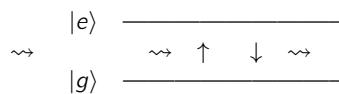


Fig. 2.13: The Jaynes-Cummings model: Two level atom (TLA) interacting with single photons near resonance.

where

$\hat{\sigma}_z = (e\rangle\langle e - g\rangle\langle g)$	paulimatrix
$\hat{\sigma}_- = g\rangle\langle e $	atomic lowering transition operator
$\hat{\sigma}_+ = \hat{\sigma}_-^\dagger = e\rangle\langle g $	atomic raising transition operator
$\hat{a}^\dagger \hat{a} n\rangle = n n\rangle$	number operator acting on field number state
$\hat{a} n\rangle = \sqrt{n} n-1\rangle$	annihilation operator acting on field number state
$\hat{a}^\dagger n\rangle = \sqrt{n+1} n+1\rangle$	creation operator acting on field number state.

The key parameters are the atom-photon coupling constant g , the resonance frequency ω_r and the atomic transition frequency ω_a , see Fig. 2.14. \hat{H}_κ describes the coupling of the cavity to the continuum which causes the photons to leak out at rate $\kappa = \omega_r/Q$. \hat{H}_γ describes the coupling of the atom to modes other than the cavity mode with a corresponding decay rate of the excited state γ . The strong coupling regime is achieved when $g \gg \kappa, \gamma$. This is possible using e.g. high- Q cavities, which means that the coupling between atom and field is significantly strong such that the coherent interaction between the atom and the field dominates over the dissipative one [71, 1, 72].

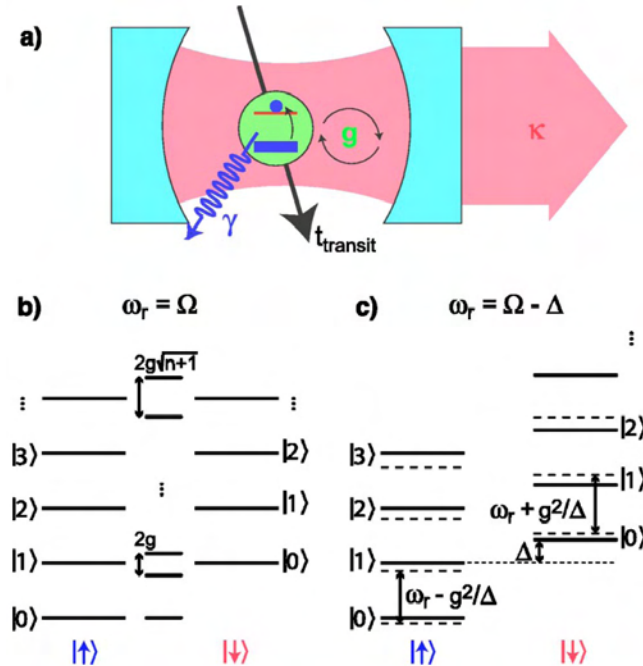


Fig. 2.14: a) The standard version of representing a cavity QED system. An atom (two-level system) with spontaneous decay rate γ passes an optical cavity with decay rate κ . During t_{transit} it interacts coherently with a single mode of the electromagnetic field trapped between the two mirrors where the coupling strength is $g = E_{\text{rms}}d/\hbar$. b) The energy diagram of the uncoupled (left and right) and dressed (center) atom-photon states for $\Delta = 0$. The photon number state is plotted on the vertical axis. c) Energy spectrum in the dispersive regime. The level separation is independent of the photon number n (that is true up to second order of g), but depends on the state of the atom.

In the absence of any damping and for the case of zero detuning $\Delta = \omega_a - \omega_r$ between the atom and the cavity, an initial dressed 'one photon - atom ground state' $|1, g\rangle$ will flop into $|0, e\rangle$ and back at the Rabi frequency $2g/2\pi$, which means that the atom's state and the photon number get entangled. The degeneracy of the two states with n additional photons are then split up by $2\hbar g\sqrt{n+1}$, see Fig. 2.14b from [2]. The value of g is determined by the transition dipole moment d of the atom and the rms zero-point electric field of the cavity mode $g = E_{rms}d/\hbar$.

2.4.1 Coupling of CPB to Cavity

In order to realize the above described situation on a chip, a setup as shown in Fig. 2.14 has been implemented [3]. A Cooper pair box is placed between the transmission line and one of the ground planes, centered between the two gap capacitors where the voltage standing wave amplitude of the first harmonic is largest, see Fig. 2.15 from [3]. The Cooper pairs on the island can Josephson tunnel to the grounded reservoir while they are capacitively coupled to the resonator. The center line of the resonator acts as a gate electrode for the Cooper pairs tunneling back and forth between the island and ground. This allows us to apply a DC voltage at the center pin of the transmission line which couples via the input gap capacitor to the resonator, hence to the qubit via the gate capacitor between island and center conductor of the resonator. This DC gate voltage is used to tune the qubit to its degeneracy point $n_g = 1$ and adjust the desired transition frequency. Furthermore it is possible, and needed, to tune the flux in the split Cooper pair box by applying a B -field perpendicular to the plane of the Cooper pair box loop.

Additionally there is an AC voltage present, arising from each mode of the resonator electromagnetic fields due to the photons in the cavity. This quantum voltage V adds to the effective gate voltage of the qubit $V_g = V_{DC} + V$. We can calculate V with $V = Q/C$ where Q is the charge operator from Eq. (2.73) and $\omega_r = 1/\sqrt{LC}$ the resonator frequency, thus

$$V = \sqrt{\frac{\hbar\omega_r}{2C}}(a + a^\dagger) = V_0(a + a^\dagger), \quad (2.76)$$

with V_0 the rms vacuum fluctuations. If we bias the CPB at the optimal point $n_g = 1$, in the two-state approximation the Hamiltonian representing the coupling of the CPB to the resonator, which is dependent on the qubit state as well as the state of the resonator, is given by

$$H_{coup} = \frac{1}{2}VQ\frac{C_g}{C_\Sigma} = \frac{1}{2}V2eN\frac{C_g}{C_\Sigma} = \frac{1}{2}V_0(a + a^\dagger)2e\sigma_x\frac{C_g}{C_\Sigma} = \hbar g(a + a^\dagger)\sigma_x, \quad (2.77)$$

with

$$g = \frac{e}{\hbar}\frac{C_g}{C_\Sigma}V_0 \quad (2.78)$$

being the coupling constant. The ratio $0 \leq C_g/C_\Sigma \leq 1$ is the coupling capacitance divided by the total capacitance of the CPB. It accounts for the voltage division in the CPB – the

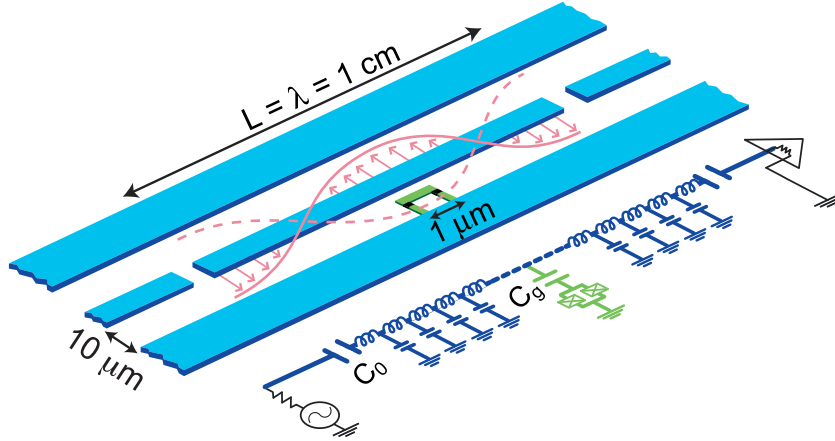


Fig. 2.15: Schematic layout of the implemented circuit QED system [3] with equivalent lumped element representation of the circuit. The Cooper pair Box is placed inside the 1D coplanar transmission line. It is capacitively coupled to the center trace at the maximum of the voltage standing wave of the first harmonic. This yields a strong electric dipole interaction between the qubit and individual photons in the cavity.

fact that part of the voltage V drops from the island to the ground and also across the tunnel barriers, which both do not contribute to the coupling of the CPB and the cavity. $2\hbar g$ therefore represents the energy needed to move one Cooper pair across a portion C_g/C_Σ of the rms vacuum voltage fluctuations V_0 in the resonator. If we now make a rotating wave approximation of Eq. (2.77), which neglects the rapidly rotating terms $a^\dagger\sigma_+$ and $a\sigma_-$, we obtain

$$H_{\text{coup}} = \hbar g(a^\dagger\sigma_- + a\sigma_+). \quad (2.79)$$

The approximation holds as long as the energy of adding a photon or adding a qubit excitation is much larger than the coupling or the energy difference between them [2] $(\omega_r + \omega_a) \gg g, |\omega_r - \omega_a|$.

In order to describe our on-chip CQED system we add the contributions from coupling Eq. (2.79) to that of the resonator Eq. (2.71) and the Cooper pair box Eq. (2.38). With taking decoherence mechanisms of qubit relaxation H_γ , and dissipation (photon leakage) H_κ into account we obtain the Jaynes-Cummings Hamiltonian Eq. (2.75). If we also add a driving rf field ω_d to the resonator near resonantly with the qubit, later on called spectroscopy tone, we obtain in the rotating wave approximation [73]

$$\hat{H} = \hbar\omega_r(\hat{a}^\dagger\hat{a} + \frac{1}{2}) + \frac{1}{2}\hbar\omega_a\hat{\sigma}_z + \frac{1}{2}\hbar\omega_d\hat{\sigma}_x + g\hbar(\hat{a}^\dagger\hat{\sigma}_- + \hat{a}\hat{\sigma}_+) + \hat{H}_\kappa + \hat{H}_\gamma, \quad (2.80)$$

which completely describes the properties of the on-chip CQED system.⁷

We see that the presented setup has a lot of similarities to optical CQED using real atoms and visible photons [71]. Still, there are some fundamental differences, e.g. in atomic CQED the dipole moment constitutes a fixed property of a given atom while in the circuit QED setup the effective dipole moment of the Cooper pair box can be adjusted to give the maximum g for

⁷From this point on the hats indicating operators will be suppressed for reasons of convenience.

any E_{rms} . Additionally the coupling is not limited to some transit time as the artificial atom stays inside the resonator at all times, also e.g. if there are high drive powers applied. Yet another feature of such a qubit-resonator system, is that the presence of the qubit induces a shift of the resonator frequency. This property can be used to do quantum non demolition (QND) measurements [70] of both, the qubit state and the photon-number state. QND refers to measurements that look carefully at one parameter of a system, making sure not to learn anything about the conjugate parameter. This allows for measuring one property of a state repeatedly without destroying it. Such a readout technique was implemented and is discussed in the following.

2.4.2 Readout Scheme

Two limits of a CQED system can be identified. In the resonant regime the atom and photons in the cavity are in resonance therefore being able to exchange energy, forming a strongly coupled system, see Fig. 2.14b. In this limit the two lose their individual character and the corresponding states are entangled. The dispersive limit on the other hand is entered when there are no actual photons being absorbed by the atom, which can be achieved by detuning atom and cavity by $\Delta = \omega_a - \omega_r > g^2$, see Fig. 2.14c. This is the limit in which the experiments presented in chapter 4 of this thesis have been done. Therefore we elaborate on that a bit more.

For g being small compared to Δ the qubit-resonator interaction in the Jaynes-Cummings Hamiltonian Eq. (2.80) (without drive, dissipation and dephasing terms) can be treated perturbatively. The effective Hamiltonian up to second order is then [2]

$$H_{eff} \simeq \hbar/2 \left(\omega_a + \frac{g^2}{\Delta} \right) \sigma_z + \hbar \left(\omega_r + \frac{g^2}{\Delta} \sigma_z \right) a^\dagger a. \quad (2.81)$$

As one can see there is still some interaction between the atom and the cavity in the form of a dispersive frequency shift proportional to g^2/Δ , which commutes with the rest of the Hamiltonian. This means that it conserves both, photon number and atom state. It also tells us that the system behaves like an ordinary resonator with two different frequencies depending on the qubit state.

We end up with an effective atom frequency $\omega'_a \approx \omega_a \pm (2n + 1/2)g^2/\Delta$ depending on n , the number of photons in the cavity, and an effective cavity frequency $\omega'_r \approx \omega_r \pm g^2/\Delta$ dependent on the state of the atom. This shift of the cavity frequency provides the possibility to probe the atom state by measuring the phase of a transmitted microwave. As the peak of the resonator spectrum gets shifted depending on the qubit state, see Fig. 2.16, there is both a phase shift as well as change in the number of transmitted photons. In our setup the phase shift and amplitude of the output signal are measured in order to obtain information on the qubit state. Usually we analyze the phase shift which is expected to be [2] $\delta\Theta = \arctan [2g^2/(\kappa\Delta)]$. A necessary condition in order to be able to resolve the two states nicely is that $\kappa \sim 2g^2/\Delta$ or smaller, which means that the linewidth of the output microwave, i.e. the linewidth of the

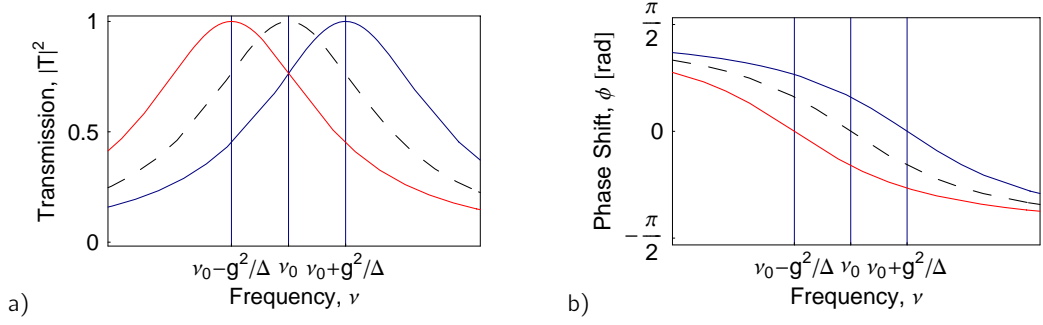


Fig. 2.16: Spectrum of the transmission amplitude a) and phase b) of the measured microwave signal. The dashed line represents the spectral density of the output microwave pulse without the presence of the qubit. The solid lines represent the spectrum of the cavity for the qubit being in the ground state $|g\rangle$ (red) or the excited state $|e\rangle$ (blue). The relative position of the input microwave with respect to the cavity spectrum results in a positive or negative phase-shift of the outgoing microwave. The actual parameters of the shown calculated curves, with Eq. (4.1) and Eq. (4.2), are taken from a resonator measurement presented in section 4.1.1. The coupling strength g was taken from a dispersive measurement, see section 4.1.3.

resonator in our case, has to be at least in the order of the frequency shift that arises when the qubit changes its state from ground to excited state in order to be able to resolve the state change.

Even though the $\langle\sigma_z\rangle$ component of the qubit state remains unaffected by applying this measurement (QND) there will be a strong dephasing ($\langle\sigma_x\rangle$ and $\langle\sigma_y\rangle$ will be changed) at the same time, which in particular affects superposition states. This is the reason why pulsed measurement techniques were incorporated in order to do time-resolved Ramsey and tomography experiments. How this was done is discussed in more detail in chapter 4.

2 Review and Theory

3 Measurement Setup

In this chapter the measurement setup, used and developed for the experiments presented in chapter 4, is described. The realization of the measurement and control circuitry including its characterization as well as the installation of the dilution refrigerator constitutes a significant part of this thesis. Preliminary to the setup of the refrigerator, a new layout for the laboratory was developed. This included vibration measurements and RF-interference measurements, in order to be able to identify the surrounding conditions of future experiments. The planning included computer-aided design, dimensioning and ordering of necessary pumping lines, lifting equipment, support frame and vibration isolations, as well as the necessary microwave frequency equipment. This was followed by a renovation of the laboratory and the assembly of the whole system.

There are basically three technological challenges one has to face in order to be able to observe and make use of coherent phenomena in superconducting circuits. Design and layout of the circuits and their micro and nano-fabrication in appropriate clean room facilities constitutes the first crucial issue. The design considerations for the manufacturing of the sample used will be discussed in the first part of this chapter. For additional information about the fabrication techniques (device fabrication was not part of this thesis), see e.g. [74] or [64]. Second, in order to suppress thermal excitations in the Cooper pair box the transition frequency is in the microwave range and since we want to measure interactions with single photons at these frequencies, one has to deal with GHz frequency signals at extremely low powers which implies appropriate wiring, electromagnetic shielding, careful filtering and mixing techniques, high sampling rates and a full characterization of the rf-equipment in use. The entire data acquisition circuit with all involved microwave components is discussed in the second part of this chapter. Finally, an ultra low temperature environment for the solid state systems has to be created by means of a dilution refrigerator which has to be installed in a low vibrational and high vacuum environment and operated with some care. Some details about the cryogenic setup are presented in the second part of this chapter, while more general information about the working principle, design considerations and operation of a dilution refrigerator can be found in [75] or [76].

3.1 The Sample

The sample used for all presented experiments is similar to the one shown in Fig. 3.1. It was fabricated in the clean room facilities at Yale University in 2004 and was already measured for the results in publication [46]. The sample parameters changed somewhat however, as

there was some additional oxidation of the tunnel barriers in the past two years. For the characterization of the sample and its parameters refer to the results presented in section 4.1.

There are three main components of the sample to identify, namely the split Cooper pair box in blue and the cavity in green, see Fig. 3.1, as well as the printed circuit board (PCB) which is shown in Fig. 3.2. All of them are briefly discussed in terms of crucial design parameters and properties in the following.

3.1.1 Microwave Resonator

The three main design parameters of the coplanar waveguide resonator are the resonance frequency ν_r determined by the length of the resonator, the quality factor Q determined by the size of the chosen gap capacitors and finally the impedance of the circuit which is determined by the ratio of the center conductor width to the size of the gap between the center conductor and the ground planes (taken to be 50Ω). In order to obtain the desired resonator frequency determined by its length, the resonator has to be shaped like a meander which does not harm the transmission properties as long as the curvature is much less than the gap size of the waveguide. The frequency is then given by Eq. (2.66) where ϵ_{eff} denotes the effective dielectric constant of the SiO_2 on Si substrate. Note, there are also geometric components that go into the determination of the effective dielectric constant, see Eq. (2.60).

For large external quality factors the gate capacitors are designed just as a gap in the center conductor. In order to get high coupling on the other hand, the capacitance can be made almost arbitrarily large by designing them as finger capacitors; the minimum spacing is set by the minimal feature size of the optical lithography process. The center conductor width was chosen to be $10 \mu\text{m}$ and, together with the gap, tapered smoothly at the edges of the chip to a width of about $500 \mu\text{m}$ in order to be able to connect the chip to the PCB, using wire bonds, without a large amount of unwanted reflections. Common minimal PCB feature sizes are in the order some $100 \mu\text{m}$ with typical tolerances of $\sim \pm 75 \mu\text{m}$. The fabrication of the resonator has been done with optical lithography, where a lift off process was used for structuring the sputtered niobium on the silicon substrate, see [64] for more information about the involved fabrication steps.

3.1.2 Cooper Pair Box

Also for the Cooper pair box there are three main design parameters, namely the two characteristic energies: Josephson energy E_{J0} and charging energy E_{c0} as well as the coupling strength g , which is related to the voltage division C_g/C_Σ across the box. All desired combinations of those parameters can be implemented with an appropriate geometry.

In the presented experiments the transition energy was essentially defined by the Josephson energy since all measurements, except gate sweeps, were done at the sweet spot and the flux was tuned such that we obtained the minimal detuning between qubit and resonator which in the sample studied was quite large. The transition frequency has to be much larger than

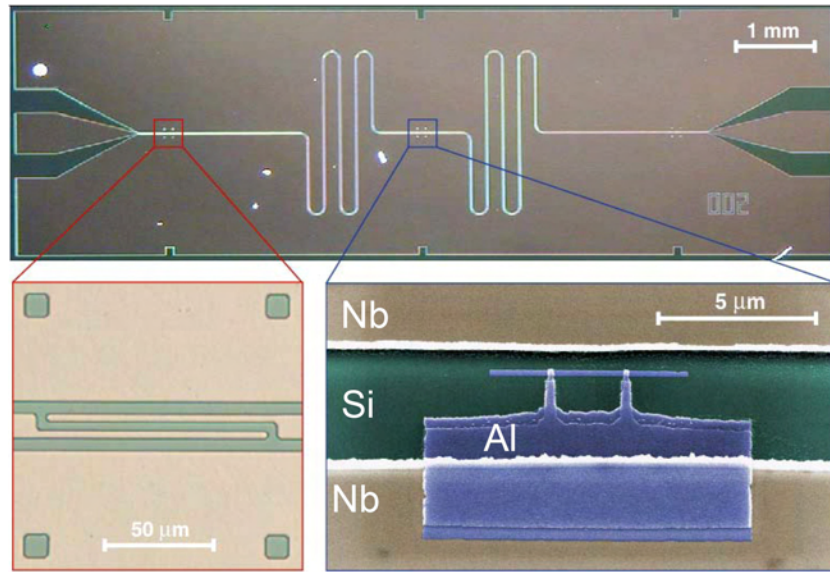


Fig. 3.1: (top) Optical microscope image of the entire chip containing the resonator (niobium) and the Cooper pair box (aluminum). The resonator is made from deposited niobium on a silicon substrate. In the lower left one of the gate capacitors is shown. Finally in the lower right a false colored SEM image shows the split Cooper pair box made from aluminum. The two aluminum-oxide tunnel barriers are right where the reservoir is connected to the island (top bar). The superconducting island is capacitively coupled to the center pin of the coplanar waveguide resonator – there are no wires connected to the CPB.

the thermal energy scale $k_b T$, however it has to be small enough so the necessary microwave engineering does not become a major problem. Reasonable values for the Josephson energy therefore are in the order of 4-8 GHz corresponding to 200-400 mK. In order to achieve such Josephson energies one has to fabricate sub-micron, $\sim 150 \text{ nm} \times 150 \text{ nm}$, junctions with a tunnel barrier thickness of some atomic layers (1 - 2 nm), which can be realized with electron beam lithography and special shadow evaporation techniques including an intermediate oxidation step, see [74] for details of the involved fabrication steps.

The charging energy E_{c0} as well as the voltage division C_g/C_Σ , going linearly into the coupling strength parameter Eq. (2.78), are related to the capacitive network formed by the strips of the coplanar waveguide, the superconducting island, the reservoir and the ground planes. This problem can be solved analytically as well as simulated. In the presented sample, the charging energy was on the order of the Josephson energy and the coupling strength was $g/(2\pi) = 20 \text{ MHz}$.

3.1.3 Sample Mount

The main design consideration for the sample mount is the suppression of any electromagnetic stray fields as well as any unwanted reflections due to impedance mismatches in the connections of the circuit. A sample mount of similar design to the one used in [74], made from solid copper and shown in Fig. 3.2, was used to protect the chip from electromagnetic fields and couple the signals to the on chip resonator. Right angle surface mount SMP connectors

3 Measurement Setup



Fig. 3.2: Sample mount made from copper and one cent coin for size scale. Also shown is the chip containing the sample, the PCB and necessary connections.

with good performance up to about 20 GHz were used to direct the signals to the printed circuit board. In order to end up with nicely sealed box and provide good contact between the bottom ground plane of the PCB and the sample holder, suitable bullet connectors were used to connect the semi rigid coaxial lines to the surface mount connectors. On the outside of the cover of the copper box some blind thread holes, for the mounting of a superconducting coil used to create magnetic bias fields, were drilled.

Also for the PCB, the main design consideration is the suppression of parasitic resonances due to impedance mismatches. One action is to periodically contact the bottom ground plane with the top ground strips of the PCB with copper vias, cutting down any modes between these two planes up to over 15 GHz. No vias could be fabricated in the silicon substrate of the chip, however the chip was taken to be small enough so the cutoff frequency of such modes are much higher than the operation frequencies. In order to keep the impedance mismatch due to different dielectric constants small, a teflon ceramic based microwave substrate with a high dielectric constant and low losses, was used as a dielectric for the PCB. Finally, the necessary wire bonds between the on-chip wave guide and the PCB waveguide were taken to be as short and as numerous as possible to keep their inductance as small as possible.

3.2 Measurement, Control and Data Acquisition

As discussed earlier, microwaves are applied to the resonator to control the qubit state and a transmission measurement through the resonator is used to read out the qubit state. Classical highly phase coherent microwave signals are generated, modulated, filtered and attenuated in order to obtain a quantized single mode electromagnetic field in the resonator interacting coherently with the qubit. On the output side a number of amplifiers with low noise temperatures as well as a fast ADC data acquisition card are employed to read out the qubit state with high fidelity. Furthermore, specially filtered gate bias and flux bias lines were set up to bias the Cooper pair box. Fig. 3.3 shows the full measurement circuit, Fig. 3.4 the 'real world' setup and Fig. 3.5 images the cryogenic part of the circuit, all of which was built up during this thesis. All crucial elements for every presented experiment are indicated and will be discussed

in the following.

3.2.1 Microwave Circuit

The microwave circuit realized consists of three main ingredients that are discussed in more detail in the following subsections. First the signal synthesis part, where phase coherent signals are generated and subsequently pulse modulated before they enter the dilution refrigerator, see top left section of Fig. 3.3 as well as Fig. 3.4, are discussed. The cryogenic part of the circuit constitutes the second main building block. Here the signals are filtered and attenuated down to powers in the order of some 10^{-18} W before interacting with the qubit. Subsequently these signals are amplified and the cables are routed back to room temperature, shown in the lower part of Fig. 3.3 as well as in Fig. 3.5. Finally the amplified high frequency signals are down-converted to frequencies that can be sampled, averaged and post processed digitally, see top right section in Fig. 3.3, which is described in the last part of this subsection.

Signal Synthesis

Three microwave frequency signal generators from *Agilent* (E8257C) were used to provide classical phase coherent signals¹ of up to 20 GHz (RF, Spec/AC and Spec sources as shown in Fig. 3.3 top left and in Fig. 3.4 top right). In order to be able to modulate the amplitude of these signals with nanosecond resolution, an arbitrary waveform generator from *Tektronix* (AWG520), providing 1GS per second on two independent channels with 10 bit resolution each, and 4 additional digital markers, was employed to provide envelope pulses for the microwave signals. This device is able to store pulse patterns containing 4 million points in total. The pulse sequences were designed in *Mathematica* and transferred into the memory of the AWG via an ethernet connection. Most pulse shapes that were programmed were rectangular with the exception of the Berry phase measurement where relatively slow sinusoidal envelope sequences were necessary. Although sharp square pulses have frequency components in a wide band, which could lead to cross talk between the resonator and the qubit, no gaussian pulses were needed since the detuning between resonator and qubit turned out to be large (~ 1.7 GHz) and the used components – connectors, cables, IQ-mixer – provide a filter effect, due to their finite bandwidth.

In order to be able to apply these pulses phase sensitively, an IQ single-sideband upconverter from *Miteq* (SSM0408LC2MDQ) was used. Such a device has three inputs, the RF input, two separate IF inputs I and Q (DC-500MHz) and one LO output. The modulator consists basically of two conventional microwave mixers and a 90 deg phase shifter. The RF input is split in two and the Q input is mixed with one of the branches. At the same time the I input is phase shifted by -90 deg (for $RF > LO$) and mixed with the second branch before the two are added again at the LO output. The RF input signal is therefore mixed with the I and with

¹Phase noise in CW mode: -115 dBc/Hz at 100 kHz offset in the interesting frequency range of 3.2 GHz to 10 GHz.

3 Measurement Setup

the Q quadrature where one of them is 90 deg out of phase, and finally added together at the output.

Mathematically the I and Q quadratures are interpreted as the two Fourier components of a given periodic signal, where the signal – for the case of a single mode considered – is simply defined by

$$f(t) = A \sin(\omega t + \phi) \quad (3.1)$$

$$= F_I \cdot \cos(\omega t) + F_Q \cdot \sin(\omega t) \quad (3.2)$$

$$= I + Q, \quad (3.3)$$

with

$$F_I = 2/T \int_T f(t) \cos(\omega t) dt, \quad F_Q = 2/T \int_T f(t) \sin(\omega t) dt, \quad (3.4)$$

T any chosen period interval e.g. $0 - 2\pi$ and $\omega = \omega_{IF} = 2\pi\nu_{IF}$ being the angular intermediate frequency with $\nu_{IF} = \pm(\nu_{RF} - \nu_{LO})$ which in principle can be chosen to be zero (homodyne mode), or finite (heterodyne mode). Amplitude and phase of the given signal are now encoded in the two quadratures I and Q with

$$A = \sqrt{F_I^2 + F_Q^2} \quad \text{and} \quad \phi = \arctan(F_Q/F_I). \quad (3.5)$$

The IQ modulator used hence makes it possible to transmit the sine component of a given continuous microwave signal – when a DC pulse at the Q input is applied, or to transmit the cosine component of the given continuous microwave signal – when a DC pulse at the I input is applied, or to transmit both with the amplitudes being proportional to the corresponding IF pulse.² If one applies pulses at a finite intermediate frequency, sidebands at frequencies $\nu_{LO} = \nu_{RF} \pm \nu_{IF}$ are generated at the output of the mixer (as long as they are in the specified frequency band, i.e. 4-8 GHz in our case) and if one does not apply any pulse at all there is ideally zero output signal.

However in reality, the RF to LO isolation was measured to be ~ -40 dB with a typical RF input power of 13 dBm. In order to not apply any signal at all when there is no pulse applied – and thus drive no transitions in the qubit – the on/off ratio, i.e. the ratio of the mixer output with and without a pulse at one of the IQ inputs, must be maximized. This is achieved by the use of the additional one-bit markers the *Tektronix* arbitrary waveform generator (AWG) provides. Two of the four markers, marker 2 and 3, were used like a backup switch, gating the microwave sources shortly before and after each pulse. A pin diode is used in the microwave source to switch on and off the signal with an on/off ratio of well above 80 dB. In accordance to the specifications of the signal generators being externally pulse modulated in such a procedure, a

² Unfortunately this mixer was not meant to be used as a carrier driven device (rather modulation driven) and the specified RF frequencies (4-8 GHz) met not quite our demands. One or both had the effect that the characteristics of the LO output was not quite linear with the IF inputs. For this reason a calibration measurement in amplitude was carried out – its results were taken into account e.g. when designing the pulse patterns in order to do quantum state tomography. However, an additional phase calibration is necessary to do more accurate modulation with this particular mixer.

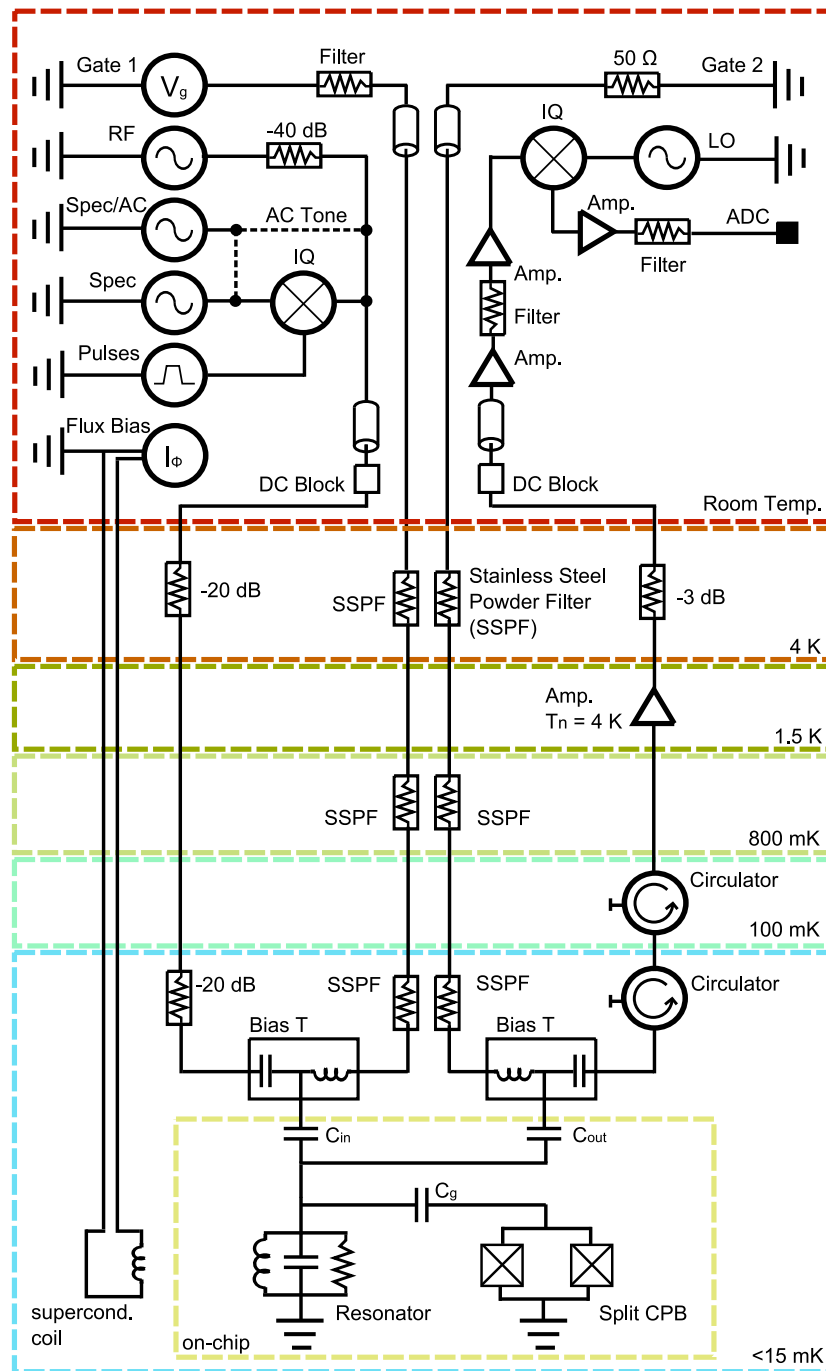


Fig. 3.3: Measurement & control circuitry with the input in the top left section, the output in the top right section and the temperature stages indicated by color. Classical phase coherent signals are generated, modulated, filtered, attenuated, and distributed via different coaxial lines and heat sink at each temperature level before they enter the resonator. After interaction with the CPB, transmission gets amplified with an extremely low noise temperature amplifier before it gets further amplified, filtered and finally measured with a ADC data acquisition card optimized for fast on board averaging. Gate and flux bias lines are also indicated. Thin dashed lines represent flexible coaxial lines which have been connected depending on the specific experiment. The individual components are discussed in the text.

3 Measurement Setup

rise and fall time of the backup pulses of < 6 ns each could be achieved. Marker 4 was used in a similar way to pulse the measurement signal provided by the RF microwave source.

The first marker, served as a master trigger in order to ensure synchronous timing of all involved devices. The ADC data acquisition card as well as the gate bias AWG were triggered with this marker. The trigger signal was split with a *minicircuits* power splitter. The other crucial issue about timing is to lock the phase of all involved microwave, AWG and data acquisition devices. These components were phase locked with a 10 MHz signal provided by a *SRS* rubidium frequency standard in order to ensure the desired phase stability and hence coherence time/length of the generated classical e.m. fields. Slow but still noticeable phase drifts would occur during long measurements if that technique would not be used.

All transmission lines at room temperature indicated in Fig. 3.3 are home made semirigid copper-copper (inner-outer conductor) coaxial lines. Thin dashed lines in Fig. 3.3 represent flexible coaxial lines that were used dependent on the specific experiment.³ The spectroscopy (spec source) and measurement signals (RF source) were generally at different frequencies and added with a *minicircuits* power splitter/adder in the appropriate frequency band indicated with a small black circle. The attenuation on the RF line at room temperature was used to protect the sample from accidentally applied high power signals (the RF measurement signal is usually in resonance with the resonator). Furthermore, a DC block was used to keep the entire experiment dc-isolated from the microwave sources and the pulse generator. Note, also every vacuum line and other connection to the experiment was isolated except for a single well defined grounding in order to avoid the occurrence of ground loops. This was taken to be the grounding-line of the low temperature sensor in the mixing chamber of the dilution refrigerator.

Apart from the pattern file transfer, all communication between the measurement & control PC and the discussed devices was done via their GPIB-interface where *Labview* software was used to automate the measurement procedures as far as possible.

Cryogenics and Filtering

In order to perform the presented experiments at ~ 10 mK, a *Kelvinox 400HA* dilution refrigerator from *Oxford Instruments* was installed (400 μ W, high access). In Fig. 3.4 the implemented setup of the cryostat inside the laboratory is shown. Prior to its installation highly sensitive vibration measurements with μ g resolution by means of geophone sensors have been carried out since the suppression of vibrations is essential to reach ultra low base temperatures. Furthermore, measurements of the electromagnetic spectrum in the laboratory up to low GHz frequencies have been carried out in order to estimate the amount of parasitic e.m. fields that could possibly interfere with the experiments implemented later on.

In the first test run, without the necessary wiring installed, we could reach a stable base

³The ac-tone path was used for the generation of a continuous signal for the two tone sideband spectroscopy experiments presented in section 4.2.2 and the second spectroscopy signal path was chosen for the pulsed off-resonant adiabatic driving during the Berry phase experiment presented in section 4.4.

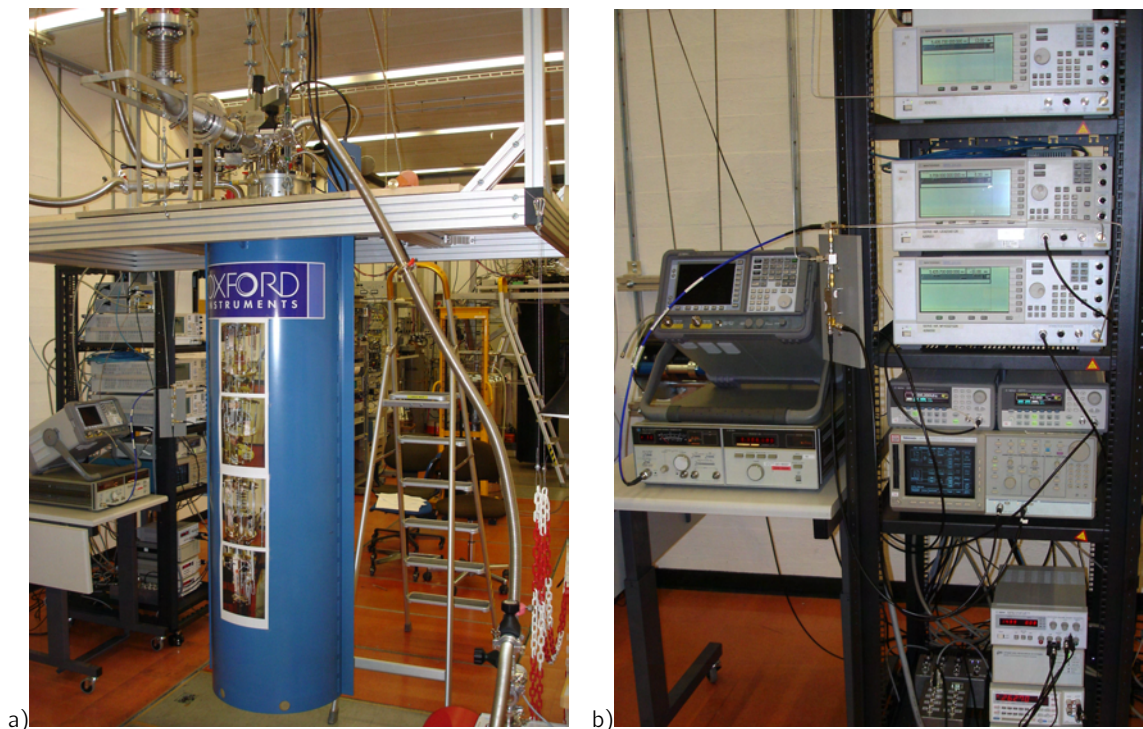


Fig. 3.4: a) The actual experimental setup with the dilution refrigerator dewar in light blue. All infrastructure for the operation of the refrigerator, i.e. pipes, cables, lifting equipment, support frame and vibration isolation (the double gimbal design, see [77]), is mounted on the ceiling of the laboratory to provide maximal access. An about 2.5 m deep pit in the floor together with special lifting equipment allows for the removal of the dewar with the insert and all tubes staying in place. The arrangement of vacuum pumps, liquid nitrogen cold trap, He-mixture dump and gas handling system as well as the electrical infrastructure was positioned in a separate pump cabinet outside the laboratory. b) Electronic equipment used in the presented experiments. Starting from the very top in counter-clockwise order: PC with data acquisition board (not visible), three microwave signal generators, arbitrary waveform generator (AWG) for synchronizing the ADC card, AWG as a gate bias voltage source, Tektronix AWG providing fast pulses, voltage source for cryogenic low temperature amplifier, SRS rubidium frequency standard, a programmable current source for the flux bias, self-made connector box and power source stabilization electronics for the cryogenic amplifier, HP microwave signal generator, spectrum analyzer and in the middle we can barely see the IQ up-conversion mixer as well as some other microwave components such as power splitters and DC blocks.

temperature of <5 mK with this system, measured with a nuclear-orientation thermometer. Typical values for the provided cooling power at the different temperature stages of the installed cryostat are measured $\sim 5 \mu\text{W}$ at ~ 20 mK, typical $400 \mu\text{W}$ at the 100 mK stage (specified), estimated 100 mW at the 1.5 K stage and almost arbitrary cooling power at the 4 K stage. For general principles of cryostat design and operation refer to [75] or [76] and for rather technical details like pumping line layout and the necessary vacuum techniques, which was part of this thesis, see [78]. For the development of an efficient vibration isolation [79] and [77] were very helpful.

The main design considerations for the wiring of such a cryostat, which is shown in Fig. 3.5, is to minimize the amount of heat and noise that reaches the sample while minimizing the attenuation, furthermore also to minimize the amount of noise that is added after the interaction with the sample. It is also important to ensure that the heat loads at different stages

3 Measurement Setup

of the cryostat do not harm its proper operation. In this section the RF input and output lines are discussed, starting with the signal input.

We generate high frequency signals at room temperature – as discussed in the previous chapter – and require only some aW of this signal applied to the sample. In section 4.2.1 we will see that just ~ -145 dBm that is $\approx 10^{-18}$ W are sufficient for measuring, and it turns out that, taking into account the offset from resonance, ~ -60 dBm are appropriate to drive transitions in the qubit with a period of some nano seconds. The noise on the generated signals at GHz frequencies is dominated by Johnson noise, generated by the thermal agitation of charge carriers in the conductor, for all temperatures above 100 mK. In fact, the voltage noise power spectral density in this regime can be estimated to be linear with the temperature $S_{V^2}(\omega) = 4k_bTR$. As the required signals are very low, the most effective way to suppress thermal radiation is to attenuate the signal together with the noise. In order to reduce the room temperature thermal noise, at ~ 300 K, down at liquid helium temperatures, at ~ 4 K, it is therefore sufficient to install a cryogenic attenuator providing 20 dB, that is a factor of 100, of attenuation. For the necessary attenuation between He temperature and base temperature, the consideration with a linear temperature dependance is not valid anymore. For this section of wire the radiation spectrum of a one dimensional black body was calculated and analyzed, particularly the radiation in the frequency band the experiments are operated at. In order to suppress thermal noise arising from temperatures higher than the base temperature, which was typically below 10 mK, another 20 dB attenuator installed at the base temperature stage was found to be sufficient.

Additional attenuation was provided by the coaxial cables as well as the insertion loss of the bias tee and the connectors. In total we estimate the attenuation to be ~ 104 dB for the RF-line and ~ 64 dB on the Spec-lines where the insertion loss of the mixer, which was in the order of 13 dBm dependent on the IQ input, is already included. Much more attenuation would be bad, not only since it would be hard to induce fast qubit transitions, as the speed of the induced transitions scales linearly with the amplitude of the applied signal on resonance, but also because the attenuators would bring additional heat load for the cryostat raising the reachable base temperature. The signal attenuation method for thermal noise reduction only works if the coaxial lines are well thermalized with each temperature stage. The only points where the center pin of the line can be thermally anchored to the surrounding temperature is at the position of the two attenuators since the teflon dielectric in the coaxial lines has extremely low thermal conductance. The shields of the semirigid cables on the other hand are heat sunk at every temperature stage. In order to find a good tradeoff between low heat conductance and low electric losses different coaxial cables were prepared. The used materials for shielding and center-pin were copper-copper at room temperature, stainless steel-copper from room temperature to 4 K and between the different stages at even lower temperatures stainless steel-stainless steel. Inside a given temperature stage the chosen materials were also copper-copper.

At base temperature the DC gate bias, which will be discussed later, and the RF signals are combined by means of a bias tee from *Anritsu* (0.1-40 GHz) before they enter the double

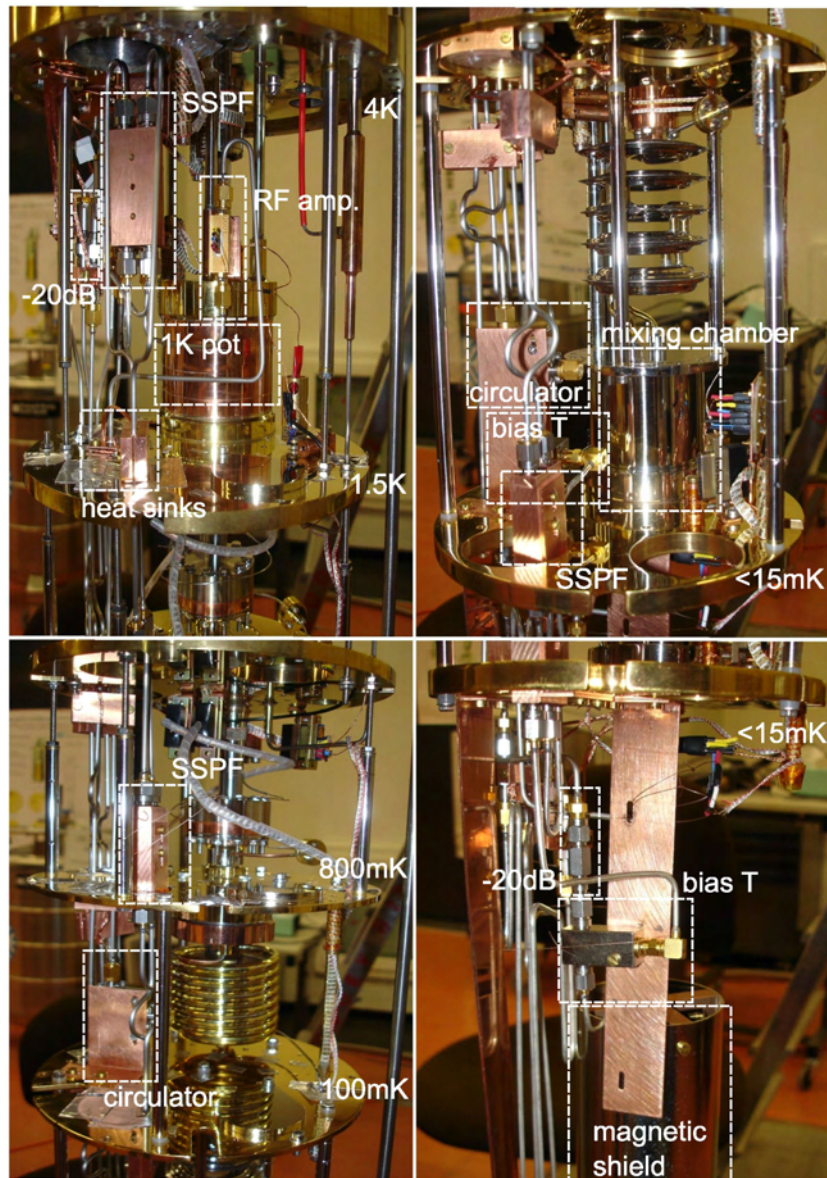


Fig. 3.5: The wiring inside the dilution refrigerator at cryogenic temperatures. Crucial RF and DC components are indicated. Cooling power is obtained in the 1K pot and in the mixing chamber. Heat sinking the coaxial cables properly to every temperature stage and choosing the right materials in order to find a balance between heat conductance and electrical attenuation is essential. The copper sample mount is placed inside the double walled magnetic shield. For the working principle of such a refrigerator see [75] or [76].

walled magnetic shielding made from tempered *Cryoperm*10 from *Vacuumschmelze*, which is soft magnetic at low temperatures, and the sample mount, see also Fig. 3.5. After interaction with the sample, the signals which are in the order of some $\sim 10^{-18}$ W are to be measured. In order to achieve their detection inside the noise added by the amplifier, which has typically larger powers than the signal itself – this is true for extremely low measurement powers corresponding to less than a single microwave photon in the resonator – the signals must reach the first amplifier with the least attenuation possible. Additional damping of the signal

3 Measurement Setup

on this path means affording quadratically more averaging time to retain the same signal to noise ratio (SNR). However, the sample has to be protected also from noise and reflections that could enter the resonator from the output side e.g. noise from the amplifier. In order to achieve that, the signal is directed through two circulators from *Pamtech* which provide an isolation in one direction only. One of the three ports is terminated with a $50\ \Omega$ cryogenic terminator, which makes the circulator acting similar to a one-way microwave valve. Typically the isolation is about 20 dB for one circulator in the specified frequency band (4-8 GHz). A band pass filter for attenuating noise on the other bands was desirable at this point, but was not implemented in the presented setup.

Once the measurement signal passed the two circulators it is taken to the first amplifier, which is mounted on the 1.5 K stage, on the shortest way.⁴ This amplifier has a gain of ~ 35 dB with a noise temperature of only ~ 4 K which is extremely low. This is necessary as the noise that is added to the signal on this first stage will be amplified roughly by another 10 orders of magnitude. The low noise amplifier, which was manufactured at *Caltech*, required a home made voltage stabilized power source and constitutes the central piece of the entire data acquisition circuit. 4 K noise temperature is among the lowest one can obtain with non superconducting amplification techniques. After the first amplification we can afford to insert a 3 dB attenuator for thermal anchoring. It also damps reflections between subsequent amplifiers. Back at room temperature another DC block isolates the experiment from the active components that follow, i.e. two *Miteq* amplifiers with 59 dB measured gain in total. This gain includes another 3 dB attenuator for the reduction of reflections between the amplifiers as well as two filters from *minicircuits* which form a bandpass (3.8 GHz to 6 GHz) that is positioned in between the two amplifiers in order to not saturate the second amplifier with noise in unused frequency bands.

Demodulation, Averaging and Post Processing

The phase and amplitude of the transmitted microwave, which in our case is at ~ 5 GHz, allow us to determine the state of the qubit. In order to be able to analyze GHz frequency signals digitally a technique similar to the one presented in the previous subsection was implemented, i.e. down-conversion of the signals by means of an IQ demodulator. We used an IQ mixer from *Miteq* (IRM0408LC2Q) where the measurement signal gets mixed with a separately generated local oscillator signal, LO in Fig. 3.3 and the HP microwave signal generator in Fig. 3.4 respectively, which is phase coherent and phase locked to the other microwave sources. The LO signal was typically taken to be offset by $\nu_{IF} = 10$ MHz from the actual measurement frequency which was given by the first harmonic of the superconducting resonator. The down-conversion to this intermediate frequency happens phase sensitively in the sense that we have the I and Q quadratures, i.e. the sine and cosine components, of the mixed signals at the output with a frequency of ν_{IF} which can be sampled conveniently. After another stage of

⁴A superconducting coaxial transmission line for this task would increase the observed SNR significantly. They are however difficult to solder which makes it hard to obtain good high frequency transmission properties and mechanical stability.

amplification with a *minicircuits* amplifier (24 dB gain) the signal is back in the millivolts range and after another low-pass filter from *minicircuits* (cutoff frequency of 10.7 MHz), which reduces high frequency noise, the signals are ready to be digitized and averaged with the ADC card.

The PCI acquisition board from *Aquiris* with a maximum sampling rate of 1 GS per second on each of two channels, has fast AD converters and an on-board FPGA hard-coded which is optimized to average the acquired signals in real time. This is particularly interesting as it is extremely large amounts of data that can be acquired in very short time at the high sampling rates used in these experiments. If we did no averaging at all, which is required for single shot readouts of the qubit, it takes about a hundred times longer to get the data into the memory than to acquire it – a very poor duty cycle. When we make use of the provided averaging optimization, which is sufficient for studying ensembles of qubit states, the data transfer time becomes negligible compared to the acquisition time for numbers of averages $\gtrsim 1000$ – in such a way the measurement time is used 100 times more efficiently. The architecture of the board and the available memory of 2 Mpoints (24 bit accumulation memory per channel), allowed for a maximum of 2^{16} averages at the full sampling rate, i.e. 1 GS/s per channel or 2 GS/s on one channel with a resolution of 8 bit. When doing very long acquisitions where a lot of points are averaged, we were limited by the available memory which could in principle be extended however.

Once the data, i.e. the two quadratures, is acquired we want to extract the phase and amplitude information of the transmitted measurement signal. For the case of a homodyne measurement, where the local oscillator is taken to be at the same frequency as the measurement signal, this is easy since the hardware mixed the signal down to DC already. We can simply use the measured DC values of I and Q plug it into the formulas Eq. (3.5) and have the required information. In fact the relative phase of the LO and the RF source can be chosen such, that no post processing at all is necessary since amplitude and phase get directly encoded in I and Q. Homodyne measurement was the method of choice when high timing resolution was required. The resolution was just limited by the sampling rate of the ADC board and the bandwidth of the IQ mixer, i.e. 500 MHz in our case. Every nanosecond we acquired a value for I and Q providing amplitude and phase. Such a procedure was implemented e.g. to analyze the timing of our pulses precisely.

Although the DC signals are easy to handle they are much more prone to $1/f$ noise and slow drifts. For the regular measurements therefore, we realized a heterodyne data acquisition procedure with an IF frequency of typically $\nu_{IF} = 10$ MHz. One can now think about using either one or both of the two quadratures to reconstruct amplitude and phase digitally. In order not to be that sensitive to offsets and imbalances in the IQ mixer or the rest of the amplification chain it turned out to be an effective method only to sample one of the two quadratures. This goes along with some reduction of bandwidth. While using both channels, similar to the homodyne acquisition, one is just limited by the bandwidth of the IQ mixer, using only one channel means being limited by the chosen IF frequency itself. In a process called

3 Measurement Setup

'single channel digital homodyne', from [64] we acquire a full period of just one IF channel⁵ which in general has the form given in Eq. (3.1), integrate one period digitally to extract the two fourier coefficients given in Eq. (3.4) which in turn yields amplitude and phase Eq. (3.5). In our case, with $\nu_{IF}=10$ MHz and the ADC sampling rate being 2 GS/s, we end up with a sum of 200 points yielding one data-point of amplitude and phase. That is done in a fashion so we still obtain one data-point in amplitude and phase for every nanosecond. The bandwidth however is set by the period of 100 ns.

$\nu_{IF} = 10$ MHz was found to be a reasonable value, first because the time resolution was found to be large enough for the experiments implemented in this thesis, second the frequency is high enough in order to avoid $1/f$ contributions and finally it is low enough to have a lot of integration points which increases the acquisition accuracy. An analysis of this acquisition method was done with *Mathematica*. Regular noise as well as jitter on the measurement signal was simulated, averaged and analyzed. It turned out that the sensitivity to phase noise (jitter) is much larger than to noise in the amplitude of the signal. Also it was found that increasing the number of integrated periods with less integration points (same total sampling rate) does not affect the accuracy of the obtained amplitude and phase. However, if one needs a higher time resolution with the same SNR, one possibility is just to choose ν_{IF} higher and increase the number of averages the ADC takes. In fact even this low intermediate frequency generated too much data in general. In order to decimate the signal averaging of 10 to 50 data points was implemented (digital low pass filter). This constituted the only post processing that was done on any data.

3.2.2 DC Bias Circuits

The dc bias circuitry consists of the gate charge bias line and the flux (current) line used to control the Hamiltonian of the Cooper pair box. Both are shown in Fig. 3.3 and their wiring, filtering and design is discussed in the following.

Gate Charge Bias

The DC lines, which are used to tune the gate charge n_g , require much more power and much less bandwidth, compared to the previously discussed RF lines. In the sample that was studied in this work ~ 0.4 V gate amplitude applied to the input port of the resonator were necessary to add or remove an extra Cooper pair to or from the island. Since the protection from noise and interference, and the suppression of room temperature thermal fluctuations are equally essential in this case, it was required to follow a different strategy in the design of these lines as simple attenuation would leave us with megavolts to generate. Extensive low pass filtering and the use of coaxial lines similar to the RF lines was our approach.

⁵In order to implement this technique an ordinary microwave mixer, without separate IQ outputs, had been sufficient. Note, since we were using an IQ mixer anyway the relative phase between LO and RF sources had to be adjusted appropriately in order to get maximal information in the quadrature that was actually analyzed.

The sample architecture allows us to use two gates by applying a voltage at the center conductor of the RF-input or output lines. These voltages couple via the two gate capacitors C_{in} and C_{out} to the coplanar wave guide center strip which is capacitively coupled to the island of the Cooper pair box with C_g , see Fig. 3.3. In the sample employed the input and output capacitances were symmetric $C_{in} = C_{out}$, therefore we chose to just terminate one of the gate charge bias lines and use the other to apply the necessary voltages.

As a voltage source we use an *Agilent* arbitrary wave form generator, Fig. 3.3 and Fig. 3.4, which enables us to implement relatively fast gate sweeps. Typically we used a triangular DC pulse shape with a period of $\sim 100 \mu\text{s}$, when we measure gate-sweeps. Considering the bandwidth we achieved on these lines and the time resolution of 100 ns, faster sweeps and acquisitions would certainly have been possible. Much faster speeds on the other hand are not suitable, since the qubit as well as the resonator should be able to follow the external bias ideally without any time lag. The output of the AWG is differential and relatively well isolated⁶ which was important to avoid any ground loops and keep the experiment isolated and on one single defined ground. In order to be maximally protected from parasitic interferences and stray electromagnetic fields we used semirigid coaxial lines similar to the ones used for the RF lines. Here the material considerations were basically the same as discussed in the last section.

As most of the thermal noise power of our bias signal is at RF frequencies, we implemented numerous stages of low pass filters to cool the e.m. signal down. The first low pass filter at room temperature (*minicircuits*) has a cut off frequency of 32 MHz. At cryogenic temperatures home made stainless steel powder filters, SSPF's in Fig. 3.3 and Fig. 3.5, at three different temperature stages were implemented. They were made from a copper mount with drilled through-holes with a diameter of ~ 5 mm. The holes were filled with a coiled up constantan wire of about half a meter length which was soldered to two SMA connectors. The holes were filled with finely ground stainless steel powder and the connectors were clotted with the copper mount by means of *stycast*. The powder shows the characteristics of a good insulator at DC, at RF frequencies however it turns out to be very lossy. In fact, we end up with an attenuation of >60 dB starting from 1 GHz for every filter stage. At higher frequencies it is even higher but hard to measure due to a finite background noise level of our network analyzer. The main reason for using this type of filter is to realize large attenuation at the qubit transition frequency. The 3 dB attenuation point was different for the individual filters, however typically ~ 100 MHz which provided a sufficient bandwidth for gate sweeps. The remaining Johnson noise is on the order of 15 nV (for a resistance of 2Ω and $T = 20$ mK) which is negligible compared to the charge noise that is occurring due to charge fluctuations in the vicinity of the qubit. This is even more valid taking into account the voltage division which reduces the voltages the qubit sees by a factor of ~ 1000 due to the large capacitance between the island and ground where most of the applied voltage drops.

The small value which was calculated for the remaining noise on the signal is of course only

⁶We assume that this isolation was not perfect in our case. The low temperature sensor which is very sensitive to extremely little currents showed deviating values for the gate being connected. However, the use of DC blocks on this line was of course not possible.

3 Measurement Setup

true if the DC lines are properly thermalized at the surrounding temperature. Although the stainless steel powder has poor thermal conductivity, which is increasingly true for lower and lower temperatures, we found the chosen setup to work well. That was also achieved by using a preferably long constantan wire to increase the contact surface. The main reason to choose constantan was its property of stable thermal conductivity for changing temperatures.

Flux Bias

In order to induce a defined flux in the split Cooper pair box loop we apply a B-field perpendicular to this loop. This was done by mounting a small superconducting coil at the outside of the cover of the copper sample mount inside the magnetic shielding about 5 mm from the sample. The used wire was *SC-T48B-M0.026mm* from *Supercon* with an outer diameter of 36 μm . The diameter of the coil was ~ 18 mm with 100 turns per layer and 70 layers implemented. The bias lines were common twisted pairs without any filters from room temperature to the sample. Due to field focusing effects, currents of some tens of micro amperes were sufficient to induce single flux quanta. We used a *Yokogawa* voltage source operated as current source to bias the coil. Its output is also differential and isolated in order to keep the experiment on a well defined ground. Due to a huge inductance of $L = 0.78$ H, which makes the coils response to noise very slow hence acting much like a low pass filter itself, no filters or shielding techniques were used for the flux bias lines.

Conclusion

In summary, the necessary prerequisites for the installation of a dilution refrigerator system has been taken care of, while at the same time the microwave measurement, control and data acquisition circuitry was being developed and tested. After the installation of the dilution refrigerator and a first test run together with the manufacturer, wiring, filtering, amplification and sample mount components as well as the sample containing resonator and qubit were integrated into the system. Already in the first cool-down we were able to successfully measure a qubit in the new laboratory.

4 Circuit QED Experiments

After the successful setup of the measurement, control and data acquisition circuitry, the goal was to carry out first measurements of a qubit in the new laboratory at ETH. This required a careful characterization of the measurement setup and the sample used. The first step was therefore to characterize the properties of the sample and test the data acquisition system which was done in spectroscopic measurements for different bias parameters. As a second step various time-resolved measurements have been implemented and realized one by one in order to achieve the coherent control of the qubit state and also to characterize the time domain parameters of the sample. All of the developed techniques were necessary in order to be able to first realize the measurement of the Berry phase in an electrical circuit.

At the outset of this chapter, measurements of the cavity transition spectrum are presented. This is followed by a presentation of the energy level diagram of the Cooper pair box, which is based on spectroscopic measurements. Subsequently, the spectroscopic characterization measurements are presented including the dependance of the qubit transition frequency on its two bias parameters, namely magnetic flux and gate charge, as well as spectroscopic measurement of the qubit level separation. The latter form the basis for the exact determination of the characteristic qubit energies E_{j0} and E_{c0} . For calibrating the measurement beam intensity in terms of the corresponding photon number in the cavity, in the second part of this chapter a measurement of the AC Stark effect is presented. Next, there are spectroscopic results that show two photon induced sideband transitions, which form the basis for the conversion of qubit states into photon states and for the coupling of more than one qubit by means of the cavity.

In the third part of this chapter time resolved CQED experiments are presented, demonstrating the deterministic control over a single qubit state and its high visibility read out by the cavity field. High coherently induced Rabi oscillation frequencies of ~ 50 MHz and long energy relaxation times of $T_1 > 8 \mu\text{s}$ were measured. In order to determine the characteristic dephasing time of the sample, Ramsey experiments were realized. Dephasing times of $T_2 > 700$ ns are demonstrated. It is possible to further increase these dephasing times by a factor of about 3 harnessing spin echo techniques which cancel low frequency noise components on the qubit transition frequency. Finally the implemented pulse techniques are used to show the preparation and full tomography of different quantum states.

By making use of the long dephasing times achieved with the spin echo technique, $T_{2_{se}} > 1.7 \mu\text{s}$, and implementing the developed quantum state tomography for the phase sensitive read out of arbitrary quantum states, as well as incorporating and modulating an additional microwave source thus being able to change the hamiltonian of the system with time, enabled

us to make measurements of the Berry phase. Its first observation in macroscopic superconducting solid state circuits demonstrates the high control and coherence that has been achieved. Furthermore it constitutes a promising candidate for the realization of robust qubit phase gates [8] which are necessary for quantum information processing [13].

4.1 Characterization of the System

All presented experiments have been done on a single sample which is similar to the one shown in Fig. 3.1. Its characteristics are discussed in the following.

4.1.1 Cavity Resonance Frequency and Quality Factor

The resonator frequency response measured in transmission exhibits a Lorentzian line shape, as expected for a driven harmonic oscillator. Its transmission power spectrum is given by [80]

$$P(\nu) = P_0 \frac{\delta\nu_0^2}{(\nu - \nu_0)^2 + \delta\nu_0^2}, \quad (4.1)$$

where $\delta\nu_0$ is the half width at half maximum of the Lorentzian line, ν_0 the bare resonance frequency and P_0 the maximally transmitted power at a given input power. The expected phase shift of the transmitted wave with respect to the incident wave is given by [80]

$$\delta(\nu) = \arctan \left[\frac{1}{\delta\nu_0} (\nu - \nu_0) \right]. \quad (4.2)$$

In order to measure the curve shown in Fig. 4.1a a constant input power of -40 dBm was applied with the RF signal generator as shown in the measurement setup Fig. 3.3. The transmitted amplitude was then measured for different frequencies. More precisely, the I and Q voltage quadratures of the transmitted signal were sampled in Volts at a rate of one sample per ns for 40 μ s separately, see chapter 3 for details, and averaged 10^4 times for each data

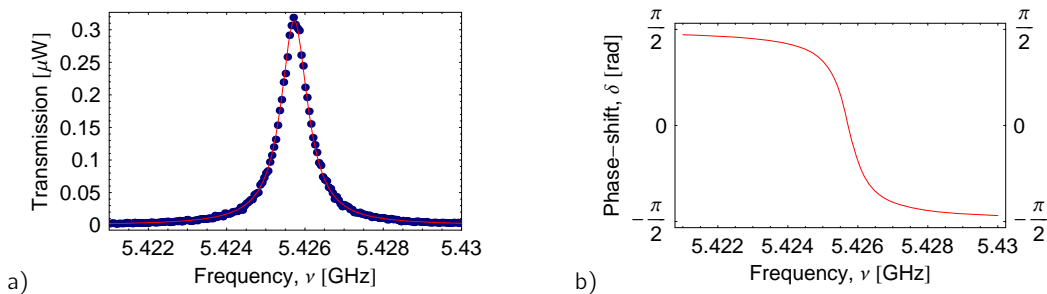


Fig. 4.1: a) Measured transmission spectrum of the coplanar waveguide resonator with the qubit biased away from resonance. The quality factor was determined to be $Q = 6525$ and the resonance frequency $\nu_0 = 5.42573$ GHz. b) Calculated phase shift for the measured resonator spectrum.

point. From that we calculate the transmission power $P(\nu) = (I^2 + Q^2)/R$, with R being the characteristic impedance of the entire measurement circuit $R = 50 \Omega$.

Fitting the obtained curve with the Lorentzian line shape Eq. (4.1) we obtain $\kappa/(2\pi) = 2\delta\nu_0 = 0.83$ MHz and a resonance frequency of $\nu_0 = 5.4257$ GHz, hence the quality factor $Q = \nu_0/(2\delta\nu_0) = 6525$. The calculated phase shift of the transmitted microwave with respect to the incident wave is π at most, see Fig. 4.1b as expected for a resonator and the lifetime of photons inside the cavity is given by $T_\kappa = 1/\kappa \approx 0.2 \mu s$. This measurement has been done with the qubit transition frequency maximally detuned from the resonance by applying a dc-voltage corresponding to one electron to the gate of the qubit (with respect to the sweet spot where the transition energy is minimal). In this case the interaction of the qubit with the resonator is negligible and the bare resonator properties can be determined. How this was done exactly will become more clear in the upcoming sections.

4.1.2 Energy Level Diagramm of the CPB

The Cooper pair box which was placed in the resonator constitutes an ‘artificial atom’ with the band structure shown in Fig. 4.2a. For the calculation of this level diagram, the full CPB Hamiltonian Eq. (2.42) was solved by means of so called Mathieu functions. The qubit parameters used in this plot were obtained in spectroscopic measurements presented in subsection 4.1.4. The lowest 4 energy levels are shown for $0 < n_g < 2$ which is given in units of single electrons and constitutes one period of the band structure. The energy level diagram is shown for the qubit tuned to its maximal Josephson energy, i.e. minimal detuning from the resonator in our case, which experimentally is done by means of an induced magnetic flux. In Fig. 4.2b one can see the energy level separation ν_{01} , ν_{12} , which is very anharmonic in the

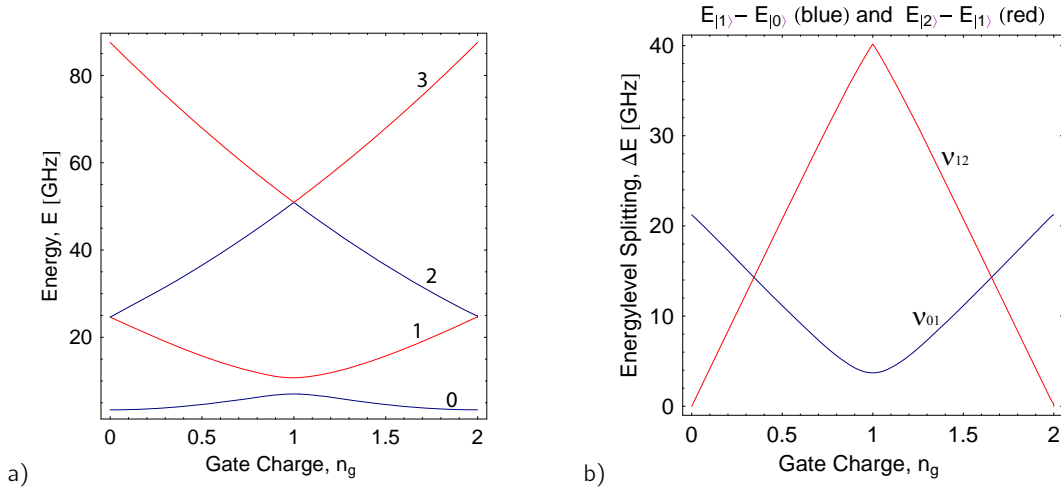


Fig. 4.2: a) Calculated band structure of the measured Cooper pair box with $E_{j0} = 3.709$ GHz and $E_{c0} = 5.24$ GHz from spectroscopic measurements. The lowest four energy levels are shown for one period ($2e$) around the charge degeneracy point $n_g = 1$. b) The energy level splitting between ground and first excited state (blue) as well as first and second excited state (red) is shown. The transition frequency $\nu_{01} = \omega_a/(2\pi)$ at $n_g = 0$ is given by the Josephson energy E_{j0} .

4 Circuit QED Experiments

vicinity of charge degeneracy. This circumstance is required for approximating a good two level system, since it allows for the individual addressing of only one transition, e.g. the first one with corresponding energy ν_{01} . Furthermore, at charge degeneracy the anticrossing of ground and excited state energies due to the coherent Josephson tunneling becomes apparent, see section 2.2.2.

We also note that the characteristic energies of the qubit $E_{j0} = 3.709$ GHz and $E_{c0} = 5.24$ GHz from spectroscopic measurements, and its transition frequencies in particular, see Fig. 4.2b, are much higher than the thermal energy $k_B T$. As a result no excitations due to thermal fluctuations are expected. For a temperature of < 15 mK the thermal energy $k_B T$ is in the order of $1 \mu\text{eV}$ that is about 0.3 GHz at most. The states are also well protected from the upper conductance bands as the quasiparticle gap energy in the used superconductor (aluminum) is much higher than the characteristic energies which avoids the occurrence of quasiparticles. The energy gap 2Δ of aluminium ($T_c = 1.2$ K) is in the order of $350 \mu\text{eV}$, i.e. ~ 4 K, or ~ 85 GHz respectively.

Another feature that becomes apparent in Fig. 4.2b is that the sensitivity of the transition frequency to noise on the gate charge bias is lowest at charge degeneracy [45]. In order to reduce this sensitivity further the group at Yale University investigates the *transmon*, a CPB qubit with huge capacitances of the superconducting island, hence low E_{c0} , therefore high E_{j0}/E_{c0} ratio, which has the effect that the energy bands get extremely flat and insensitive to gate charge fluctuations at the expense of some loss of anharmonicity [81].

4.1.3 Response to Bias

It is discussed in section 2.4.2 that the actual resonator frequency is given by the sum of the bare resonator frequency ν_0 (without the presence of the qubit) plus or minus a dispersive shift due to the presence of the qubit depending on its state $\nu_0 \pm g^2/\Delta$. In fact, the qubit represents a tunable dielectric inside the resonator. Biasing the qubit therefore changes the effective 'optical length' of the resonator - this is being used for the qubit state readout. We call such a procedure a dispersive readout as it measures the electric susceptibility of resonator plus qubit - without leaving any energy behind (QND) [2, 3].

The resonator frequency depends on the state of the qubit $\langle \sigma_z \rangle$, the detuning Δ and the coupling strength g , where the latter two depend on the bias parameters of the CPB. When the qubit is tuned such that its transition frequency approaches the bare resonator frequency, we will observe a dispersive shift of the cavity resonance frequency, resulting in a phase shift of the probe beam, which is taken to be at the bare resonator frequency. When the transition energy approximates the resonator frequency ($\Delta \rightarrow 0$) the shift becomes largest and changes its sign. At $\Delta = 0$ the weak probe beam essentially drives the qubit between ground and excited state.

There are basically two parameters to tune the Hamiltonian of the artificial atom in situ, magnetic flux and the gate charge applied to the qubit. Figure 4.3a shows the measurement response dependent on these two parameters. We see a periodicity in both the gate charge

and the flux bias which is due to the quantization of flux and charge. At low B fields one can vaguely discern a parity switcher resulting in a shadow of the expected pattern, see below. The measurement represents a calibration of both, one flux quantum which required a current of $86 \mu\text{A}$ in small superconducting coil, and an integer gate charge which corresponded to a dc-voltage of 202 mV at the input of the circuit. In Fig. 4.3b the calculated energy level splitting between ground and first excited state is shown. It depends on the gate charge (such as in Fig. 4.2b) as well as on the flux ϕ , which is applied to the split CPB loop via an externally applied current through a superconducting coil. In this calculation E_j , the Josephson energy, is taken to be $E_j = E_{j0} \cos(\pi\phi/\phi_0)$ with ϕ/ϕ_0 being the magnetic flux in units of the flux quantum ϕ_0 . One important feature is the fact that the contrast of the measurement response, which follows the intersecting energy landscapes of resonator and qubit shown in Fig. 4.3b, is maximal at integers of the flux bias and goes to zero for half integers which is due to the vanishing charge transition matrix element of the CPB Hamiltonian, Eq. (2.40) goes to zero for $\phi/\phi_0 = 1/2$.

In the dispersive gate sweep type of measurements shown in Fig. 4.3 and Fig. 4.4 the gate voltage was ramped linearly for $100 \mu\text{s}$ while the transmitted microwave signal at the resonator frequency was converted down to 10 MHz with an IQ-mixer, see section 3.2.1. One quadrature was sampled with a sampling rate of two samples per nanosecond and averaged $2 \cdot 10^4$ and $2 \cdot 2^{16}$ times respectively. From that both quadratures are determined digitally and the phase shift as well as the amplitude are extracted with Eq. (3.5).

The flux bias was applied with a superconducting coil, which was mounted at a distance of about 5 mm from the qubit. Due to a field focusing effect of the superconducting resonator it was sufficient to apply a current of just $86 \mu\text{A}$ to the coil in order to shift the CPB by a single flux quantum. In the regime of low B fields a periodicity of the pattern with one electron is perceptible. Such so called parity jumps were increasingly observed at higher temperatures

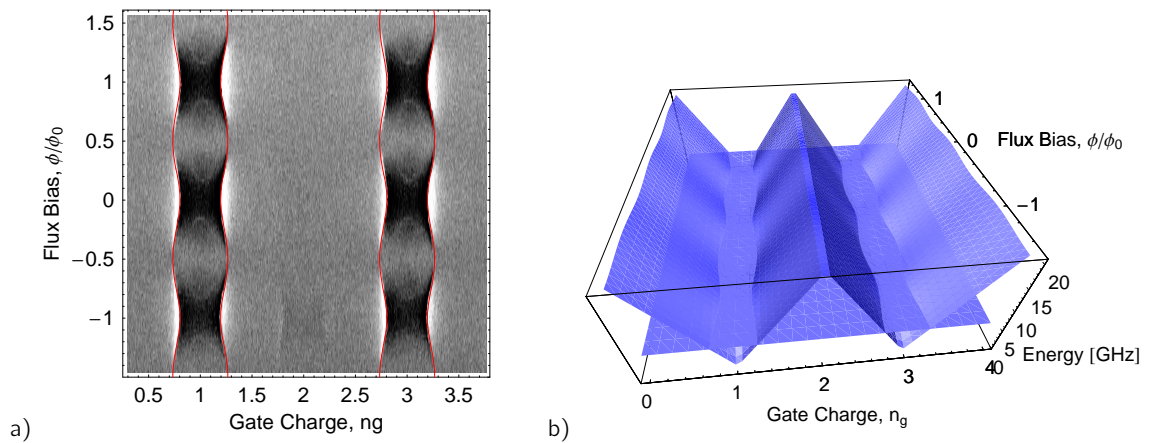


Fig. 4.3: a) Measured qubit response in a dispersive measurement as a function of gate charge and flux bias. b) The energy level landscape of the transition energy between ground and first excited state as well as the resonator energy plane. Their intersection is superposed to the measurement data shown in a) (red). The calculation was done with the full Cooper pair box Hamiltonian Eq. (2.42). The qubit parameters were varied to correspond to the measurement in a).

already by other groups giving rise to the assumption that this is due to a small number of quasiparticles (single electrons) which are free to tunnel resulting in a $1 e$ periodic pattern [82].

As the Josephson energy is periodic in the flux bias and the maximal Josephson energy is below the resonator frequency $E_{j0}/h < \nu_0$ it was not possible to tune this qubit into resonance with the resonator at the sweet spot. Furthermore, the sensitivity to gate charge fluctuations was quite notable for charge bias parameters other than the sweet spot. Thus all measurements presented here were done in the dispersive regime with a minimal possible detuning of the qubit transition energy from the resonator $\Delta = \nu_0 - E_{j0}/h = 1.717$ GHz.

In Fig. 4.3b the energy of the resonator which does not depend on the two bias parameters up to a very large extent is also shown. See e.g. [64] for a brief discussion on the influence of the magnetic field on the resonator properties. The intersection of the qubit energy landscape with the resonator plane is superposed to the data in Fig. 4.3a in red and shows good agreement with the data. Adjusting the two energies in the calculation of this intersection line constitutes a useful means to estimate the qubit parameters E_{j0} and E_{c0} roughly when analyzing a new sample for the first time.¹

In order to understand the measurement response we will now look at a cut where the contrast is maximal, this is where the charge transition matrix element Eq. (2.40) is maximal, see Fig. 4.4. Actually all measurements presented in the following were done in this regime where the number of flux quanta ϕ/ϕ_0 was taken to be an integer, $I_\phi = 262.7 \mu\text{A}$. The gate voltage was ramped linearly and the transmitted microwave signal was analyzed phase sensitive. When the gate voltage is tuned so that the qubit frequency approaches the resonator frequency the frequency shift of the cavity resonance frequency with respect to the probe frequency increases resulting in a phase shift of the probe beam. When the transition frequency of the qubit crosses the resonator frequency the dispersive shift g^2/Δ and hence also the measured phase shift change sign. From this measurement we determine the coupling strength between qubit and resonator to be $g = 20$ MHz.

In order to obtain the theoretical curves shown in Fig. 4.4 one uses the formulas for the resonator transmission Eq. (4.1) and Eq. (4.2), where ν is the probe or measurement frequency which is taken to be the bare resonator frequency ν_0 . The resonance frequency of the cavity now depends on the state of our qubit $\nu_0 \pm g^2/\Delta$ with the detuning from the resonator $\Delta = \nu_0 - (E_{|1\rangle} - E_{|0\rangle})$ plotted in Fig. 4.2 where both g and Δ are dependent on the gate charge. In particular g^2 is proportional to the charge transition matrix element given in Eq. (2.40). The theoretical plots shown in Fig. 4.4 show excellent agreement to the data with the coupling between the qubit and the cavity taken to be $g = 20$ MHz.

¹The parameters that were used here, $E_{j0} = 3.67$ GHz and $E_{c0} = 5.1$ GHz, deviate somewhat from the more accurate determination via a spectroscopic measurement. This is mainly due to the fact that this measurement was taken much earlier than the rest (except the Rabi oscillation measurement), and the properties of the qubit changed at some point suddenly, in particular the transition frequency at the sweet spot E_{j0} increased by about 40 MHz. It is not quite clear what was causing this effect. It could possibly be some mechanism due to a vanishing or appearing vortex in one of the tunnel junctions of the split CPB.

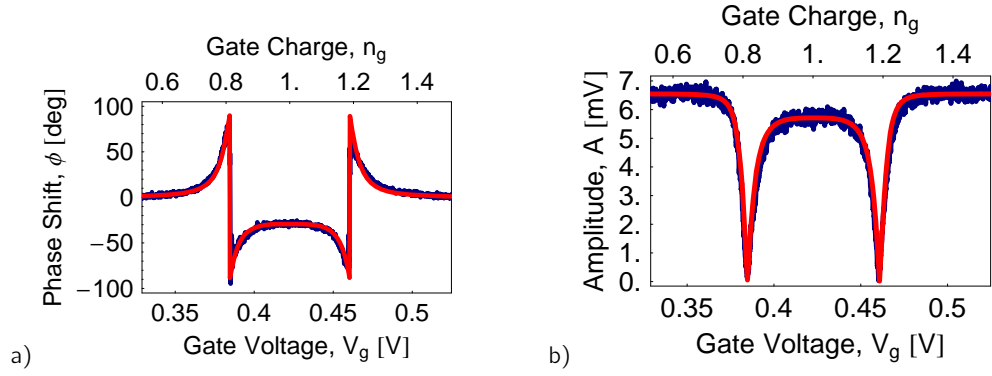


Fig. 4.4: a) Measured phase shift (blue) with respect to gate voltage and theory (red). b) Measured transmission amplitude (blue) with respect to gate charge which has been extracted from the same set of data as in a) and theory (red) with the same parameters as in a).

4.1.4 Spectroscopic Characterization

In the previous measurements we determined the qubit's properties dispersively without any e.m. field driving the qubit, only at $\Delta = 0$ the resonator drive has driven transitions in the qubit. In experiments presented in this section an additional microwave signal is added to the RF input line by means of the spectroscopy generator as shown in Fig. 3.3. In the first plot shown in Fig. 4.5, where this additional drive was applied, we see a measurement that was identically determined to the previous one, with the exception of having taken $5 \cdot 2^{16}$ averages for each data point and an additional microwave drive being applied. The frequency of this driving field was taken to be $\nu_{spec} = E_{j0}/h = 3.704$ GHz, thus inducing transitions between the ground and excited states at the sweet spot $n_g = 1$ where the energy splitting approaches E_{j0} .

We observe an additional peak in the transmitted phase which saturates at 0 degree phase shift at the sweet spot, indicating that the qubit transition saturates and the population in the

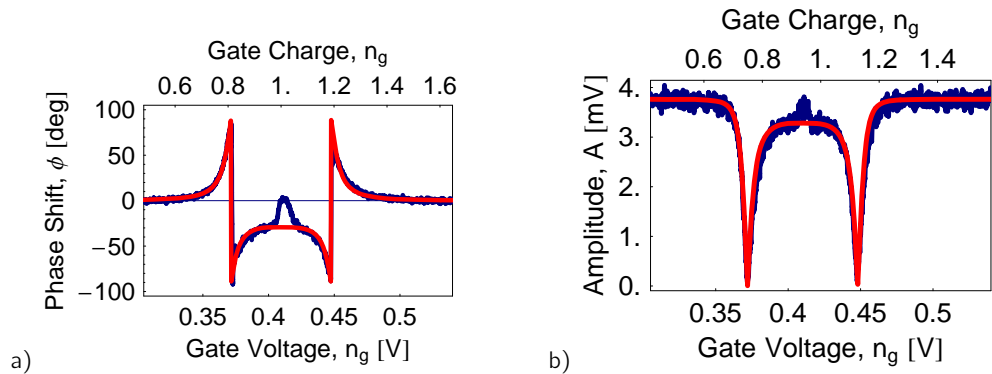


Fig. 4.5: a) and b) A similar measurement to the dispersive gate-sweep presented before with a spectroscopic drive added to the input of the resonator. The frequency of this driving field was taken to be $\nu_{spec} = E_{j0}/h = 3.704$ GHz. The theoretically obtained curves (red) are for comparison and did not take the additional drive into account.

4 Circuit QED Experiments

excited and ground state approaches $1/2$ [83]. This is the maximal population of the excited state that can be achieved by continuously driving at the transition frequency $\nu_{spec} = E_{j0}/h$ with a measured phase shift of 28 degrees with respect to the ground state. The theoretical curves shown in red are for comparison to the un-driven qubit response and did not take the driving field into account. In the obtained amplitude the feature is not that obvious, yet perceptible. The difference in the response of amplitude and phase becomes apparent when one considers Fig. 2.16 which is plotted using the qubit and resonator parameters of the experiments presented. While there is ideally – for ν_0 being sampled with infinitely small linewidth – no variation of the measured amplitude depending on the state of the qubit with the incident probe beam at frequency ν_0 , there is a substantial phase shift $2g^2/\Delta$ between ground and first excited state to be measured. This is the reason for usually taking the phase shift as a marker of the qubit state.

While in section 4.1.3 we were essentially considering the intersection of the transition energy landscape with a plane at constant energy - the resonator, see Fig. 4.3a and b, in Fig. 4.6a we see a sweep at constant magnetic flux ϕ versus spectroscopy frequency ν_s and gate charge n_g . As a first step theoretical curves with the line shape of the energy level splitting between first excited and ground state, as plotted in Fig. 4.2b, were superposed to the data Fig. 4.6a in order to estimate the qubit parameters and determine the interesting data ranges for a

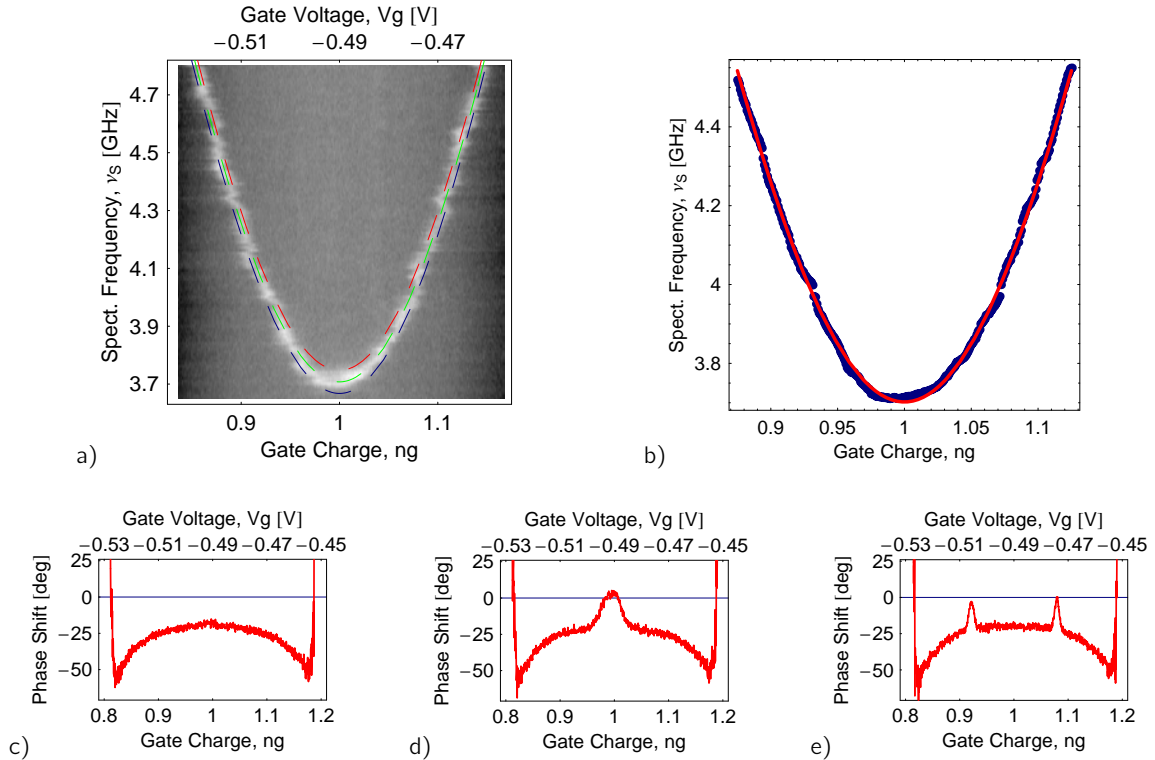


Fig. 4.6: a) Spectroscopic determination of the qubit's transition energy at a constant magnetic flux ϕ which is taken to be an integer of a flux quantum. b) Blue data points show determined positions of fitted peaks of the data shown in a) in frequency direction. The red line is a fit to these extracted peak positions. c) - e) show cuts of the data for spectroscopy frequencies taken to be $\nu_s = 3.665/3.695/4.055$ GHz.

fit. Subsequently peak positions were extracted with individual gaussian fits, which is the expected line shape for high drive powers [4], in frequency direction. The fit to the extracted peak positions is shown in Fig. 4.6b. It shows good agreement with the data and yields the two parameters characterizing the Cooper pair box $E_{j0} = 3.709$ GHz and $E_{c0} = 5.24$ GHz. The only perceptible deviation between fit and data at small spectroscopy frequencies is due to a small drift in gate charge during the data acquisition which took about 10 min for the entire plot. The data was acquired with a 10 MHz resolution in spectroscopy frequency and $2 \cdot 10^4$ averages of each data point.

4.2 Spectroscopic Measurements

In the dispersive limit where the detuning $\Delta = \omega_a - \omega_r$ is much bigger than the vacuum Rabi frequency $2g$, and in particular at low drive and measurement powers, one can study the coupling of cavity photons to the qubit in detail. In the first part of this section the AC Stark effect, i.e. a shift in the qubit transition frequency due to off resonant coupling to a cavity field, is discussed [83]. In the second part spectroscopic measurements on two photon induced sideband processes in the qubit spectrum [7] are presented. Both effects hold the potential to be used creating qubit phase gates allowing the realization of arbitrary rotations around σ_z [6].

4.2.1 AC Stark Effect

After having characterized the Cooper pair box by studying the effect of the qubit state on the resonator frequency, the effect of the cavity photons on the qubit transition frequency is investigated. It turns out that the observation and analysis of the AC Stark effect, see Fig. 4.7 provides a good means to calibrate the measurement power in the presented system and addresses the question of the actual population of the resonator with measurement photons.

In order to illustrate the role of the qubit the CQED Hamiltonian in the dispersive limit

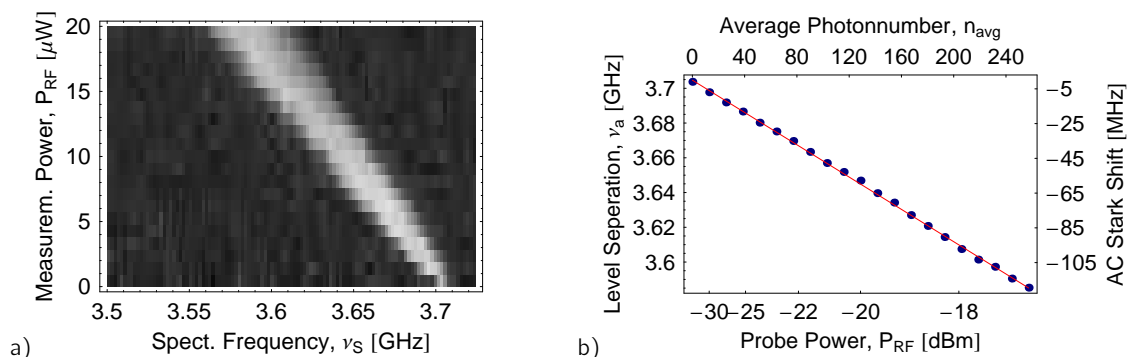


Fig. 4.7: Measurement of the AC Stark effect. a) The transition frequency of the qubit is measured spectroscopically for different probe powers at the resonator frequency. b) Extracted peak positions and linear fit. We see a linear dependence over a large range of intra-cavity photons.

Eq. (2.81) may be reexpressed as

$$H_{disp} = \hbar\omega_r \left(a^\dagger a + \frac{1}{2} \right) + \frac{\hbar}{2} \left(\omega_a + \frac{2g^2}{\Delta} a^\dagger a + \frac{g^2}{\Delta} \right) \sigma_z, \quad (4.3)$$

where the term $\hbar g^2/(2\Delta)$ constitutes the Lamb shift, which takes into account the vacuum fluctuations $\hbar\omega_r/2$ acting on the qubit. The actual atomic frequency in the resonator – the qubit ‘dressed frequency’, can then be expressed as

$$\omega'_a = \omega_a + \frac{2g^2}{\Delta} a^\dagger a + \frac{g^2}{\Delta}. \quad (4.4)$$

Every intra-cavity photon $n = \langle a^\dagger a \rangle$ therefore shifts the transition frequency of the qubit by $2g^2/\Delta$. The transmitted power through the resonator is proportional to the mean number of intra-cavity photons n which hence can be calibrated by the effect, $P = n\hbar\omega_r\kappa$ with the cavity lifetime $1/\kappa$. In Fig. 4.7 the spectroscopically measured qubit line shape in dependence on the measurement power of the probe beam applied at the bare resonator frequency is shown. Depending on the input power, the resonator is populated with less than one photon to up to 240 photons. The shift of transition frequency due to a single photon was determined to be $\Delta\nu_s = 0.46$ MHz and an average population of the resonator with a single photon was reached when applying a measurement microwave power of $P_{\langle n \rangle=1} = -41$ dBm at the spec source output shown in Fig. 3.3.

In the low power limit, the peak width is governed by the grade of saturation determined by the spectroscopy power. At higher photon numbers we observe additional broadening due to a measurement back action process [83, 73]. The quantum fluctuations of the intra-cavity photon field lead to random fluctuations in the qubit level separation, hence to a higher dephasing rate and a broader peak. The linear fit, and therefore also the first order perturbation method used to derive the Hamiltonian in the dispersive limit, agrees well with the presented data over the full range. The powers are consistent with an expected total attenuation of 104 dB, see section 3.2.1, and the determined cavity lifetime $1/\kappa$, see section 4.1.1, since $P_{\langle n=1 \rangle} = h\nu_r\kappa \approx 3 \cdot 10^{-18}$ W, i.e. ~ -145 dBm, which corresponds to the applied power of -41 dBm and the expected attenuation of is ~ -104 dBm. For a more in depth analysis of the AC Stark effect in such a system see [83] and for the range beyond the lowest order dispersive approximation in particular, the discussion in [64]. In order to study the expected line shapes for a coherent driving signal, i.e. Lorentzian for low powers and Gaussian for high powers, refer to [4].

4.2.2 Two-Tone Sideband Spectroscopy

We have already discussed that in the non-resonant limit where ω_a is detuned from the cavity frequency ω_r by Δ the resonant qubit-photon interaction is suppressed. Nevertheless, in a dispersively coupled regime sideband transitions may be used to transfer qubit states to photon states applying fast pulses on one of the sidebands [7]. As shown in Fig. 4.8a, such

transitions are induced by driving the coupled system at its sum $\omega_{blue} = \omega_r + \omega_a$ or difference frequencies $\omega_{red} = \omega_r - \omega_a$ representing the blue $|g, 0\rangle \rightarrow |e, 1\rangle$ and red $|g, 1\rangle \rightarrow |e, 0\rangle$ sideband transitions. Using these transitions, entanglement between the qubit and the resonator could be generated, a process essential for realizing non-local gate operations in a set of qubits coupled to a cavity. The next step of course would then be the generation of qubit-qubit entanglement, e.g. the creation of Bell-states. Pulse sequences with sidebands have been used e.g. for the implementation of a CNOT operation in ion trap systems already [84]. Furthermore single microwave sources and cavity Fock states could be prepared using sideband schemes.

If we use only a single photon transition as shown in Fig. 4.8a in order to access the sidebands, it is not possible to observe them with the qubit biased at its sweet spot, because single photon sideband transitions are forbidden at charge degeneracy [7]. This is because states involved in sideband transitions are of equal parity (with the parity operator $P = e^{-i\pi a^\dagger a}$) and the term in the Hamiltonian describing the drive of these transitions is of odd parity. P therefore anti-commutes with the drive Hamiltonian and the transitions are forbidden to first order. However for a two photon transition the drive Hamiltonian is effectively acting twice and the previous selection rules are therefore simply reversed [6]. Figure 4.8b shows the implemented two tone sideband spectroscopy scheme.

The easiest way would of course be to choose $\delta = \Delta/2$, so the two drive photons are of equal frequency $\omega_{blue,red} = \omega_a \pm \Delta/2$. However, frequencies at such huge detunings from the resonator, in particular in the case of the red sideband, are getting filtered very strongly and it is hard to obtain the required transition rates to achieve saturation, see [7] for the effective Hamiltonian. Instead we chose to add an additional phase coherent drive $\omega_{ac} = \omega_r - \delta$, also shown in the measurement setup Fig. 3.3. Sideband transitions can now be induced as shown in Fig. 4.8b with the only constraint being $\omega_{s_{red,blue}} = \omega_a \pm \delta$.

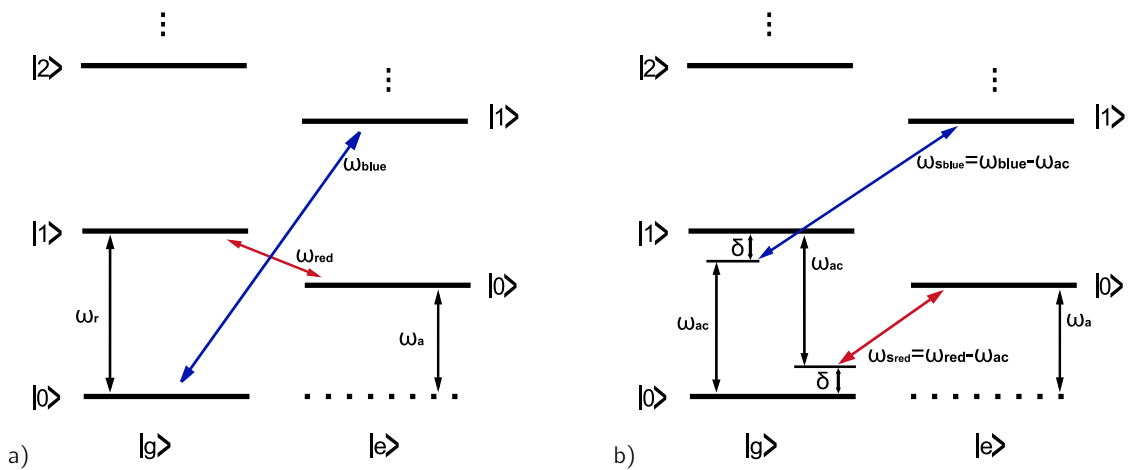


Fig. 4.8: a) Dressed states energy level diagram for the dispersively coupled cavity plus qubit system. The qubit states $|g\rangle$ and $|e\rangle$ are separated by ω_a and the cavity photon states $|n = 0, 1, 2, \dots\rangle$ by ω_r . b) Two-tone scheme for inducing sideband transitions in the presented system. A fixed ac-tone ω_{ac} detuned from the resonator by δ in combination with the spectroscopy tone $\omega_{s_{red,blue}} = \omega_a \pm \delta$ induces sideband transitions.

4 Circuit QED Experiments

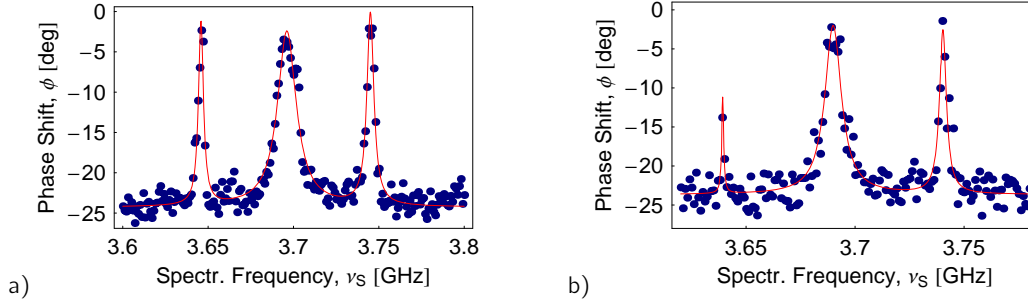


Fig. 4.9: a) Measured cavity phase shift ϕ versus spectroscopy drive frequency $\nu_s = \omega_s/(2\pi)$. The red, blue and fundamental transition peaks are saturated, symmetrically arranged and well resolved. b) Same measurement with less probing power, i.e. an average population of the resonator $n < 1$.

For the measurements presented in Fig. 4.9 the ac-tone detuning from the resonator was chosen to be $\delta = -50$ MHz and the cavity phase shift ϕ was measured versus spectroscopy drive frequency $\nu_s = \omega_s/(2\pi)$. In Fig. 4.9a the red, blue and fundamental transition peaks are well saturated, symmetrically arranged and well resolved. In Fig. 4.9b the same measurement with less measurement power, average population of the resonator taken to be below one photon $n < 1$, is shown. Since we start out the measurement in the qubit ground state and the red sideband to occur requires at least one photon inside the resonator $|g, 1\rangle \rightarrow |e, 0\rangle$, the red sideband is strongly suppressed for this measurement. In Fig. 4.9b therefore, the red sideband almost vanishes due to the lack of intra cavity photons. Note, the SNR is reduced in this measurement due to the low measurement power.

Although the transitions are well resolved and saturated in the results shown above and the rate equations yield a (just) positive answer, see [7] for transition rates, it was not possible to observe sideband Rabi oscillations in a time-resolved measurement. In order to achieve the necessary rates for the observation of sideband oscillations within the dephasing time of the qubit, which is reduced due to the presence of cavity photons, and the lifetime of the photons inside the resonator, very small values for δ and very high input powers, are necessary. This goes hand in hand with various problems including badly resolved peaks hence unintended driving of the fundamental transition, additional AC Stark shifts, which can be compensated in principle, but also a very unstable qubit transition frequency. The high driving powers close to the resonator frequency apparently induce additional noise on the qubit resulting in enhanced charge noise thus lower T_1 and T_2 times. A better understanding of the mechanisms at high powers and a careful design in the next generation of qubits however should allow the time-resolved driving of sidebands. Meanwhile, other interesting measurements in the time domain are being presented here.

4.3 Time Domain Measurements

Up until now we were studying spectroscopic measurements that could tell us basically all parameters that characterize the circuit QED device used in this thesis. In order to make use

of the system for quantum information processing (QIP) it has to be shown that we are able to fully control the Hamiltonian of the single qubit system with fast gate operations. A high fidelity read out technique, as well as full control over a qubit state that shows long coherence times compared to necessary gate operation times is crucial and will be presented.

4.3.1 Rabi Oscillations

The generation and measurement of coherent Rabi oscillations represents just the first step, yet the most important one, towards the coherent control of the quantum state of a qubit. Biasing the qubit at the optimal point and measuring weakly (very low average cavity photon number) and continuously at the resonator frequency ω_r , we drive the qubit with a short microwave pulse close to its transition frequency ω_a , see Fig. 4.10. The response to such a procedure versus time, where the pulse length of the applied pulses Δt is varied in the y-direction is shown in Fig. 4.11a.

In the Bloch-sphere picture the applied microwave pulses induce rotations around either the x or the y-axis, depending on the phase of the applied pulse. It is possible to draw the analogy to a spin- $\frac{1}{2}$ in an external magnetic field with the quantization axis chosen to be σ_z . The Bloch vector precesses with the Larmor frequency $\hbar\omega_a = \mu B$ which is given by the qubit transition frequency and μ being the magnetic moment. In the rotating frame an oscillating field $\omega_d \sim \omega_a$ looks static and drives transitions $B_{xy} \sin(\omega_d t)$ or $B_{xy} \cos(\omega_d t)$ respectively, where B_{xy} is a perpendicular field in the $x - y$ plane. The Hamiltonian illustrating the analogy can be written as

$$H = -\frac{\hbar\omega_a}{2}\sigma_z - \frac{\hbar\Omega_R}{2}[\cos(\omega_d t + \phi)\sigma_x + \sin(\omega_d t + \phi)\sigma_y], \quad (4.5)$$

with Ω_R representing the angular Rabi frequency. In the rotating frame, using the transformation $\psi^{rot} = \exp(-i\omega_d t \sigma_z)\psi$, we obtain

$$H^{rot} = -\frac{\hbar}{2}(\omega_a - \omega_d)\sigma_z - \frac{\hbar}{2}\Omega_R[\cos(\phi)\sigma_x + \sin(\phi)\sigma_y], \quad (4.6)$$

where fast rotating terms were dropped – the rotating wave approximation [70]. On resonance, where $\omega_a = \omega_d$ there is no precession around B_z but a precession around B_{xy} with the Rabi frequency Ω_R . As shown in Fig. 4.11 the angle of rotation was measured to be e.g. $\phi = 2\pi$ for a pulse length of $\Delta t = 21$ ns, see Fig. 4.11c, corresponding to an angular Rabi oscillation

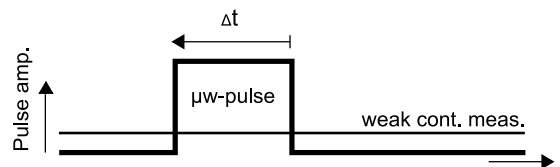


Fig. 4.10: Microwave pulse sequence for the measurement of Rabi oscillations. The measurement signal is taken to be weak and continuous at frequency ω_r . The pulse length Δt of the microwave pulses with frequency $\omega_d \approx \omega_a$ is varied.

4 Circuit QED Experiments

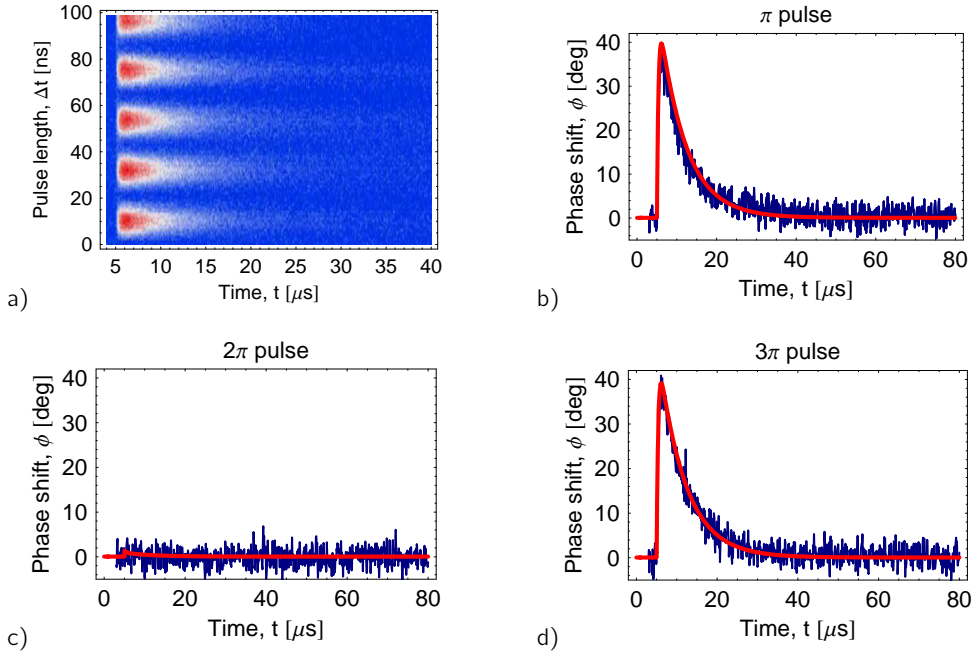


Fig. 4.11: a) Density plot of the measured phase shift of the probe beam versus time. At $t = 5 \mu$ s a near resonant microwave pulse with a variable length was applied. Scaling: blue = 0 deg \rightarrow $|g\rangle$ and red = 40 deg \rightarrow $|e\rangle$. b)-d) show cuts along the time axis for different pulse lengths. We obtain $\pi/2\pi/3\pi$ -pulses (rotation angles on the Bloch-sphere) with corresponding pulse lengths of 11/21/32 ns. The red curves show the expected response inferred from a cavity Bloch simulation.

rate of $\Omega_R = \phi/\Delta t \approx 0.3$ GHz hence the Rabi oscillation frequency is $\nu_R = \Omega_R/(2\pi) \approx 50$ MHz.

The measurement setup as shown in Fig. 3.3 was used for these experiments. The probe signal was continuous with an average photon number of $n \approx 3$ in the resonator, see Fig. 4.10. With reference to a master trigger the data acquisition started at 2μ s and the microwave pulse $\nu_d \approx \nu_a$ with a specific length ended at 5μ s. After a few T_1 times (110 μ s in our case), it is likely that the qubit is in the ground state and the sequence was started again. After averaging the such acquired data points 2^{16} times, the next pulse length was applied until the density plot shown in Fig. 4.11 was obtained.

In order to extract the qubit population from the resonator response which is shown in Fig. 4.12 it is necessary to compare the data to a theoretical model, see the temporal response in Fig. 4.11b-d in red. The model requires the knowledge of E_{j0} , E_{c0} and κ , as well as the coupling strength g and the cavity population $\langle n \rangle$, which were obtained in measurements presented previously. Furthermore the expected qubit relaxation and dephasing rates, which were fitted for the measured data (for the T_2 time see the next section) are required. These parameters are sufficient to simulate the temporal response of the coupled qubit cavity system by solving Bloch-type equations of motion for the cavity and qubit operators, where the Jaynes-Cummings Hamiltonian in the dispersive regime Eq. (4.3) was taken as a starting point [85].

The calculations of the temporal response capture the expected exponential rise in the observed

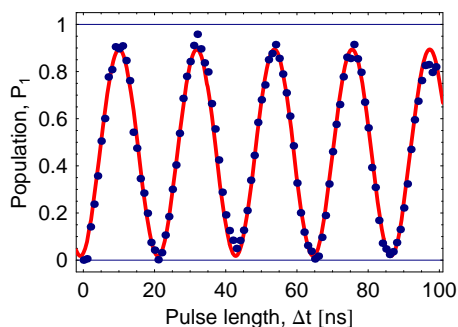


Fig. 4.12: Population of the excited state P_1 versus pulse length Δt . The population was extracted from the measurement shown in Fig. 4.11a. The phase shift response was measured for pulse lengths 0 – 100 ns with a resolution of one nanosecond. The red line is a sinusoidal fit to the extracted data with a Rabi frequency of $\Omega_R/(2\pi) = 46\text{MHz}$ and a visibility of 90%.

phase shift on the timescale of the resonator response time $1/\kappa$ very well, see Fig. 4.11b-d. The finite rise-time is the reason for a reduced maximum response in comparison to spectroscopic results, see Fig. 4.5, where a maximum phase shift response of almost 28 degrees between ground and equal superposition state was measured.² Due to the QND nature of the measurement there is no further systematic influence resulting in a reduction of the measurement response, e.g. relaxation or excitation of qubit states due to interaction with the measurement apparatus. The simulations also accurately model the exponential decay of the measured response signal over the full range of pulse lengths. The qubit energy relaxation was determined to be exponential with the time of a decay by $1/e$ being fitted to be $T_1 > 8 \mu\text{s}$. In order to determine the effective qubit excited state population the scalar product of the obtained data (of a given trace) with the theoretical response, representing a weighting function in this case, was calculated. This takes the systematics of the measurement into account as it ‘weights’ the data points by their expected signal. Finally this result was divided by the scalar product of the theoretical response with itself, in order to normalize to the theoretical line shapes.

The observation of fast Rabi oscillations with a frequency of about 50 MHz³ corresponding to gate operation times of only a few nano seconds was demonstrated. Good visibility $> 90\%$ up to a pulse length of a 100 ns indicates a long dephasing time of the qubit. Together with the measured energy relaxation times $> 8 \mu\text{s}$ ⁴ and the well understood read out technique,

²Note that the Rabi oscillation data presented here, similar to the B field sweeps in section 4.1.3, was taken at the time before a sudden change of the qubit transition frequency of about +40 MHz was observed. For the old set of parameters g was determined to be about 18 MHz (corresponding to about 25 degrees between ground and superposition state), which happens to be the parameter that has the strongest influence in the obtained theoretically calculated cavity response and hence the calculated population. The spectroscopic determination of the coupling strength is not the most accurate however. A direct observation by a vacuum rabi mode splitting measurement is desirable but was not possible as E_{j0} turned out to be too small to enter the resonant limit being biased at the sweet spot with this particular sample.

³Even faster oscillations up to 85 MHz could be observed with the maximal output power of the signal generator, although with less contrast. From a technical point of view however, a corresponding $\pi/2$ pulse of 3 ns is hard to implement cleanly in the current experimental setup.

⁴With measuring at a even lower cavity population $\langle n \rangle < 1$ and hence reduced signal to noise ratio energy

the presented system constitutes a good candidate for carrying out more complicated gate operations sequentially in order to create and control quantum states of qubits in a quantum computer architecture.

4.3.2 Ramsey Fringes

After having shown the ability to manipulate the qubit states with short pulses, more complicated pulse sequences are introduced. In order to study the dephasing time of our sample, a Ramsey experiment was implemented that is presented here.

There are various sources of decoherence to identify in our solid state quantum system; this includes charge fluctuations, trapped vortices, magnetic field noise, paramagnetic and nuclear spins, environmental circuit modes, quasiparticle tunneling due to charge and Josephson-energy fluctuations, emitted and induced photons and phase noise in the driving field [86]. It was already noted that in the experiments presented in this thesis, the main reason for dephasing is charge noise that can be described as fluctuations on the gate charge electrode. The origin of this noise limiting the observed decoherence and dephasing times is not instrumental, it is an intrinsic property of the sample and the materials used. This noise randomly modifies the effective transition frequency of the qubit, hence its effective Larmor precession frequency, which in turn causes the qubit to accumulate a random phase. If the noise is short correlated in time (e.g. white noise) and weak, the dephasing rate can be calculated with the *Bloch-Redfield* approach [87]

$$\Gamma_2 = \frac{1}{2}\Gamma_1 + \Gamma_\phi, \quad (4.7)$$

where $\Gamma_1 = 1/T_1$ is the energy relaxation rate, $\Gamma_2 = 1/T_2$ the dephasing rate and Γ_ϕ the pure dephasing rate. In an experiment one can only measure the combination of pure dephasing and energy relaxation of a qubit state which is T_2 .

Figure 4.13 shows how an interference measurement, which is phase sensitive and shows the dephasing time, can be implemented. Starting with the qubit in its ground state two $\pi/2$ -pulses are applied. They are phase coherent and were defined to be x-pulses. The pulses are detuned from the transition frequency by $\delta/(2\pi) = \nu_a - \nu_d = 7.6$ MHz. The first pulse flips the qubit into the superposition state $1/\sqrt{2} (|g\rangle + |e\rangle)$. During a time Δt the qubit state evolves freely, in the rotating frame set by choosing ω_d it precesses with δ and a phase $\phi = \delta\Delta t$ is acquired. The second pulse rotates the state vector such that one of the components of the acquired phase (in our case the y-component) is mapped to the z-component of the state after rotation. The projection of the z-component, which is the only parameter that we can measure in the experiment, is measured after the end of the second pulse. The measurement is pulsed in order not to induce additional decoherence through intra-cavity photons [83, 73]. The measurement pulse is a 40 μs long rectangular pulse which starts 20 ns after the last qubit manipulation.

The pulse sequence as described above was implemented for an increasing free evolution time

relaxation times of up to $T_1 = 14 \mu\text{s}$ could be observed, though not reliably.

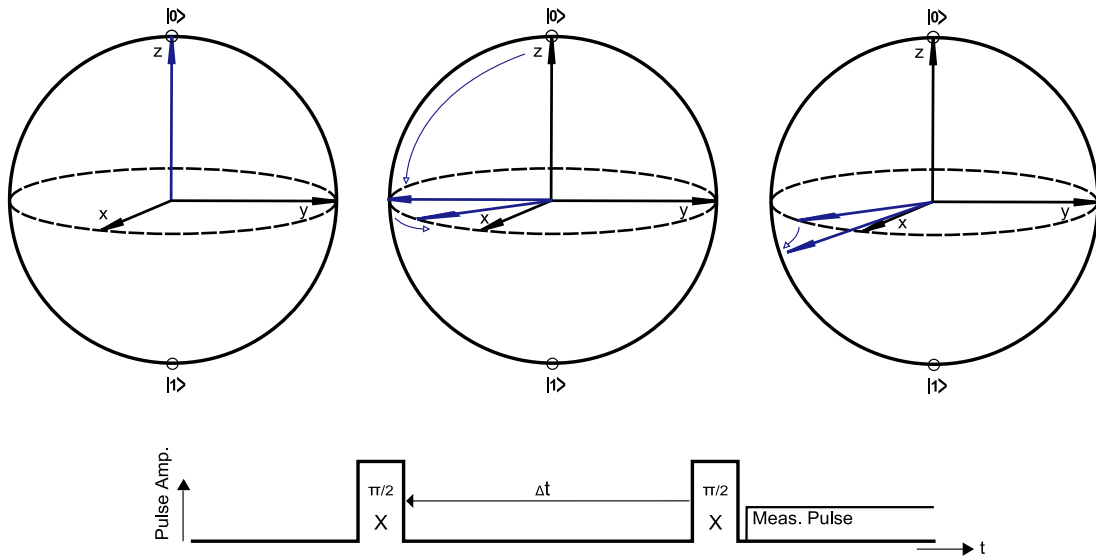


Fig. 4.13: Implemented Ramsey pulse sequence (bottom) and corresponding schematic representation of pulse sequence in terms of rotations on the Bloch sphere (top).

$0 < \Delta t < 1.4 \mu\text{s}$ with a step size of 8 ns. This was done sequentially where every single sweep was averaged 2^{16} times (similar to the Rabi experiment) before starting with the next one. The sampling period of the measurement beam was again one nanosecond in each quadrature. The amplitude of the spectroscopy drive was tuned to yield a π -pulse with a length of 10 ns, which was 5.75 dBm at $\nu_s = 3.696$ GHz in a separate experiment. A $\pi/2$ pulse was realized in the experiment at the same frequency and taken to be 5 ns long. The result of this measurement is shown in Fig. 4.14a-b, where the population was determined by comparing every single trace to a theoretically predicted response to a simple π pulse such as in the previous section.

Figure 4.14b shows the extracted qubit excited state population with respect to the free evolution time Δt . We observe Ramsey fringes with a frequency $\delta/(2\pi) = (\omega_a - \omega_d)/(2\pi) = 7.6$ MHz. The measurement was pulsed and weak, $\langle n \rangle < 1$, and the exponential decay of the 2π sequence, $\Delta t = 120$ ns, was determined to be $T_1 = 14 \mu\text{s}$. The decay of the Ramsey fringes indicate the loss of phase coherence versus free evolution time Δt . Fitting with an exponential decay law, the dephasing time was determined to be $T_2 = 740$ ns. The measured dephasing and energy relaxation times in this experiment are among the longest ever observed in solid state quantum bits; compare to measurements of other groups e.g. [86] with $T_2 = 0.3 \mu\text{s}$ and $T_1 = 0.5 - 1 \mu\text{s}$, [53] with $T_2 = 200$ ns and $T_1 = 4 \mu\text{s}$, or more recent results [19] with $T_2 = 0.8 \mu\text{s}$ and $T_1 = 1 \mu\text{s}$. The measured qubit lifetimes are also slightly improved in comparison to [46] where $T_2 > 0.5 \mu\text{s}$ and $T_1 = 7.3 \mu\text{s}$ was reported although the identical sample was used. This could indicate a lower base temperature, less vibrations, or lower external noise obtained in the presented measurement setup; probably more likely are improved sample parameters in terms of the dephasing rates due to additional oxidation in the tunnel barriers of the sample during the past two years.

4 Circuit QED Experiments

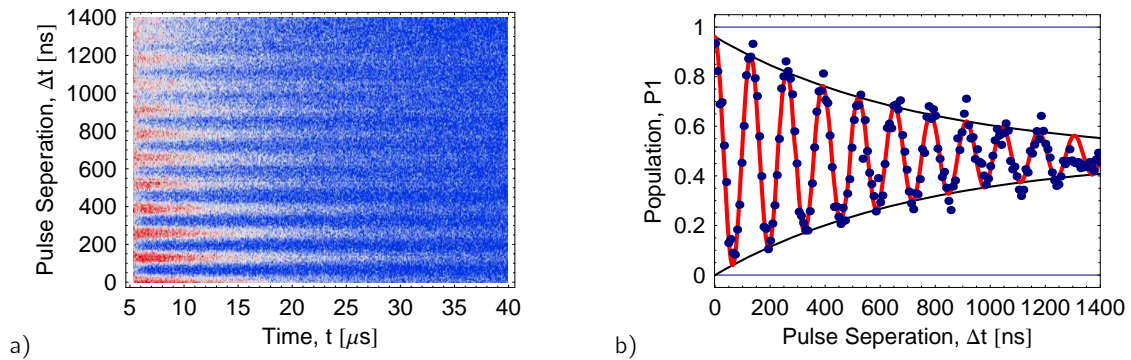


Fig. 4.14: a) Measured resonator response ϕ for the pulse sequence shown in Fig. 4.13 for different free evolution times Δt (blue to red: 0 to 40 degrees phase shift of the probe beam). b) Extracted qubit population (similar procedure as for the Rabi oscillations) versus Δt .

4.3.3 Spin Echo Technique

In this section the influence of spin echo techniques on the coherent qubit state lifetime are investigated. This work was carried out together with a semester student, L. Steffen [88]. Originally the spin echo technique was developed in NMR systems, where it is used to cancel an inhomogeneous broadening of the spin resonance lines, e.g. due to spatial inhomogeneities of the magnetic field. In this experiment however, spin echoes are used to cancel low frequency temporal variations in the phase of a single qubit superposition state that gets measured repetitively. Basically it is possible to cancel frequency components of noise occurring on timescales that are in the order of, or longer than the free precession time between two subsequent spin echo pulses. We expect such a contribution from low frequency charge noise ($1/f$) which affects the transition frequency of the qubit. For example during the free precession in a Ramsey sequence a random phase is accumulated in such a way. Implementing the spin echo technique leads to a larger dephasing time than the T_2 inferred from Ramsey fringes because it reduces the effect of low frequency phase noise on the qubit state. It also can provide information about the spectrum of the noise acting on the qubit.

We slightly modify the Ramsey sequence presented before by introducing an additional π pulse that is positioned symmetrically between the two $\pi/2$ pulses, see Fig. 4.15. Assuming that the noise acting on the qubit's transition frequency is not perfectly white, calculations and experiments show that the spin echo method can increase the T_2 time significantly [86, 89, 90]. In fact the additional π pulse, which rotates the qubit state by 180 degrees about an axis orthogonal to the quantization and Ramsey rotation axes, is inserted to make the phases accumulated during the free evolution intervals before and after the pulse canceling each other. When the two time intervals are chosen symmetrically the total phase accumulated is independent of the detuning $\delta = \omega_a - \omega_s$ if δ is constant over the one complete sequence. Compared to the Ramsey experiment the spin echo signal is therefore less sensitive to fluctuations of δ from sequence to sequence [89]. The additional symmetrically placed π -pulse can be chosen to induce a π -rotation either around the x axis or the y axis. In the first case ideally the qubit is expected to be rotated always to the ground state, in the latter case the qubit will always

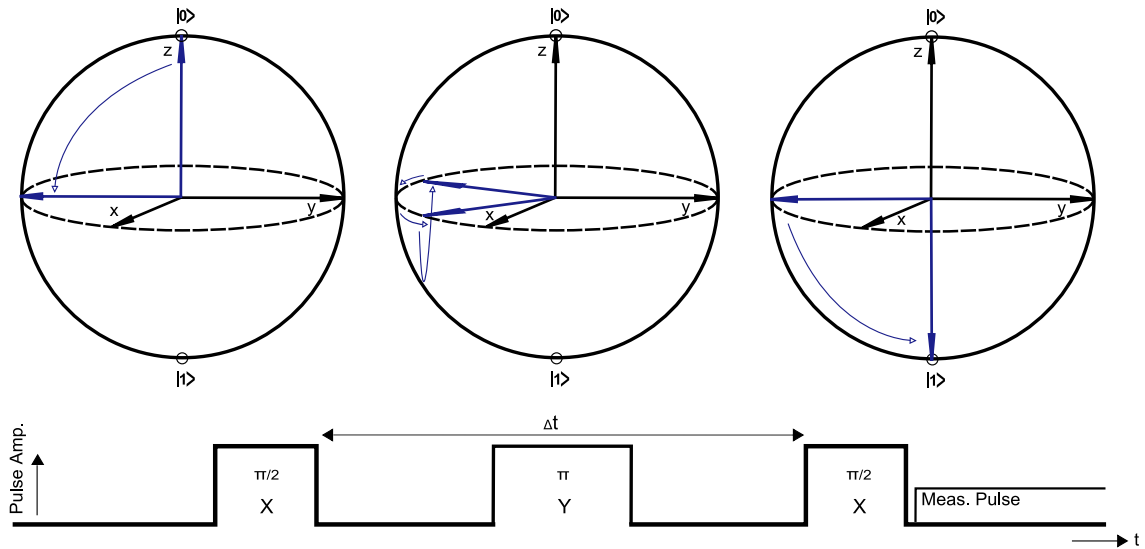


Fig. 4.15: Implemented spin echo pulse sequence (bottom) and corresponding schematic representation in the Bloch sphere picture (top). Initially the qubit is in its ground state. The first $\pi/2$ -pulse (5 ns) is in phase with the last one, both around x. The π pulse (10 ns) is applied symmetrically between the two other and chosen to be 90 deg out of phase, around y, but still phase coherent.

end up in the excited state. Implementing the pattern shown in Fig. 4.15 for different Δt one can therefore directly observe how phase coherence gets lost, see Fig. 4.16a.

All pulses shown in Fig. 4.15 are taken to be near resonant, $\delta = \omega_a - \omega_d \sim 0$. The first pulse brings the qubit into a superposition state. During free evolution $\sim \Delta t/2$ the Bloch vector precesses with δ and a random phase due to noise gets acquired. The second pulse rotates the qubit around the x axis by 180 degrees. During the second free evolution period the vector therefore precesses in the opposite direction. The last pulse maps the y-component of the acquired phase to the z-component of the state vector which is being measured after the end of the last pulse.

Measuring the measurement beam phase shift 20 ns after the last qubit manipulation as a function of time shows the decay due to energy relaxation of the qubit with $T_1 \approx 7 \mu\text{s}$ obtained in a pulsed measurement with a mean intra-cavity photon number of $\langle n \rangle \approx 6.5$ photons. The measurement response for $\Delta t = 32$ ns and the corresponding theoretical calculation are shown in Fig. 4.16b. The solid curve is obtained by a cavity Bloch simulation. This time by simulating the full pulse sequence of the sweep with $\Delta t = 32$ ns. Note, this is the reason for a theoretically expected population of 1/2 at 7 μs just before the second Ramsey pulse is applied. Because the measurement was pulsed the amplitudes are low in the beginning, at 7 μs , and the phase of the signal is thus undefined, see Eq. (3.5), which is the reason why the data is analyzed starting at 7.4 μs . Using the theoretical response for the determination of the actual population of the excited state, such as in section 4.3.1, and plotting the extracted data points with respect to Δt , we obtain the decaying signal shown by the solid line in Fig. 4.16a. An exponential fit to the data gives a dephasing time of $T_2 = 1.9 \mu\text{s}$. The signal levels off at $P_{\text{mixed}} = 0.37$ somewhat below the theoretically expected population of 1/2, which is in agreement with a

4 Circuit QED Experiments

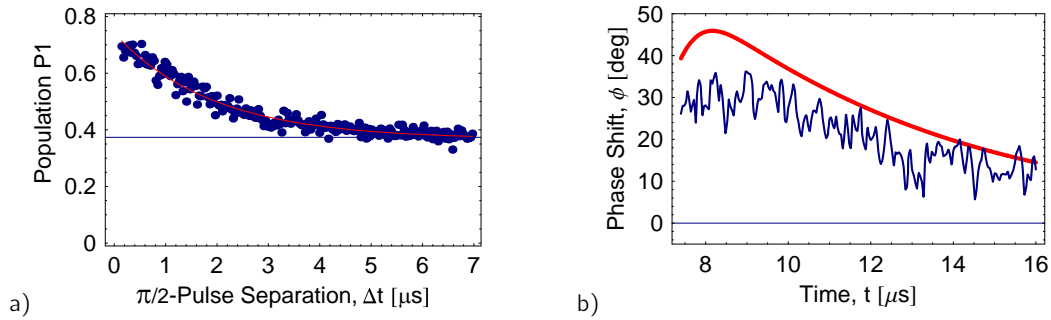


Fig. 4.16: a) Extracted excited state population versus pulse separation time Δt and exponential fit. b) Measured probe beam phase shift response for the spin echo sequence with a pulsed measurement for $\Delta t = 32\text{ns}$. The solid line is obtained from a cavity Bloch simulation where the response to the full sequence was calculated.

visibility of $\approx 75\%$ obtained in this measurement. The reduced visibility in comparison to previous presented data is most likely due to the pulsed measurement and the comparatively high measurement powers of $\langle n \rangle = 6.5$ intra-cavity photons. It constitutes an important task for the future to understand the implications of the resonator being populated with high mean measurement photon numbers in a pulsed measurement.

Spin echo experiments with more than one π pulse were investigated in order to learn more about the noise spectrum that affects the qubit. One can expect to cancel the influence of noise at higher frequencies with the free evolution time between the pulses being shorter. If two π -pulses are applied one has the choice of two different versions. For equally spaced spin echo pulses a Ramsey pattern with a third of the detuning frequency is obtained. It is also possible to rotate the qubit to the excited state at the end of every sequence at all times, like in the presented case, if the spacing of the pulses is chosen appropriately – the two π -pulses have to be separated by twice the time between a $\pi/2$ and a π pulse. Unsurprisingly the latter option turned out to be more efficient as the entire (random) phase is canceled for the whole sequence, which is obviously not the case for equally spaced pulses (therefore the expected Ramsey fringes). The decoherence time obtained for two spin echo π pulses was determined to be $T_2 = 2.1\ \mu\text{s}$ (for the Ramsey type it was only $1.5\ \mu\text{s}$). With more than two spin echo pulses we did not show any improvement. Also, additional unwanted features in the obtained decay response were observed. They could be explained with a Bloch simulation showing that they are due to the finite pulse length of possibly just slightly off-resonant pulses. This effect becomes more pronounced when applying more pulses during the same time of free evolution Δt .

Conclusions

The observation of an increased spin echo dephasing time $T_2 \approx 1.9 - 2.1\ \mu\text{s}$ by a substantial factor of up to ~ 3 leads to the conclusion that low frequency $1/f$ type noise is one of the main decoherence mechanisms in our setup. This result is therefore in accordance with our assumption of the observed decoherence times being limited by low frequency charge noise.

We also conclude that introducing two spin echo pulses, hence improving the efficiency of canceling higher frequency noise, has a positive effect. The improvement is not that significant however and it is lost quickly for even more pulses because of the finite pulse length at a finite detuning δ and not perfectly tuned π pulses; these effects add up for more spin echo pulses applied. The observed energy relaxation time $T_1 \approx 7 \mu\text{s}$ is limited by high frequency noise and we expect noise-sources at higher frequencies to play a role also for the dephasing time as the upper limit in the framework of the Bloch-Redfield theory, see Eq. (4.7), is given by $T_2 = 2T_1$, which would be $\sim 14 \mu\text{s}$ for the presented experiment. The results compare well with spin echo decoherence times measured by other groups in superconducting qubits. The presently largest spin echo decay time however was reported to be $4 \mu\text{s}$, realized in a superconducting phase qubit [53].

4.3.4 Tomography of Quantum States

The realization of the tomography of arbitrary quantum states presented in this section, is the result of work that has been done together with a semester student, P. Maurer [91].

In order to obtain the full information of an arbitrary qubit state, which is given by the position the Bloch-vector is pointing to and its length, the different components σ_x , σ_y and σ_z have to be mapped to the σ_z component as σ_z projection is the only component we are able to measure in the implemented experiment. We have already seen how one can realize phase sensitive measurements of a qubit state in terms of Ramsey experiments. A quite similar procedure will be implemented in order to demonstrate quantum state tomography [13, 92, 93]. Generally three independent measurements of an equally prepared state are sufficient. First the state has to be prepared and the σ_z -component can be measured directly. In the second and third measurement the equally prepared state is rotated by $\pi/2$ around the x or y -axis respectively. Measuring after these two tomography pulses yields the σ_y and σ_x components of the prepared state.

Although just three well chosen tomography measurements would give the desired qubit state information in principle, in the measurements presented all possible combinations of tomography pulses are applied and the resulting state is measured, see Fig. 4.17. Such a measurement procedure yields a two dimensional probability map for the measurement of the excited state, see Fig. 4.18. The direction and length of the Bloch vector corresponding to the prepared state can simply be computed from this pattern, where the length is determined by the maximal contrast that was measured. Such a measurement scheme is not very practical for a fast

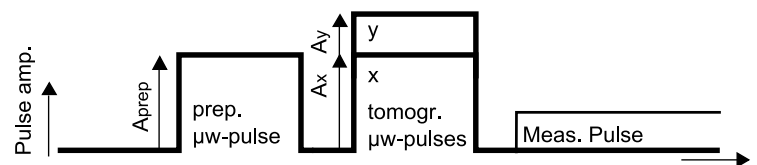


Fig. 4.17: Pulse sequence for quantum state tomography.

quantum state tomography, but it is a nice demonstration of the qubit state control one has reached and provides a good calibration for arbitrary σ_x and σ_y rotations. In order to be able to realize the tomography pulses with good resolution in the presented experiments the pulse amplitude is varied, rather than the pulse length. This is equivalent as the induced rotation angle in radian is e.g. $\varphi_x = \Omega_x t$, where the rate Ω_x is proportional to the amplitude of a pulse and t is the length of the applied pulse. Starting from no pulse at all the x-pulse amplitude A_x is ramped up linearly followed by the same sequence with a low amplitude y-pulse amplitude A_y superposed at the same time, see Fig. 4.17. This is repeated with a slightly larger y-pulse amplitude and so on. Every quantum state shows a distinct pattern in such a measurement, see Fig. 4.18.

In this measurement we have used negative and positive voltages as input to the IQ mixer, in order to access all 4 quadrants of the complex plane, which induce positive and negative rotation angles respectively. To get the output amplitude right, a calibration of the partly non-linear mixer behavior was implemented. The preparation pulse length as well as the lengths of the tomography pulses was chosen to be 10 ns. Right after the preparation pulse the two tomography pulses were applied exactly at the same time. Those were followed by a weak measurement pulse with $\langle n \rangle = 5$ intra-cavity photons. The amplitude of a π -pulse was obtained in a separate experiment, a $\pi/2$ -pulse was then implemented with a half of this amplitude. For such a measurement sequence we expect a circular measurement pattern, see Fig. 4.18. Every trace in x direction swept the amplitude of the tomography pulse around σ_x and constituted an independent measurement which required an acquisition time of some minutes. This was repeated for different tomography pulse amplitudes inducing rotations around σ_y , which were applied simultaneously to the x-pulses. These results got appended in the y direction of the plots shown in Fig. 4.18. The applied drive amplitudes on the IQ mixer as well as the acquired rotation angles (fitted for $|e\rangle$ measurement, Fig. 4.18a) are indicated. Note, that one expects a checkerboard type of pattern, rather than a circular pattern, for tomography pulses that are applied subsequently [91].

Discussion

Looking at the overall patterns in Fig. 4.18 and comparing them with the simulations shows that the implemented quantum state tomography works and a good control of the quantum state has been achieved. Nevertheless, there are various issues which make the obtained measurements look noisy compared to results presented in [93, 92, 5]. Firstly the IQ mixer output was determined to be not linear with respect to the input voltages for the range it had to be used in the current experiment. To correct for that, a calibration of the output amplitude for the two channels was introduced. The phase however was not calibrated and is expected to go along with the non linearity of the amplitude. Also the fact that we are not able to completely shut down one of the quadratures with the other one being on could possibly have a bad impact on the results, since we still induce transitions with the voltage quadrature that should nominally be off, see also section 3.2.1. More importantly, the acquisition of one trace in the x direction required a measurement time of some minutes, that results in an acquisition

time for one whole pattern of well above an hour. During this time the qubit was subject to charge noise, which had the effect that the gate charge bias was not exactly the same from one measurement to following one. This is the main reason for the x traces being recognizable individually in the presented patterns. Better equipment to create phase sensitive pulses or an even better characterized mixer, as well as a qubit design that allows for longer acquisition times at the same transition frequency (e.g. with a bigger E_{j0}/E_{c0}) or even a more careful measurement, e.g. with less measurement power, less data points and shorter averaging and acquisition times, will be sufficient to improve the presented patterns significantly. Qualitatively however the full quantum state tomography is demonstrated successfully.

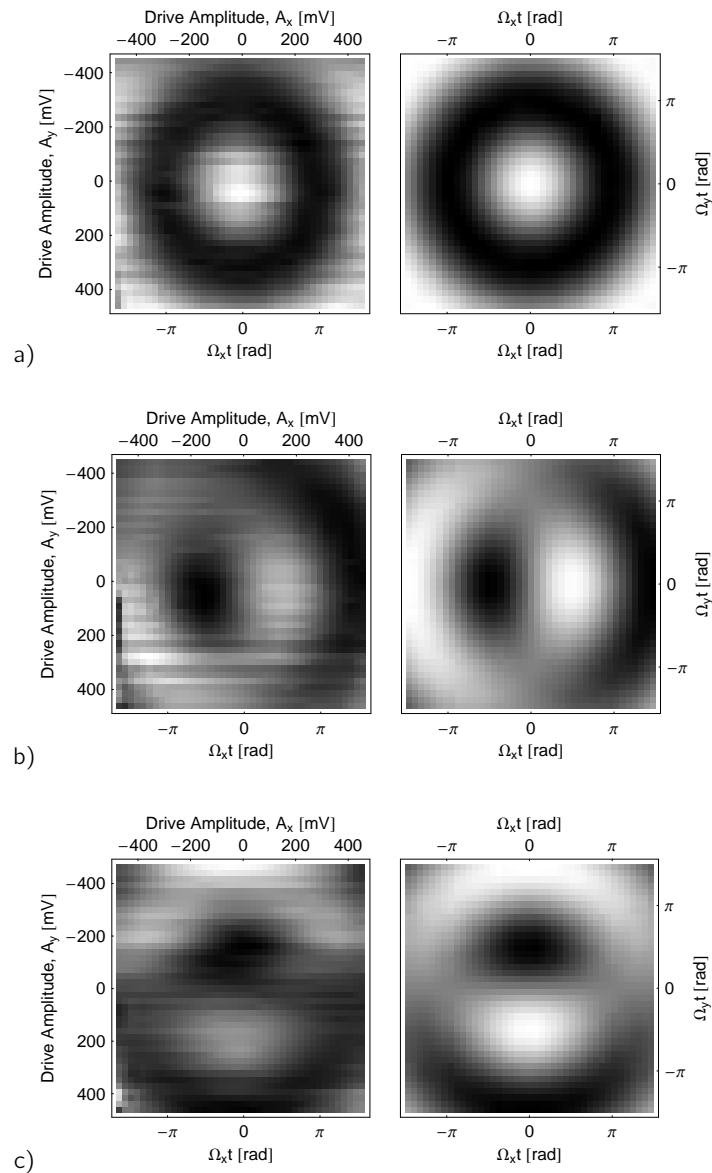


Fig. 4.18: Measured probe beam phase shift response of three differently prepared quantum states a) $|e\rangle$, b) $1/\sqrt{2}(|g\rangle + |e\rangle)$ and c) $1/\sqrt{2}(|g\rangle - |e\rangle)$ as a function of the applied tomography pulses (left) and corresponding simulation (right).

In this section arbitrary rotations on either the x or the y-axis of the qubit state in the Bloch sphere picture were demonstrated. For the realization of rotations around the z-axis, corresponding to a single qubit phase gate, there are several possibilities [6], including e.g. a pulsed AC-Stark shifting of the qubit transition frequency or a pulsed change of the qubit bias parameters inducing a shift in the qubit transition frequency. The implementation presented in section 4.4 however uses adiabatic changes of the qubit Hamiltonian generating a σ_z -rotation that arises due to geometric properties of the parameter space of the qubit Hamiltonian only – the Berry phase.

4.4 Berry Phase Experiment

The experiments presented in this section have been carried out together with my colleague Peter Leek, post doctoral associate in the Quantum Device Lab. One reason to investigate the Berry phase [94, 95, 96], a geometric phase arising in quantum systems, is that it is argued to be useful as a phase gate for quantum information processing. In particular geometrically acquired phases are argued to be more robust to errors than the regular dynamic phase [8, 9]. Its relevance for quantum computation has been demonstrated both in NMR [97] as well as in ion trap systems [98]. Yet another reason to look into the Berry phase is the fact that it is fundamentally interesting to observe a geometrically acquired phase in the wave-function of an artificially generated macroscopic solid state quantum system. Recently there has been significant interest in observing controlled geometric phases in solid state qubits, in particular there are a number of proposals with superconducting circuits [99, 100, 101, 102]. The long coherence times and the deterministic qubit state control, demonstrated in previous chapters of this thesis, constituted the prerequisites for the experiment presented in the following – the first observation of the geometric phase in a solid state quantum bit.

4.4.1 The Geometric Phase

If one considers a system with a Hamiltonian depending on a parameter that is varied cyclically, the wave-function of the system acquires a phase in addition to the dynamic phase that is geometric in nature. If the changes on the Hamiltonian are done in an adiabatic⁵ manner this phase is called *Berry phase* after Sir M. V. Berry who first investigated this phenomenon in 1984 [94]. Geometric phases actually appeared much earlier in literature. The first time a geometric phase definition appeared was in 1956 by Pancharatnam who investigated the interference of polarized light [103]. The Pancharatnam phase can be seen as a generalization of Berry's phase for non-closed loops in the quantum systems parameter space. Note, a generalization for non adiabatic but cyclic evolutions was developed by Aharonov and Anandan [104].

⁵In contrary to thermodynamics where the term adiabatic refers to processes without heat exchange, which can in practice easiest be realized by carrying out processes *quickly*, in quantum mechanics it refers to a *slow* evolution of the system compared to its intrinsic timescale – a quasi-static process in thermodynamical terms.

An intuitive analogy provides the classical mechanics counterpart of Berry's Phase, i.e. the *Hannay angle* [105], appearing e.g. when thinking about parallel transporting a vector on a curved surface, see Fig. 4.19. The definition for being parallel on such a 2-sphere is being parallel to a meridian, however this definition does not work on the entire surface – at least at one point on the sphere you get in trouble with this definition, i.e. the poles of the sphere. Also the rotation of Foucault's pendulum can be explained by this phenomenon which is mathematically called *holonomy*. The Berry phase which was derived for quantum systems can therefore be identified with a Hannay angle in the classical limit. One can interpret its occurrence as a geometrical property of the underlying parameter space of the system's Hamiltonian and describe it within the framework of differential geometry as a *holonomy* of the parallel transported eigenstates of the quantum mechanical system.

The Berry phase can be seen as a 'memory' of global changes of a system without the occurrence of a local change. In quantum mechanical terms, a slowly evolving quantum system retains a memory of its motion when returned to its original physical state $\psi' = e^{i\gamma}\psi$. Interestingly it turns out that this phase $\gamma(C)$ depends solely on the contour C that is traced out in parameter space but not on the way the contour is traversed nor on the time it takes as long as it is adiabatic. Note, if the parameter space is a simply connected manifold and the eigenvectors of the considered system can be chosen everywhere real in a smooth way the Berry phase $\gamma(C)$ is zero [106]. Therefore typically the appearance of a geometric phase indicates that the system's parameter space is undefined for some combination of parameters, or that the eigenvectors of the Hamiltonian describing the system are complex valued, which is the case in our experiment as we will see. More important to note is the fact that it is not possible to remove the geometric phase by a certain choice of the basis states of the Hamiltonian, i.e. a gauge transformation. Therefore it is possible to measure it in an interference experiment.

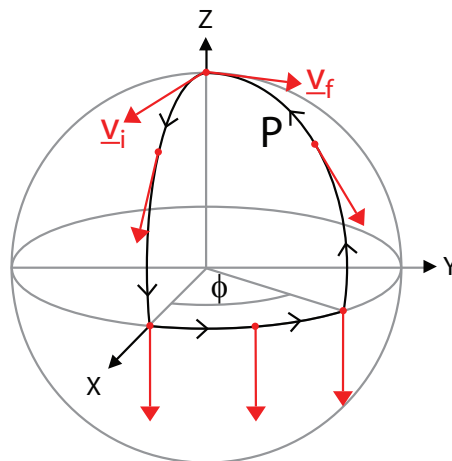


Fig. 4.19: Classical analogy to the Berry phase – the Hannay angle. The vector \vec{v}_i is parallel transported on a spherical surface along the path P until it reaches its final position \vec{v}_f . Due to the curvature of the 2-sphere the vector \vec{v}_f is rotated with respect to \vec{v}_i by an angle ϕ . In the experiments presented, the vector \vec{v} is the state vector of a pseudo spin- $\frac{1}{2}$, the Cooper pair box, which follows the rotation of an externally applied fictitious magnetic field whose parameter space is a 2-sphere.

4.4.2 Pseudo Spin-1/2 under RF-Irradiation

We consider the dynamics of a pseudo spin- $\frac{1}{2}$ particle, the Copper pair box, in an adiabatically rotating fictitious magnetic field, which is realized with a phase sensitively induced rf-irradiation, see Fig. 4.20a. The interaction Hamiltonian of a spin- $\frac{1}{2}$ particle in a magnetic field that is rotating adiabatically around the z-axis, is given by

$$H(t) = \mu \vec{B}(t) \cdot \vec{\sigma}, \quad \text{with} \quad \vec{B}(t) = B_0 \begin{pmatrix} \sin \Theta(t) \cos \phi(t) \\ \sin \Theta(t) \sin \phi(t) \\ \cos \Theta(t) \end{pmatrix}, \quad (4.8)$$

where $\phi(t) = \omega t$ with ω the angular frequency of rotation of the magnetic field, $\mu = \hbar e / (2m)$ the magnetic moment, $B_0 = |\vec{B}(t)|$ and Θ the angle between the rotating B-field vector and z-axis.

For our particular case, where the effective B-field is generated by applying phase sensitive microwave frequency signals, the parameter space is shown in Fig. 4.20b. We can write the Hamiltonian, which is valid at the sweet spot of the CPB, given Eq. (4.6)

$$H(t) = \frac{\hbar}{2} \vec{B}_{\text{eff}}(t) \cdot \vec{\sigma} \quad (4.9)$$

$$= \frac{\hbar}{2} [\Omega_x \sigma_x + \Omega_y \sigma_y + \Delta \sigma_z] \quad (4.10)$$

$$= \frac{\hbar}{2} [\Omega_R \cos(\phi) \sigma_x + \Omega_R \sin(\phi) \sigma_y + \Delta \sigma_z] \quad (4.11)$$

$$= \frac{\hbar}{2} \begin{pmatrix} \Delta & e^{-i\phi} \Omega_R \\ e^{i\phi} \Omega_R & -\Delta \end{pmatrix}, \quad \text{with} \quad B_{\text{eff}}(t) = \begin{pmatrix} \Omega_R \cos \phi \\ \Omega_R \sin \phi \\ \Delta \end{pmatrix} \quad (4.12)$$

with $\Theta = \arccos(\Delta / \sqrt{\Delta^2 + \Omega_R^2})$ the cone angle of the induced rotation in parameter space, see Fig. 4.20b, $\Omega_R = \sin \Theta$ the externally applied angular Rabi frequency, $\Delta = \cos \Theta = \omega_a - \omega_d$ the detuning between drive frequency and Larmor frequency and $\phi = t\Delta$ the angle of rotation. The normalized eigenstates of $H(t)$ solving the eigenvalue equation $H(t)|n(t)\rangle = E_n|n(t)\rangle$ are then

$$|n_+(t)\rangle = \begin{pmatrix} \cos \frac{\Theta}{2} \\ e^{i\phi} \sin \frac{\Theta}{2} \end{pmatrix} \quad \text{and} \quad |n_-(t)\rangle = \begin{pmatrix} -\sin \frac{\Theta}{2} \\ e^{i\phi} \cos \frac{\Theta}{2} \end{pmatrix}, \quad (4.13)$$

with the corresponding energy eigenvalues $E_{\pm} = \pm \hbar/2 |\vec{B}_{\text{eff}}| = \pm \hbar/2 \sqrt{\Delta^2 + \Omega_R^2}$. The parameter space of the effective B-field $\vec{B}_{\text{eff}}(t)$ is a 2-sphere, where we have three control parameters that can be time dependent $\Delta(t)$, $\Omega_R(t)$ and $\phi(t)$.

Implemented Path

A possible closed path that can be implemented using these parameters is shown in Fig. 4.20b. Such a contour is convenient to implement since the drive frequency ω_d is taken to be constant.

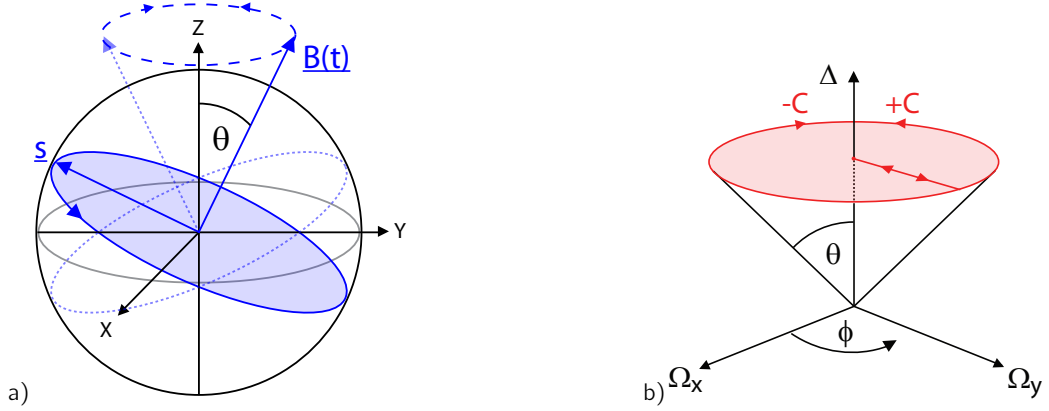


Fig. 4.20: a) Bloch sphere of a spin- $\frac{1}{2}$ particle in the superposition state \vec{s} . The state vector rotates with the Larmor frequency ω_a around the quantization axis set by the direction of the effective B-field. $\vec{B}(t)$ is rotated around the z axis adiabatically so the spin can follow its evolution quasi-statically. b) Parameter space of the pseudo spin- $\frac{1}{2}$ particle under the influence of external rf-irradiation. $\pm C$ shows two directions of the path of the effective B-field vector $\vec{B}_{\text{eff}}(t) = (\Omega_x(t), \Omega_y(t), \Delta(t))$ that have been implemented in the experiments presented.

The field initially along z gets adiabatically tilted to an angle Θ by ramping up the drive power Ω_y adiabatically. It is then adiabatically rotated in the $\Omega_x - \Omega_y$ plane to form a closed loop, either $+C$ or $-C$. The geometric phase $\gamma(C)$ associated with this particular evolution is simply plus or minus half the solid angle $\Gamma(C)$ enclosed by the effective B-field vector along C

$$\gamma(C) = \pm \frac{1}{2} \Gamma(C) = \pm \frac{1}{2} \phi (1 - \cos \Theta), \quad (4.14)$$

which is $\gamma(C) = \pm \pi (1 - \cos \Theta)$ for one closed loop [94]. While the dynamically acquired phase depends on the period of the cyclic motion (it is a function of time), we see that the geometric phase depends solely on the opening angle Θ of the contour in the presented case. In order to carry out experiments where we measure the Berry phase as a function of a bias parameter, in the measurements presented below we choose a finite detuning Δ as well as a fixed angle of implemented rotation ϕ and measure the acquired phase as a function of the externally applied drive $\Omega_R(t)$.

Adiabatic Criterion

A necessary criterion for the observation of the Berry phase is an *adiabatic* change of the Hamiltonian in time. The adiabatic theorem, first mentioned by Ehrenfest [107], can be formulated as follows: For a slowly varying Hamiltonian, the instantaneous eigenstates of the Hamiltonian evolve continuously into the corresponding eigenstate at a later time, e.g. the n -th energy eigenstate stays in the n -th eigenstate during an evolution of the system: $|\psi(0)\rangle = |n(0)\rangle \rightarrow |\psi(t)\rangle = |n(t)\rangle$. In our particular case this necessary precondition can be understood quite descriptive; it is required that the spin of the qubit is able to follow the rotation of the effective B-field, see Fig. 4.20a. In other words, the evolution of the system has to be slow in

comparison to its intrinsic timescale, i.e.

$$\frac{\omega_0}{\omega_i} \rightarrow 0, \quad (4.15)$$

where $\omega_0 = \langle n_+ | \partial_t | n_- \rangle$ denotes the angular frequency of the evolution, and $\omega_i = (E_+ - E_-)/\hbar = \sqrt{\Delta^2 + \Omega_R^2}$ the intrinsic frequency of the system which is given by the energy gap between the two eigenstates. For the first part of the path realized, see Fig. 4.20b, where $\phi(t)$ is constant we therefore require, given Eq. (4.15) and Eq. (4.13),

$$\frac{\Theta'(t)}{2\sqrt{\Delta^2 + \Omega_R(t)^2}} \ll 1, \quad (4.16)$$

and for the circular part of the path shown in Fig. 4.20b we require, given Eq. (4.13),

$$\frac{\sin \Theta \phi'(t)}{2\sqrt{\Delta^2 + \Omega_R^2}} \ll 1 \quad (4.17)$$

for the adiabatic criterion to be fulfilled in the experiment. Using these formulas one can find optimal shapes for ramping up the drive power Ω_R and an optimal timing in order to keep the adiabaticity constant over a full path. Typical values of the adiabatic parameter, the ratios Eq. (4.16) and Eq. (4.16), are in the order of 0.1 in the experiments presented.

4.4.3 Measurement & Results

In our measurement setup the Berry phase is distinguished from the regular dynamic phase by means of the developed spin-echo technique. A spin echo sequence similar to the one investigated in section 4.3.3 is used to entirely cancel the dynamic phase, see Fig. 4.21 and Fig. 4.22. In order to monitor the state evolution, a quantum state tomography procedure is employed. Note, a quite similar implementation could already be realized successfully in an liquid state NMR system [97].

Measurement Procedure

The measurement setup is similar to the one shown in Fig. 3.3 with using two independent spectroscopy signal generators in order to be able to generate resonant pulses and detuned adiabatic drives. Both signals are modulated phase sensitively with the same IQ mixer. As the Berry phase is observed in an interference experiment we employ a Ramsey type of sequence. The first step is to apply a fast, 12 ns, and resonant, $\omega_a/2\pi = 3.712$ GHz, $\pi/2$ rotation around the y-axis as shown in Fig. 4.21. Both components of the thus generated superposition state $1/\sqrt{2}(|0\rangle + |1\rangle)$ are then subject to the adiabatic changes of the time dependent Hamiltonian. The changes are implemented by applying an off-resonant, $\Delta/2\pi = 25$ MHz Rabi drive. One of its quadratures is ramped up to Ω_R at constant adiabaticity, thus tilting the effective B-field the spin- $\frac{1}{2}$ sees by Θ . This signal is then kept at constant power, where one quadrature is

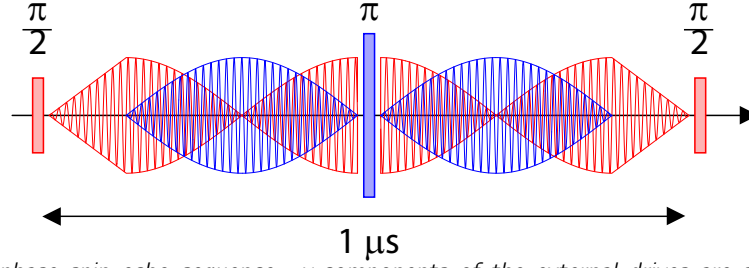


Fig. 4.21: *Berry phase spin echo sequence.* y -components of the external drives are shown in red and x -components in blue. A resonant Ramsey pulse ω_a is followed by detuned rf-induced adiabatic rotation of the effective B -field ω_d , a resonant spin echo pulse, another rotation of the effective B -field in opposite direction, a resonant tomography pulse and finally the measurement pulse at the resonator frequency ω_r (not shown). A typical sequence-length was $1 \mu\text{s}$ at a detuning $\Delta = 25 \text{ MHz}$ and a π -pulse length of 12 ns .

varied with the shape of a cosine and the other simultaneously with a sinusoidal shape, hence varying ϕ from ϕ_0 to $\phi_0 + 2\pi$ tracing the loop $+C$ or $-C$, see also Fig. 4.22 for examples of actual pulse-shapes applied to our upconversion IQ mixer.

The state after the first loop $+C$ can be written as $1/\sqrt{2}(|0\rangle + e^{i(\delta_1 - \delta_0 + \gamma)}|1\rangle)$ where $\delta_{0,1}$ is the dynamical component of the acquired phase. In order to get rid of the dynamical component, which is much larger than the geometric counterpart, we apply a spin echo π pulse on x , flipping the qubit state to $1/\sqrt{2}(|0\rangle + e^{-i(\delta_1 - \delta_0 + \gamma)}|1\rangle)$. For example in a period of 500 ns at a detuning of $\Delta/2\pi = 25 \text{ MHz}$ we acquire a dynamical phase of $12.5 \cdot 2\pi$ in comparison to a geometric phase $< 2\pi$ for one closed loop C . The second reason to employ the spin echo technique is an enhancement of the dephasing time of the qubit. Subsequent to the spin echo pulse the same off resonant rf-power is applied for exactly the same time and a shape symmetric with respect to the previous loop, see Fig. 4.22, tracing the path in the opposite direction $-C$. During this procedure the dynamical phase cancels completely with the exception of accumulated high frequency random phases due to dephasing. At the same time the acquired geometric phases add up, because the spin echo pulse flips the effective $B_x \rightarrow -B_x$ the spin- $\frac{1}{2}$ experiences and hence the effective direction of the trace $C \rightarrow -C$. We end up with twice acquiring the Berry phase where the final state can be written $1/\sqrt{2}(|0\rangle + e^{-i2\gamma}|1\rangle)$ with the sign of γ depending on the chosen order of $+C$ and $-C$.

In order to transform the obtained state to measurement probabilities we perform a fast, 12 ns , tomography pulse followed by a long measurement pulse at the resonator frequency ω_r . For the tomography pulse being a $\pi/2$ on x we obtain the y -component of the qubit states phase, for a $\pi/2$ on y we obtain the x -component and for not applying any tomography pulse the z component. The expected measurement values without taking the adiabatic criterion into account are then simply given by

$$\langle \sigma_x \rangle = 1/2(1 + \cos(2\gamma)), \quad \langle \sigma_y \rangle = 1/2(1 + \sin(2\gamma)), \quad \langle \sigma_z \rangle = 0, \quad (4.18)$$

where we took into account that the Bloch sphere was defined with radius 1, i.e. $\langle \sigma_z \rangle \in [-1, 1]$, while the population axis when measuring the excited state is only defined from 0 to 1 i.e. $\langle \sigma_z \rangle \in [0, 1]$. These expectation values were measured varying the off-resonant rf power

4 Circuit QED Experiments

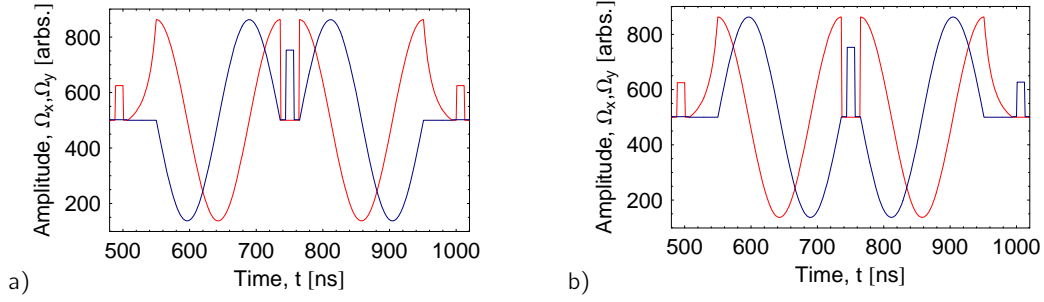


Fig. 4.22: Two examples of pulse-sequences applied to the IQ mixer. The maximally applied y component of the external drives $\Omega_{y_{max}}$ is shown in red and the maximally applied x component $\Omega_{x_{max}}$ in blue with a sequence length of $T = 500$ ns tracing two loops $\phi = 4\pi$ in parameter space. The plotted amplitude axis matches with the 10 bit resolution of the used arbitrary waveform generator and the time axis is plotted with respect to a master trigger. The sequence shown in a) traces $+C, -C$ and yields $\langle\sigma_x\rangle$ since the tomography pulse rotates around y . The sequence shown in b) traces $-C, +C$ and yields $\langle\sigma_y\rangle$ (tomography pulse on x).

$\Omega_R = \sqrt{\Omega_x^2 + \Omega_y^2}$, at detuning $\Delta/2\pi = 25$ MHz. The sequence time T , i.e. the time between the two $\pi/2$ -pulses, and the total angle of two subsequent loops $\phi = 4\pi$ are constant.

Results

In Fig. 4.23a-b two such measurements with different sequence times $T = 500$ ns and $T = 1000$ ns are shown, where $\langle\sigma_x\rangle$ is plotted in red, $\langle\sigma_y\rangle$ in blue and $\langle\sigma_z\rangle$ in black. The fact that we measure qualitatively similar patterns for acquisition periods different by a factor of 2 is a proof for the observed effect being purely due to the geometric phase. In addition to a reduced visibility because of dephasing, a decay of the signal is observed for increasing drive rates $\Omega_R/(2\pi)$, both features are discussed later. Figures 4.23c-d show results obtained with a Bloch vector simulation of the implemented pulse-sequences for comparison with the measurements 4.23a-b. The simulation did not take dephasing into account but it shows the expected influence of finite adiabaticity. The measured oscillations in the $\langle\sigma_z\rangle$ component of the qubit's state vector, see Fig. 4.23, compare well with the simulations. Furthermore, in the measurement with shorter sequence length we observe the amplitude of these oscillations to be larger than for the slower evolution, as expected. Both, the simulation and measurements show that the $\langle\sigma_x\rangle$ and $\langle\sigma_y\rangle$ components are only marginally affected by the influence of imperfect adiabaticity. We therefore conclude that the adiabatic theorem applies to our experiments.

If we consider no dephasing to occur and the adiabatic criterion to be fulfilled entirely for a start, given Eq. (4.14), the expected geometric phase can be calculated as

$$2\gamma(\Omega_R) = \pm\phi \left(1 - \frac{\Delta}{\sqrt{\Delta^2 + \Omega_R^2}} \right), \quad (4.19)$$

with the sign depending on the chosen loop direction. In order to extract the acquired Berry phase from the measurement data we use the measured $\langle\sigma_x\rangle$ and $\langle\sigma_y\rangle$ components of the

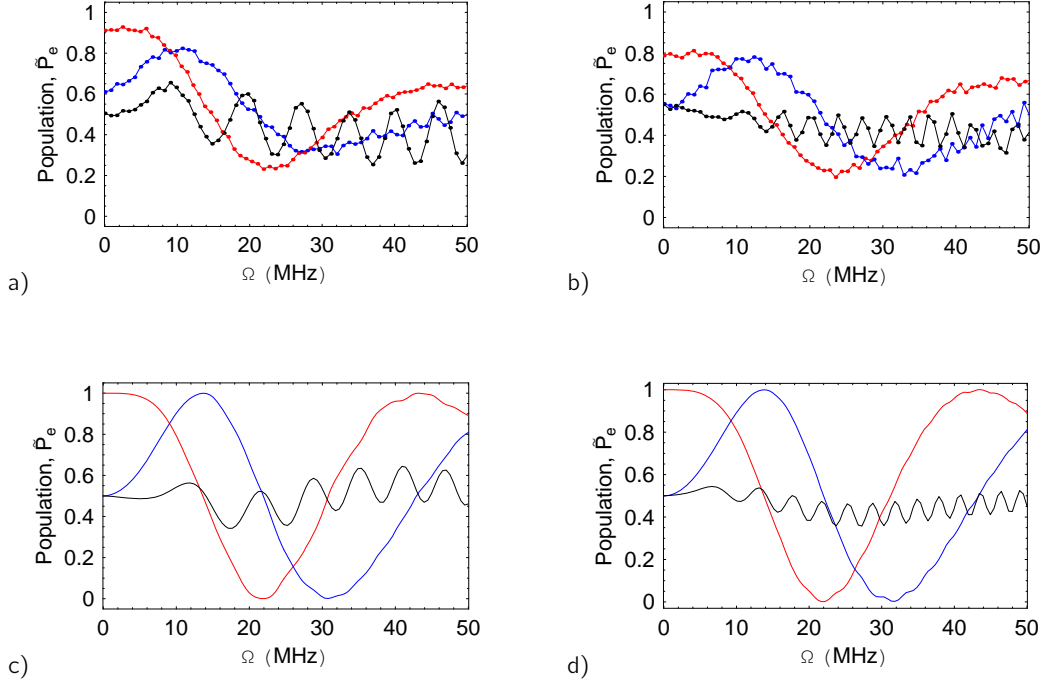


Fig. 4.23: Measured expectation values of σ_x (red), σ_y (blue) and σ_z (black) in dependence on the amplitude of the off-resonant drive $\Omega = \Omega_R/2\pi$. The corresponding Bloch vector simulations are shown below. Figure a) shows measurement results for $\Delta/2\pi = 25$ MHz, $\phi = 4\pi$ and a sequence time, i.e. the time between the two $\pi/2$ -pulses, of $T = 500$ ns. Figure b) shows the results for the same set of parameters except the sequence time which was chosen to be $T = 1000$ ns. The Bloch vector simulations c) and d) account for the motion of the effective B-field not being perfectly adiabatic but does not incorporate dephasing.

acquired data. Given Eq. (4.18) we can write down an equation for the acquired geometric phase

$$2\gamma(\Omega_R) = \tan^{-1} \frac{2\langle\sigma_y\rangle - 1}{2\langle\sigma_x\rangle - 1}. \quad (4.20)$$

Analyzing the measured expectation values, data points in Fig. 4.23, with Eq. (4.20), we can calculate the actual acquired geometric phase dependent on the chosen drive amplitude $\Omega_R/(2\pi)$, which is shown in Fig. 4.24. A positive Berry phase is acquired for the combination of paths $-C$ and $+C$, a negative phase for $+C$ and $-C$ and the geometric phase cancels for the combination of paths $+C$ and $+C$. The presented data was acquired at a detuning $\Delta/2\pi = 25$ MHz, with tracing two full loops $\phi = 4\pi$ and a sequence length of $1 \mu\text{s}$. Measurements of adiabatically acquired geometric phases of up to $\sim 2\pi$, depending on the external drive amplitude Ω_R , are demonstrated. The origin of the slight deviations between theory and measurement for the negative Berry phase in particular is still unclear, see Fig. 4.24. It is expected however that e.g. a measurement of $\langle\sigma_x\rangle$ and $\langle\sigma_y\rangle$ in an interleaved fashion, rather than measuring them subsequently for a entire set of different drive frequencies, would suppress systematic errors and further improve the shown results.

The acquisition of a purely geometric phase could be shown with good agreement to the theory

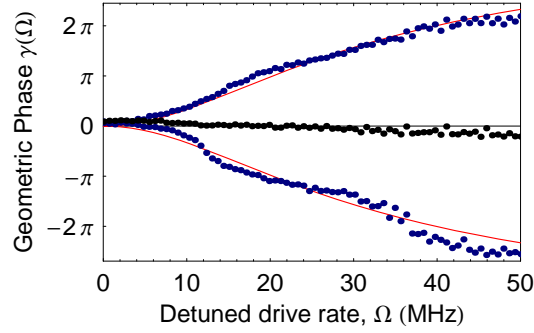


Fig. 4.24: Measured Berry phase versus external drive amplitude $\Omega = \Omega_R/(2\pi)$. Data points are extracted from the measurement shown in Fig. 4.23b as well as similar measurements with other path directions (not shown). Solid lines were obtained from theory Eq. (4.19), without considering decoherence or the adiabatic criterion and without any fit parameters.

of the Berry phase. We measured the geometric phase in a spin echo Ramsey experiment and observed the expected dependence on the solid angle enclosed by the contour traced in parameter space. The independence of the acquired phase on the implemented sequence times as well as the different signs of the acquired phase for different contour directions show the geometric origin of the measured phase unambiguously. However, there are important features of the measured data shown in Fig. 4.23 that need further discussion. First we observe a reduced visibility due to the expected dephasing during the Berry sequence which was relatively long. Furthermore, we observe the expectation values $\langle\sigma_x\rangle$, $\langle\sigma_y\rangle$ and $\langle\sigma_z\rangle$ to decay for an increasing drive amplitude, i.e. a path traversed at larger cone angles, an effect which we call geometric dephasing. These effects are discussed in more detail on the following pages.

Visibility

In order to determine the visibility in the results presented in this section, Fig. 4.23, a slightly different method was chosen compared to previously shown experiments. First, similar to earlier presented data, no pulse at all applied to the qubit in the ground state, but the measurement still pulsed, yielded the background signal which was defined as $\tilde{P} = 0$. Also similarly, a π -pulse was applied, which was tuned in a separate experiment, yielding the expected energy relaxation time $T_1 \approx 7 \mu s$. In order to determine the expected measurement response of the excited state however, no cavity Bloch simulation has been implemented for the Berry phase measurements. It was already pointed out that the temporal measurement response, the phase shift of the probe beam, is not as large as expected for the implementation of pulsed measurement schemes, see subsection 4.3.3. Either on the technical side, or in the model used for the cavity Bloch simulation (or the parameter values that are fed into the simulation) there are imperfections still to be investigated. However, in order to analyze the data independent of these issues we chose to determine the expected response by experimentally preparing and measuring the mixed state of the qubit and define it as $\tilde{P} = 0.5$. Such a procedure was chosen to account for the fact that the observed excited state population is always somewhat

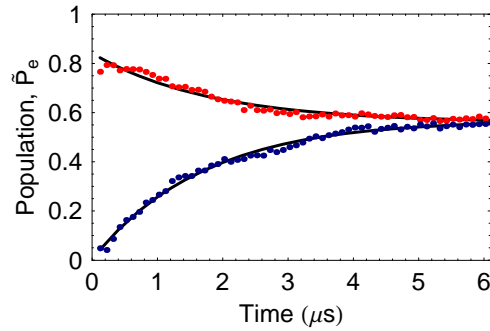


Fig. 4.25: Measured spin echo response with corresponding fit. Red data points show the response of a $(\pi/2)_x(\pi)_y(\pi/2)_x$ sequence and blue data points are the results after a $(\pi/2)_x(\pi)_y(-\pi/2)_x$ sequence.

reduced due to noise on the transition frequency and the expected phase shift response of the excited state is reduced due to a finite cavity response time T_κ . On the practical side this was done by measuring the response to a full Rabi period with pulse lengths on the order of T_1 and using the average response to all pulses as calibration for the mixed state population. Using an exponential decay law with the measured T_1 as a weighting function, replacing the weighting function from a cavity Bloch simulation, the population after every pulse sequence was then calculated similarly to previous sections.

In order to explain the effect of dephasing which reduces the observed contrast of the Berry phase measurement shown in Fig. 4.23, a spin echo measurement with identical parameters, but without the adiabatic changes between the pulses was performed. Red data points in Fig. 4.25 show the result of a $(\pi/2)_x(\pi)_y(\pi/2)_x$ sequence and blue data points the result of a $(\pi/2)_x(\pi)_y(-\pi/2)_x$ sequence. Ideally, the former rotates the initial ground state always to the excited state and the latter back to the ground state. The population was extracted as discussed above. Two fits yielded a dephasing time of $T_2 \approx 1.7 \mu\text{s}$. From the shown data Fig. 4.25 we expect a visibility of $\sim 60\%$ for the data in Fig. 4.23a and $\sim 50\%$ for the data in Fig. 4.23b. In fact we observe a contrast that is larger than expected, i.e. $\sim 80\%$ and $\sim 60\%$ respectively. This is an interesting observation, in particular because we would expect to see a lower contrast in comparison to the spin echo sequence as the resonator is populated with more photons in the Berry experiment, which are expected to induce photon shot noise on the qubit transition frequency and hence a faster dephasing of the qubit, $1/T_2$ is proportional to n for a small number of photons in the resonators and it is proportional to \sqrt{n} for large n , see [83]. This effect is increasingly relevant for higher intra-cavity photon numbers which is proportional to the drive amplitude applied. Indeed we observe a reduced visibility for large Ω_R , see Fig. 4.23. It turns out however, that there is also a geometric mechanism that is causing a drive dependent reduction of measured contrast, which is discussed in the following. The interesting question on the origin of the enhanced dephasing time at low drive amplitudes however is still unclear and under investigation – it might just be the result of slightly changed qubit parameters between the two measurements.

Geometric Dephasing

In our experiment various sources of noise affect the transition frequency of the qubit. In a spin echo experiment we demonstrated that we are able to cancel any noise with correlation times larger than a sequence time, see 4.3.3. The Berry phase, which is acquired in a spin echo measurement, however is expected to be insensitive to high frequency noise, i.e. noise which is correlated on timescales lower than the time it takes to traverse a loop. This is reasonable, since the geometric phase depends only on the area that is traversed in parameter space, a quantity that is conserved for high frequency noise acting on the amplitude of any one of the parameters. Nevertheless there is one mechanism of decoherence to identify which remains. We expect low frequency noise that is acting on the Berry phase to be not canceled in the spin echo sequence since it is geometrically acquired – in fact this particular noise before and after the spin echo pulse is expected to add up, such as the geometric phase itself. If it is geometrically acquired the degree of dephasing should therefore depend on the path that is traversed in parameter space – indeed this is what we see in the measured data presented in Fig. 4.23a-b.

Figures Fig. 4.23a-b show a decay of the measured expectation values $\langle \sigma_x \rangle$, $\langle \sigma_y \rangle$ and $\langle \sigma_z \rangle$ with Ω_R , i.e. different qubit state dephasing for measurements at different cone angles $\Theta(\Omega_R)$. We mainly attribute this decay to the charge noise on the qubit, which causes fluctuations in the Larmor frequency ω_a hence affecting our actual detuning $\Delta = \omega_a - \omega_d$. It turns out that fluctuations in the detuning at different cone angles Θ have a different impact on the solid angle $\Gamma(C)$ of the traversed path in parameter space. Given Eq. (4.19) for two subsequent loops $\phi = 4\pi$ we can calculate

$$\frac{\partial \gamma}{\partial \Delta} = \pm \frac{\phi}{2} \left(\frac{\Delta^2}{(\Delta^2 + \Omega_R^2)^{3/2}} - \frac{1}{\sqrt{\Delta^2 + \Omega_R^2}} \right), \quad (4.21)$$

which tells us how prone the components of the Berry phase γ are to noise on the detuning Δ . Figure 4.26a shows the sensitivity to noise for different values of $\Omega = \Omega_R/(2\pi)$ where the detuning was taken to be $\Delta = 25$ MHz and the $\phi = 4\pi$ such as in the experiments presented. We see that the sensitivity to noise that does not depend on the drive amplitude

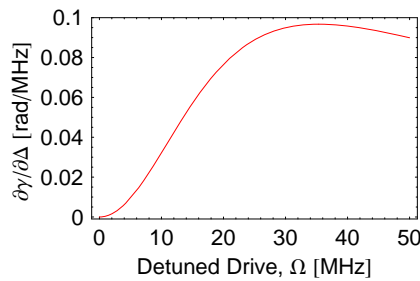


Fig. 4.26: The derivative of the Berry phase Eq. (4.19) with respect to the detuning Δ is plotted as a function of the externally applied drive $\Omega = \Omega_R/(2\pi)$ with $\Delta = 25$ MHz, i.e. the drive dependent sensitivity to changes in Δ for different cone angles $\Theta(\Omega_R)$.

Ω_R , is dependent on the geometry – the cone angle – of the path that is traversed, therefore we call it geometric dephasing. It is important to note however, that we do not expect the acquired Berry phase $\gamma(C)$, that we extract from the measured expectation values $\langle\sigma_x\rangle$ and $\langle\sigma_y\rangle$, to be affected since both components are equally subject to noise and the geometrically acquired phase is conserved on average. More descriptive we expect the length of the Bloch vector to be affected by geometric dephasing rather than where it is pointing to, which is also true for regular dephasing, see chapter 8.3 in [13]. It is not quite clear yet which conditions have to be fulfilled for this assumption to hold. Possibly a symmetric noise distribution and a large ensemble of measurements is required for the acquired phase not being affected by noise. In the experiments however we did not observe significant deviations of the acquired phase from simple theory due to dephasing that depends on the path traversed, see Fig. 4.24.

In order to support these arguments the impact of such noise on the measurement signal has been simulated. We have seen in Eq. (4.18) that the measured components $\langle\sigma_x\rangle$ and $\langle\sigma_y\rangle$ are only dependent on the acquired geometric phase $\gamma(\Omega_R)$ which is given in Eq. (4.19). If we now, as an approximation incorporate a gaussian distributed shot to shot variation of the qubit transition frequency with a standard deviation of $\pm\sigma/2\pi = 3$ MHz affecting the detuning $\Delta/2\pi$ in Eq. (4.19), and average the simulated data $2 \cdot 10^3$ times, we obtain the result shown in Fig. 4.27a. The result compares well to the experimentally acquired data which indicates that the observed decay of visibility for larger drive amplitudes Ω_R is indeed a geometric mechanism. In the experiment we possibly had even more noise on the transition frequency, since the decay of the signal is more pronounced as in the simulation. The exact amount of geometric dephasing however was found to vary somewhat between different runs of the same experiment. In summary we clearly can reproduce the effect of the dephasing of the state vector that is dependent on the geometry of the traversed path. The acquired Berry phase however is not affected by this dephasing mechanism as expected, see Fig. 4.27b.

There are some aspects of this simulation that need further discussion. First of all, the simulation presented does not incorporate any effects arising due to a not perfectly adiabatic evolution of the system. Second, the model shown would be more accurate if we would take into account the fact that it is gaussian type of noise that is acting on the gate charge

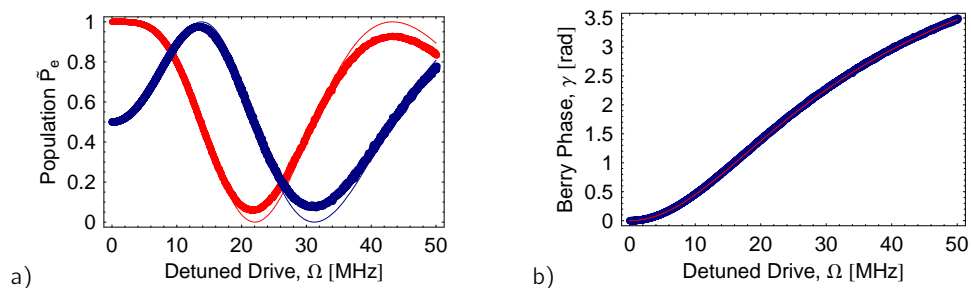


Fig. 4.27: Simulation of the dephasing that is dependent on the geometry – the cone angle – of the traversed path during a Berry phase measurement. a) Dots show simulated and averaged state vector components $\langle\sigma_x\rangle$ and $\langle\sigma_y\rangle$, where gaussian noise with $\sigma/(2\pi) = 3$ MHz is added to the detuning Δ . Solid lines show the same situation without noise. b) Blue dots show the extracted Berry phase and the solid line shows the theoretically expected phase for $\Delta = 25$ MHz.

4 Circuit QED Experiments

affecting the transition frequency in a non linear way – the function is plotted in Fig. 4.2b. A linear approximation however seems to be a reasonable choice for a first investigation of the phenomenon since there are also other sources of noise that affect the qubit transition frequency, see section 4.3.3, and the exact noise-spectrum is presently not known. Third, the charge noise solely increases the transition frequency which can also be seen in Fig. 4.2b. This circumstance is taken into account however since we chose our transition frequency in all experiments presented as the one that yields the highest contrast in a Rabi experiment. This means that we have tried to take the resonant drive frequency ω_d equal to the ‘effective transition frequency’ which was determined for every experiment separately. Finally, in order to generally investigate the influence of noise on the acquired geometric phase a different approach would be more appropriate. Rather than adding noise to the theoretically derived equations of the Berry phase, one should calculate the evolution of the density matrix of this open quantum system [108, 109].

Nevertheless, the model for geometric dephasing presented, i.e. Eq. (4.21), predicts some interesting features that are found to be in agreement with the naive simulation discussed, and could be interesting to try to be verified in an actual experiment. First of all it can be seen in Fig. 4.26 as well as in Fig. 4.28a that the state vector is maximally prone to noise on the transition frequency in the range where $\Omega_R \approx \Delta$. It should therefore be possible to observe a lower dephasing at higher drive rates, that is at larger cone angles. As it is hard to increase the drive further in our experiments, we could choose to decrease the detuning, e.g. $\Delta = 12.5$ MHz which is shown in Fig. 4.28a-c. Indeed the simulation shows an increasing signal at higher driving rates in Fig. 4.28c. Such an effect is however only observable in an experiment if the influence of increased dephasing due to the presence of additional photons in the resonator is almost negligible. Moreover the adiabaticity will decrease for smaller detunings, see Eq. (4.16) and Eq. (4.17), which will make it hard to carry out a corresponding measurement.

Another feature that becomes apparent is that we find the amount of dephasing to scale linearly with the number of loops one traverses in a Berry experiment, see Eq. (4.21). That implies that one can acquire the same Berry phase with less dephasing by traversing less loops at higher driving rates Ω_R . Such a procedure is also favorable for optimally complying with the adiabatic criterion. Finally, for the optimal choice of the detuning Δ there are similar conclusions. Comparing Fig. 4.26 and the red curve in Fig. 4.28a, shows that the

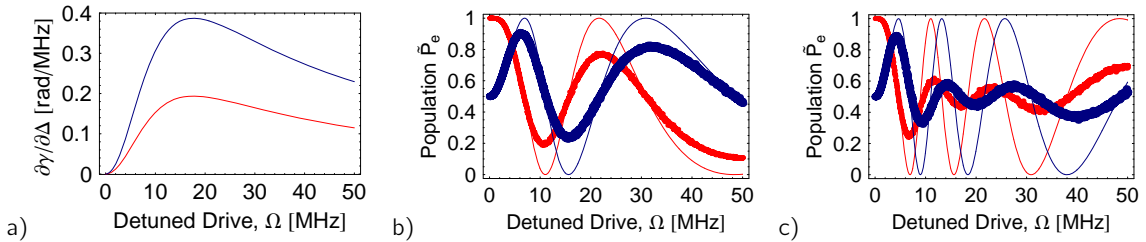


Fig. 4.28: a) Eq. (4.21) plotted for $\Delta = 12.5$ MHz and $\phi = 4\pi$ (red) as well as $\phi = 8\pi$ (blue). b) Simulation of the expected measurement values $\langle \sigma_x \rangle$ and $\langle \sigma_y \rangle$ with $\sigma/(2\pi) = 3$ MHz gaussian noise on the detuning Δ ; given the situation in Fig. a) in red. c) Similar simulation given the situation in Fig. a) in blue.

sensitivity to noise increases for lower detunings however more Berry phase is acquired. The corresponding simulations, compare Fig. 4.27a and Fig. 4.28b, indicate that the latter effect is less pronounced. Additionally we can also comply better with the adiabatic criterion for higher detunings Δ . In conclusion small values of ϕ and high values of Δ seem to be favorable in order to acquire the Berry phase with least geometric dephasing and non adiabatic influence. This is true only if there is a large enough drive power Ω_R available in order to acquire a given phase, while the necessary time is basically limited by the amount of adiabaticity one wants to retain. In the limit close to perfect adiabaticity this is basically the amount of fluctuations in the σ_z direction tolerable when the geometric phase is used as a phase gate in an actual algorithm.

Conclusion

The acquisition of an adiabatically acquired geometric phase could be shown for the first time in a macroscopic solid state system – the Cooper pair box charge qubit. The necessary conditions are long coherence times and full qubit state control and readout. An acquired phase of $\sim 2\pi$ during a sequence of 500 ns could be demonstrated, while the adiabatic criterion was retained relatively well. The obtained degree of accordance with the adiabatic requirement of the Berry phase could be shown to comply with Bloch simulations. In order to use the implemented procedure as a fast and powerful single qubit phase gate however, much longer coherence times, or the utilization of non-adiabatic geometric phases are expected to be required. Finally, a first and possibly naive investigation into the geometry dependent degree of dephasing of the qubit state vector was presented, showing agreement to the directly comparable measurements. Possibly, an extension of the experiments presented, where the response to canceled dynamic phase ($+C \rightarrow -C$) is compared to canceled dynamic and geometric phase ($+C \rightarrow +C$) at different sequence lengths, could be used to interrogate the spectrum of the noise inducing geometric dephasing of the qubit state. Generally, some more discussions on the phenomenon of geometric dephasing will be necessary to draw final conclusions with useful implications on the employment of the geometric phase in a quantum algorithm.

4 *Circuit QED Experiments*

5 Conclusion and Prospects

The measurements presented in this thesis are the result of one year of setting up a laboratory, installing a new experiment and performing first experiments. The experimental setup, a solid state version of optical cavity QED utilizing superconducting qubits coupled to a microwave resonator, has successfully been realized in the framework of this diploma thesis. A number of initial measurements were necessary to become acquainted with the measurement setup and to characterize the sample. In this period a variety of experiments and effects only recently reported by other groups have been reproduced, see sections 4.1 – 4.3. The main focus however was the realization of time-resolved control and read out of the qubit quantum state. The gained understanding and the excellent control over the experimental system finally allowed for a novel measurement to be realized – the first observation of the Berry phase in a solid state quantum bit, see section 4.4.

A wealth of very interesting experiments aiming at the realization of a quantum information processor using the circuit QED architecture remain to be done. Next steps will include an analysis of the contrast in the measurement response for pulsed measurement sequences, an in depth analysis of decoherence mechanisms that affect the qubit state and the development of single shot qubit read out. Another major step forward would be the realization of time-resolved sideband transitions which would allow the implementation of a first proof of principle quantum algorithm, such as the Deutsch algorithm, in a superconducting circuit. The main path of research will then be to scale the system up to two and more qubits coupled via single intra-cavity photons. As soon as the required samples will be available, the creation of conditional gates and entangled states will be a major goal. In order to prove their entanglement a test of Bell inequalities, a GHZ experiment or the teleportation of a quantum state on a chip could be performed. Equally exciting would be the realization of a truly hybrid quantum processor, where long living hyperfine states of on-chip trapped ions could be coupled through a resonator to superconducting macroscopic qubit states that allow for fast gate operations.

There are numerous technological as well as conceptual challenges waiting to be solved until a quantum processor will beat any classical computer in solving a given task faster. The progress in the field however is accelerating and there is a lot of interesting physics to be unveiled on this path. Experimental research is always also about being curious, playing and pushing technological borders. The circuit QED architecture clearly provides an excellent playground to investigate various quantum optics and quantum information processing phenomena in a novel environment and to test and push the boundaries of the size of truly quantum mechanically behaving systems further and further. It really is what could be called *a quantum mechanics lab on a chip*.

5 *Conclusion and Prospects*

Bibliography

- [1] Mabuchi, H. and Doherty, A. C. Cavity Quantum Electrodynamics: Coherence in Context. *Science* **298**(5597), 1372–1377 (2002).
- [2] Blais, A., Huang, R. S., Wallraff, A., Girvin, S. M., and Schoelkopf, R. J. Cavity quantum electrodynamics for superconducting electrical circuits: An architecture for quantum computation. *Physical Review A* **69**(6), 062320 (2004).
- [3] Wallraff, A., Schuster, D. I., Blais, A., Frunzio, L., Huang, R. S., Majer, J., Kumar, S., Girvin, S. M., and Schoelkopf, R. J. Strong coupling of a single photon to a superconducting qubit using circuit quantum electrodynamics. *Nature* **431**(7005), 162–167 (2004).
- [4] Schuster, D. I., Houck, A. A., Schreier, J. A., Wallraff, A., Gambetta, J. M., Blais, A., Frunzio, L., Majer, J., Johnson, B., Devoret, M. H., Girvin, S. M., and Schoelkopf, R. J. Resolving photon number states in a superconducting circuit. *Nature* **445**(7127), 515–518 (2007).
- [5] Houck, A. A., Schuster, D. I., Gambetta, J. M., Schreier, J. A., Johnson, B. R., Chow, J. M., Majer, J., Frunzio, L., Devoret, M. H., Girvin, S. M., and Schoelkopf, R. J. Generating single microwave photons in a circuit. *cond-mat/* **0702648** (2007).
- [6] Blais, A., Gambetta, J., Wallraff, A., Schuster, D. I., Girvin, S. M., Devoret, M. H., and Schoelkopf, R. J. Quantum-information processing with circuit quantum electrodynamics. *Physical Review A* **75**(3), 032329 (2007).
- [7] Wallraff, A., Schuster, D. I., Blais, A., Gambetta, J. M., Schreier, J., Frunzio, L., Devoret, M. H., Girvin, S. M., and Schoelkopf, R. J. Sideband transitions and two-tone spectroscopy of a superconducting qubit strongly coupled to an on-chip cavity, (2007).
- [8] De Chiara, G. and Palma, G. M. Berry phase for a spin 1/2 particle in a classical fluctuating field. *Phys. Rev. Lett.* **91**(9), 090404, Aug (2003).
- [9] Zhu, S.-L. and Zanardi, P. Geometric quantum gates that are robust against stochastic control errors. *Physical Review A* **72**(2), 020301 (2005).
- [10] Lloyd, S. The computational universe: Quantum gravity from quantum computation. *quant-ph/* **0501135** (2005).
- [11] Feynman, R. P. Simulating physics with computers. *International Journal Of Theoretical Physics* **21**(6-7), 467–488 (1982).

Bibliography

- [12] DiVincenzo, D. P. and Loss, D. Quantum information is physical. *Superlattices and Microstructures* **23**, 419 (1998).
- [13] Nielsen, M. A. and Chuang, I. L. *Quantum Computation and Quantum Information*. Cambridge University Press, (2000).
- [14] Shor, P. W. Polynomial-time algorithms for prime factorization and discrete logarithms on a quantum computer. *Siam J. Sci. Statist. Comput.* **26**, 1484 (1997).
- [15] Grover, L. K. A fast quantum mechanical algorithm for database search. In *STOC '96: Proceedings of the twenty-eighth annual ACM symposium on Theory of computing*, 212–219 (ACM Press, New York, NY, USA, 1996).
- [16] Farhi, E., Goldstone, J., Gutmann, S., Lapan, J., Lundgren, A., and Preda, D. A Quantum Adiabatic Evolution Algorithm Applied to Random Instances of an NP-Complete Problem. *Science* **292**(5516), 472–475 (2001).
- [17] Zurek, W. H. Decoherence and the transition from quantum to classical – revisited. *Los Alamos Science* **27** (2002).
- [18] Steffen, M., Ansmann, M., Bialczak, R. C., Katz, N., Lucero, E., McDermott, R., Neeley, M., Weig, E. M., Cleland, A. N., and Martinis, J. M. Measurement of the Entanglement of Two Superconducting Qubits via State Tomography. *Science* **313**(5792), 1423–1425 (2006).
- [19] Niskanen, A. O., Harrabi, K., Yoshihara, F., Nakamura, Y., Lloyd, S., and Tsai, J. S. Quantum Coherent Tunable Coupling of Superconducting Qubits. *Science* **316**(5825), 723–726 (2007).
- [20] Majer, J. B., Paauw, F. G., ter Haar, A. C. J., Harmans, C. J. P. M., and Mooij, J. E. Spectroscopy on two coupled superconducting flux qubits. *Physical Review Letters* **94**(9), 090501 (2005).
- [21] Andre, A., DeMille, D., Doyle, J. M., Lukin, M. D., Maxwell, S. E., Rabl, P., Schoelkopf, R. J., and Zoller, P. A coherent all-electrical interface between polar molecules and mesoscopic superconducting resonators. *Nature Physics* **2**, 636–642 (2006).
- [22] Rabl, P., DeMille, D., Doyle, J. M., Lukin, M. D., Schoelkopf, R. J., and Zoller, P. Hybrid quantum processors: Molecular ensembles as quantum memory for solid state circuits. *Physical Review Letters* **97**(3), 033003 (2006).
- [23] Tian, L., Rabl, P., Blatt, R., and Zoller, P. Interfacing quantum-optical and solid-state qubits. *Physical Review Letters* **92**(24), 247902 (2004).
- [24] Wendin, G. and Shumeiko, V. S. Superconducting Quantum Circuits, Qubits and Computing. Handbook of Theoretical and Computational Nanotechnology, Eds. M. Rieth and W. Schommers. Ch. 12. *American Scientific Publishers*. (2006), cond-mat/ (0508729).

- [25] Wootters, W. K. and Zurek, W. H. A single quantum cannot be cloned. *Nature* **299**, 802–803 (1982).
- [26] Bennett, C. H. and Brassard, G. Quantum cryptography: public key distribution and coin tossing. *Int. Conf. on Computers, Systems and Signal Processing* (Bangalore, India, Dec. 1984), 175 (1984).
- [27] Ekert, A. K. Quantum cryptography based on bell's theorem. *Phys. Rev. Lett.* **67**(6), 661–663, Aug (1991).
- [28] Bužek, V. and Hillery, M. Quantum copying: Beyond the no-cloning theorem. *Phys. Rev. A* **54**(3), 1844–1852, Sep (1996).
- [29] Einstein, A., Podolsky, B., and Rosen, N. Can quantum-mechanical description of physical reality be considered complete? *Phys. Rev.* **47**(10), 777–780, May (1935).
- [30] Bell, J. On the einstein-podolsky-rosen paradox. *Physics* **1**, 195–200 (1964).
- [31] Bohm, D. and Aharonov, Y. Discussion of experimental proof for the paradox of einstein, rosen, and podolsky. *Phys. Rev.* **108**(4), 1070–1076, Nov (1957).
- [32] Clauser, J. F. and Horne, M. A. Experimental consequences of objective local theories. *Phys. Rev. D* **10**(2), 526–535, Jul (1974).
- [33] Aspect, A., Dalibard, J., and Roger, G. Experimental test of bell's inequalities using time-varying analyzers. *Phys. Rev. Lett.* **49**(25), 1804–1807, Dec (1982).
- [34] Weihs, G., Jennewein, T., Simon, C., Weinfurter, H., and Zeilinger, A. Violation of bell's inequality under strict einstein locality conditions. *Phys. Rev. Lett.* **81**(23), 5039–5043, Dec (1998).
- [35] Rowe, Kielpinski, Meyer, Sackett, Itano, Monroe, and Wineland. Experimental violation of a bell's inequality with efficient detection. *Nature* **409** (2001).
- [36] Greenberger, D. M., Horne, M. A., Shimony, A., and Zeilinger, A. Bell's theorem without inequalities. *American Journal of Physics* **58**(12), 1131–1143 (1990).
- [37] Gröblacher, S., Paterek, T., Kaltenbaek, R., Brukner, C., Zukowski, M., Aspelmeyer, M., and Zeilinger, A. An experimental test of non-local realism. *Nature* **446**(7138), 871–875 (2007).
- [38] Everett, H. "relative state" formulation of quantum mechanics. *Rev. Mod. Phys.* **29**(3), 454–462, Jul (1957).
- [39] DeWitt, B. S. Quantum mechanics and reality. *Physics Today* **23**(9), 30–40 (1957).
- [40] Deutsch, D. The fabric of reality: The science of parallel universes and its implications. *Penguin Books* (1998).

Bibliography

- [41] Walther, P., Resch, K. J., Rudolph, T., Schenck, E., Weinfurter, H., Vedral, V., Aspelmeyer, M., and Zeilinger, A. Experimental one-way quantum computing. *Nature* **434**, 169 (2005).
- [42] Vandersypen, L. M. K., Steffen, M., Breyta, G., Yannoni, C. S., Sherwood, M. H., and Chuang, I. L. Experimental realization of shor’s quantum factoring algorithm using nuclear magnetic resonance. *Nature* **414**, 883 (2001).
- [43] Cirac, J. I. and Zoller, P. Quantum computations with cold trapped ions. *Physical Review Letters* **74**(20), 4091–4094 (1995).
- [44] Stephan, G., Mark, R., Gavin, P. T. L., Christoph, B., Jürgen, E., Hartmut, H., Ferdinand, S.-K., Chuang, I. L., and Blatt., R. Implementation of the deutsch–jozsa algorithm on an ion-trap quantum computer. *Nature* **421**, 48–50 (2003).
- [45] Vion, D., Aassime, A., Cottet, A., Joyez, P., Pothier, H., Urbina, C., Esteve, D., and Devoret, M. H. Manipulating the Quantum State of an Electrical Circuit. *Science* **296**(5569), 886–889 (2002).
- [46] Wallraff, A., Schuster, D. I., Blais, A., Frunzio, L., Majer, J., Devoret, M. H., Girvin, S. M., and Schoelkopf, R. J. Approaching unit visibility for control of a superconducting qubit with dispersive readout. *Phys. Rev. Lett.* **95**, 060501 (2005).
- [47] Aharonov, D., van Dam, W., Kempe, J., Landau, Z., Lloyd, S., and Regev, O. Adiabatic quantum computation is equivalent to standard quantum computation. *quant-ph/0405098* (2004).
- [48] Deutsch, D. Quantum theory, the church-turing principle and the universal quantum computer. *Proceedings of the Royal Society of London. Series A, Mathematical and Physical Sciences* **400**(1818), 97–117 (1985).
- [49] Deutsch, D. and Jozsa, R. Rapid solution of problems by quantum computation. *Proceedings of the Royal Society of London, Series A* **439**, 553 (1992).
- [50] Steane, A. M. The ion trap quantum information processor. *Applied Physics B* **64**, 623 (1997).
- [51] Stick, D., Hensinger, W. K., Olmschenk, S., Madsen, M. J., Schwab, K., and Monroe, C. Ion trap in a semiconductor chip. *Nature Physics* **2**, 36 (2006).
- [52] Yamamoto, T., Pashkin, Y. A., Astafiev, O., Nakamura, Y., and Tsai, J. S. Demonstration of conditional gate operation using superconducting charge qubits. *Nature* **425**, 941 (2003).
- [53] Bertet, P., Chiorescu, I., Burkard, G., Semba, K., Harmans, C. J. P. M., DiVincenzo, D. P., and Mooij, J. E. Dephasing of a superconducting qubit induced by photon noise. *Physical Review Letters* **95**(25), 257002 (2005).

- [54] Johansson, J., Saito, S., Meno, T., Nakano, H., Ueda, M., Semba, K., and Takayanagi, H. Vacuum rabi oscillations in a macroscopic superconducting qubit Ic oscillator system. *Physical Review Letters* **96**(12), 127006 (2006).
- [55] Chiorescu, I., Bertet, P., Semba, K., Nakamura, Y., Harmans, C. J. P. M., and Mooij, J. E. Coherent dynamics of a flux qubit coupled to a harmonic oscillator. *Nature (London)* **431**, 159–162 (2004).
- [56] Devoret, M. H., Wallraff, A., and Martinis, J. M. Superconducting qubits: A short review. *cond-mat/* **0411174** (2004).
- [57] Göppl, M. *Quantenelektronik mit supraleitenden Bauelementen - Herstellung und Charakterisierung von Fluss - Qubits*. Diploma thesis, Technische Universität München, (2006).
- [58] Tinkham, M. *Introduction to Superconductivity*. McGraw-Hill International Editions, (1996).
- [59] Büttiker, M. Zero-current persistent potential drop across small-capacitance josephson junctions. *Phys. Rev. B* **36**(7), 3548–3555, Sep (1987).
- [60] Bouchiat, V., Vion, D., Joyez, P., Esteve, D., and Devoret, M. H. Quantum coherence with a single Cooper pair. *Physica Scripta* **T76**, 165–170 (1998).
- [61] Nakamura, Y., Pashkin, Y., and Tsai, J. S. Coherent control of macroscopic quantum states in a single-cooper-pair box. *Nature* **398**(6730), 786–788, April (1999).
- [62] Vion, D., Aassime, A., Cottet, A., Joyez, P., Pothier, H., Urbina, C., Esteve, D., and Devoret, M. H. Manipulating the quantum state of an electrical circuit. *Science* **296**, 886–889 (2002).
- [63] Makhlin, Y., Schön, G., and Shnirman, A. Quantum-state engineering with Josephson-junction devices. *Rev. Mod. Phys.* **73**, 357–400 (2001).
- [64] Schuster, D. I. *Circuit Quantum Electrodynamics*. PhD thesis, Yale University, (2006).
- [65] Bouchiat, V. *Quantum fluctuations of the charge in single electron and single Cooper pair devices*. PhD thesis, Université Paris VI, CEA-Saclay, (1997).
- [66] Cottet, A. *Implementation of a quantum bit in a superconducting circuit*. PhD thesis, Université Paris VI, CEA-Saclay, (2002).
- [67] Pozar, D. Microwave engineering. *Addison-Wesley Publishing Company* (1993).
- [68] Wallraff, A., Majer, H., Frunzio, L., and Schoelkopf, R. Superconducting solid state cavity quantum electrodynamics, notes on resonators. (2003).
- [69] Simons, R. N. Coplanar waveguide circuits, components and systems. *Wiley Series in Microwave and Optical Engineering, Wiley Inter-Science* (2001).

Bibliography

- [70] Walls, D. and Milburn, G. *Quantum Optics*. Springer-Verlag, Berlin, (1994).
- [71] Haroche, S. *Fundamental Systems in Quantum Optics*, chapter Cavity quantum electrodynamics, 767. Elsevier (1992).
- [72] Haroche, S. and Kleppner, D. Cavity quantum electrodynamics. *Physics Today* , 24, January (1989).
- [73] Gambetta, J., Blais, A., Schuster, D. I., Wallraff, A., Frunzio, L., Majer, J., Devoret, M. H., Girvin, S. M., and Schoelkopf, R. J. Qubit-photon interactions in a cavity: Measurement-induced dephasing and number splitting. *Physical Review A* **74**(4), 042318 (2006).
- [74] Frunzio, L., Wallraff, A., Schuster, D. I., Majer, J., and Schoelkopf, R. J. Fabrication and characterization of superconducting circuit qed devices for quantum computation. *IEEE Trans. Appl. Supercond.* **15**, 860 (2005).
- [75] Pobell, F. *Matter and methods at low temperatures*. Springer, 2nd edition, (1995).
- [76] Enss, C. and Hunklinger, S. *Low-Temperature Physics*. Springer-Verlag Berlin Heidelberg, (2005).
- [77] Kirk, W. P. and Twerdochlib, M. Improved method for minimizing vibrational motion transmitted by pumping lines. *Rev. Sci. Instrum.* **49**, 6 (1978).
- [78] Roth, A. *vacuum technology*. North-Holland Publishing Company, (1976).
- [79] Richardson, R. C. and Smith, E. N. *Experimental Techniques in Condensed Matter Physics at Low Temperatures*. Addison-Wesley Publishing Company, Inc, (1988).
- [80] Schwabl, F. *Quantenmechanik*. Springer-Verlag, Berlin Heidelberg New York, (2002).
- [81] Koch, J., Yu, T. M., Gambetta, J., Houck, A. A., Schuster, D. I., Majer, J., Blais, A., Devoret, M. H., Girvin, S. M., and Schoelkopf, R. J. Introducing the transmon: a new superconducting qubit from optimizing the cooper pair box. *cond-mat/* **0703002v1** (2007).
- [82] Aumentado, J., Keller, M. W., Martinis, J. M., and Devoret, M. H. Nonequilibrium quasiparticles and $2e$ periodicity in single-cooper-pair transistors. *Physical Review Letters* **92**(6), 066802, February (2004).
- [83] Schuster, D. I., Wallraff, A., Blais, A., Frunzio, L., Huang, R. S., Majer, J., Girvin, S. M., and Schoelkopf, R. J. ac stark shift and dephasing of a superconducting qubit strongly coupled to a cavity field. *Physical Review Letters* **94**(12), 123602 (2005).
- [84] Schmidt-Kaler, F., Haffner, H., Riebe, M., Gulde, S., Lancaster, G. P. T., Deuschle, T., Becher, C., Roos, C. F., Eschner, J., and Blatt, R. Realization of the cirac-zoller controlled-not quantum gate. *Nature* **422**(6930), 408–411 (2003).

- [85] Blais, A. *Cavity Bloch Simulation*. privat communications, (2007).
- [86] Ithier, G., Collin, E., Joyez, P., Meeson, P. J., Vion, D., Esteve, D., Chiarello, F., Shnirman, A., Makhlin, Y., Schrieffer, J., and Schön, G. Decoherence in a superconducting quantum bit circuit. *Phys. Rev. B* **72**(13), 134519, Oct (2005).
- [87] Slichter, C. P. *Principles of Magnetic Resonance, 3rd ed.* Springer-Verlag, Berlin, (1990).
- [88] Steffen, L. *Spin Echo Measurements in a Superconducting Qubit*. Semesterarbeit, ETH Zürich, (2007).
- [89] Vion, D., Aassime, A., Cottet, A., Joyez, P., Pothier, H., Urbina, C., Esteve, D., and Devoret, M. H. Rabi oscillations, ramsey fringes and spin echoes in an electrical circuit. *Fortschritte der Physik* **51**(4-5), 462–468 (2003).
- [90] Nakamura, Y., Pashkin, Y. A., Yamamoto, T., and Tsai, J. S. Charge echo in a Cooper-pair box. *Phys. Rev. Lett.* **88**, 047901 (2002).
- [91] Maurer, P. *Tomography on Superconducting Qubit States*. Semesterarbeit, ETH Zürich, (2007).
- [92] Steffen, M., Ansmann, M., Mcdermott, R., Katz, N., Bialczak, R. C., Lucero, E., Neeley, M., Weig, E. M., Cleland, A. N., and Martinis, J. M. State tomography of capacitively shunted phase qubits with high fidelity. *Physical Review Letters* **97**(5) (2006).
- [93] Katz, N., Ansmann, M., Bialczak, R. C., Lucero, E., McDermott, R., Neeley, M., Steffen, M., Weig, E. M., Cleland, A. N., Martinis, J. M., and Korotkov, A. N. Coherent State Evolution in a Superconducting Qubit from Partial-Collapse Measurement. *Science* **312**(5779), 1498–1500 (2006).
- [94] Berry, M. V. Quantal phase factors accompanying adiabatic changes. *Proc. R. Soc. Lond.* **A392**, 45–57 (1984).
- [95] Wilczek, F. and Shapere, A. *Geometric Phases in Physics*. World Scientific, (1989).
- [96] Anandan, J. The geometric phase. *Nature* **360**, 307–313 (1992).
- [97] Jones, J., Vedral, V., Ekert, A., and Castagnoli, G. Geometric quantum computation using nuclear magnetic resonance. **403**, 869–71 (2000).
- [98] Leibfried, D., DeMarco, B., Meyer, V., Lucas, D., Barrett, M., Britton, J., Itano, W. M., Jelenkovic, B., Langer, C., Rosenband, T., and Wineland, D. J. Experimental demonstration of a robust, high-fidelity geometric two ion-qubit phase gate. *Nature* **422**(6930), 412–415, March (2003).
- [99] Falci, G., Fazio, R., Palma, G. M., Siewert, J., and Vedral, V. Detection of geometric phases in superconducting nanocircuits. *Nature* **407**, 355–358 (2000).

Bibliography

- [100] Blais, A. and Tremblay, A. M. S. Effect of noise on geometric logic gates for quantum computation. *Physical Review A* **67**(1), 012308, January (2003).
- [101] Mottonen, M., Pekola, J. P., Vartiainen, J. J., Brosco, V., and Hekking, F. W. J. Measurement scheme of the berry phase in superconducting circuits. *Physical Review B* **73**(21), 214523, June (2006).
- [102] Xiang-bin, W. and Keiji, M. Nonadiabatic detection of the geometric phase of the macroscopic quantum state with a symmetric squid. *Phys. Rev. B* **65**(17), 172508, May (2002).
- [103] Pancharatnam, S. Generalized theory of interference and its applications. *Proc. Indian Acad. Sci.* **A44**, 247–262 (1956).
- [104] Aharonov, Y. and Anandan, J. Phase change during a cyclic quantum evolution. *Phys. Rev. Lett.* **58**, 1593–1596 (1987).
- [105] Hannay, J. H. Angle variable holonomy in adiabatic excursion of an integrable hamiltonian. *Journal of Physics A: Mathematical and General* **18**(2), 221–230 (1985).
- [106] Durstberger, K. *Geometric Phases in Quantum Theory*. Diploma thesis, Universität Wien, (2002).
- [107] Ehrenfest, P. Adiabatische invarianten und quantentheorie. *Ann. d. Phys.* **51**, 327 (1916).
- [108] Kamleitner, I., Cresser, J. D., and Sanders, B. C. Geometric phase for an adiabatically evolving open quantum system. *Physical Review A* **70**(4), 044103 (2004).
- [109] De Chiara, G., Lozinski, A., and Palma, G. M. Berry phase in open quantum systems: a quantum langevin equation approach. *Eur.Phys.J.D* **41**, 179 (2007).

Acknowledgements

The presented work is the result of a collaboration with a considerable number of people, who all contributed in different ways. First of all I want to express my gratitude to my supervisor Prof. Andreas Wallraff who gave me the opportunity to work on this fascinating subject. He shared his vast knowledge about physics as well as technological aspects with me and I want to thank him for his continuous support and encouragement. I enjoyed it to be one of the first members of an initially really small research group which necessitated not only a lot of basic laboratory setup work, but also a very personal mentoring from which I have profited a lot.

I also want to thank all my colleagues at the Quantum Device Lab. Together with Peter Leek I was working on the Berry phase measurement, Romeo Bianchetti worked with me on the installation and setup of the dilution refrigerator and Martin Göppl was the reference for questions related to electronics. The semester thesis students Lars Steffen and Peter Maurer strongly contributed to the investigation of spin echo experiments and quantum state tomography respectively. Finally, Will Braff, a summer student from Yale University collaborated on the characterization of the data acquisition card.

There were also a lot of people involved in the renovation and setup of the laboratory and office facilities here at ETH. First of all I want to mention our group technician Hans Rudolf Aeschbach and our group secretary Gabriela Strahm. I also thank the technical staff at ETH, including Hans-Jürg Gübeli, Jean-Pierre Stucki and Walter Bachmann. Finally I want to thank the staff of the mechanical workshop, which I made use of quite heavily when I started to work in the newly founded group.

Another crucial aspect for the success of this work was the sample investigated. It was provided by the research group my supervisor Prof. Wallraff was formerly part of – the group of Prof. Robert Schoelkopf at Yale University. I want to mention David Schuster in particular. He has not only fabricated the sample investigated in this thesis, but he furthermore supported us with his expertise concerning the data acquisition software being used. I also thank Prof. Alexandre Blais from Université de Sherbrooke and Jay Gambetta from Yale University for a number of helpful discussions on the theoretical aspects of the experimental results presented.

Finally I want to express my gratitude to the people who made it possible to come from Vienna to Zürich for doing my diploma thesis. Together with Prof. Markus Arndt from the University of Vienna, his secretary Ursula Gerber and my supervisor an Erasmus student exchange program between the two Universities has been brought into being. This new opportunity will hopefully provide a fascinating and instructive time for many students of both Universities in the upcoming years.

Curriculum Vitae

Name:	Johannes Martin Fink
Contact Details:	Wolfbühl 324 6934 Sulzberg, Austria Email: JohannesFink@gmx.net
Citizenship:	Austria
Date, Place of Birth:	21 st of December 1981 in Bregenz, Austria.
Education:	1996 – 2001 <i>HTL Bregenz</i> – higher technical school for mechanical engineering and automation technology. Thesis: ‘Heat-dissipation by Convection at Cylindrical Bodies’ in cooperation with <i>Liebherr Aerospace</i> , Germany. 2002 – 2007 Study of physics at the <i>University of Vienna</i> . 2004 Joint Study Exchange fellowship at <i>Macquarie University</i> , Sydney. Internship in theoretical physics: ‘Quantum Information Transfer in an Open Quantum System’ supervised by senior lecturer Dr. James Cresser. 2006 European Union Erasmus fellowship, working on my diploma thesis at the Quantum Device Lab, <i>ETH Zürich</i> .
Professional Experience:	1997 <i>Meusburger tool-making</i> in Wolfurt, Austria. Divisions machining and quality assurance – 4 weeks. 1998 – 2003 <i>Doppelmayr rope-ways</i> in Wolfurt, Austria. Division assembling – 2 months. Division technical office: construction, design and development – 5 months. 2001 – 2002 Obligatory military service – 7 months. 2005 <i>Liebherr Aerospace</i> in Lindenberg, Germany. Division performance and actuation systems: performance simulations and computation of flight controlling components for the Airbus A 400M – 1.5 months. 2006 – 2007 <i>ETH Zürich</i> , Switzerland. Department of Physics, Laboratory for Solid State Physics, Quantum Device Group of Prof. Dr. Andreas Wallraff as a research associate – 6 months.

Zürich, 29th of May 2007

